Charles University in Prague

Faculty of Mathematics and Physics

DOCTORAL THESIS

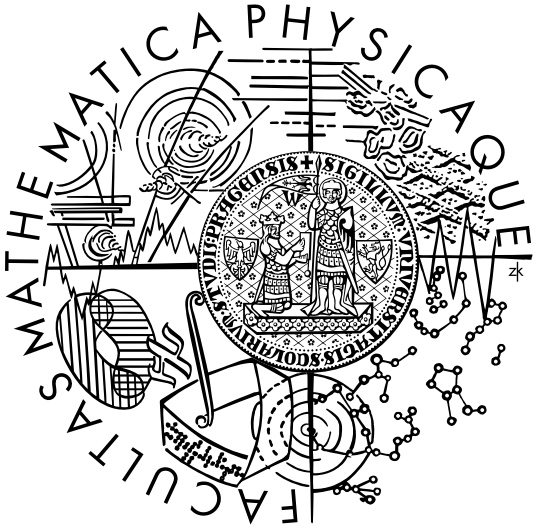

Jan Kapitán

Jet production in p+p and d+Au collisions at $\sqrt{s_{\mathrm{NN}}} = 200$ GeV in STAR

Nuclear Physics Institute AS CR

Thesis supervisor: doc. Michal Šumbera, CSc., DSc.

Study field: Subnuclear Physics

Prague, December 2011

Acknowledgments

Above all I offer my sincere gratitude to Jana Bielčíková, who was my mentor and advisor and gave me both motivation and guidance needed for my work. Not only her expertise and insight was indispensable for my research, but I indeed enjoyed working with her.

My utmost acknowledgement belongs to my supervisor Michal Šumbera. He always pointed me to the right direction when I needed help and without his support I would never be where I am today.

I would like to express my gratitude towards the STAR Collaboration in which I had the privilege to work with many outstanding scientists and met many good friends. I want to thank Helen Caines, Renee Fatemi and Jörn Putschke for discussions and comments on my analysis. I would like to express my sincere thanks to John Harris for the support I received during my stays in New Haven. I would also like to thank Xin Dong who helped me immensely during my service work project (Heavy Flavor Tracker).

I was lucky to work in great team of coworkers in the Prague heavy ion group. I'd like to thank my fellow students Michal Zerola, Michal Bysterský, David Tlustý, Jan Rusňák and Michal Vajzer for their support in either physics or computing related matters, and also for just being good friends. A special thank you to Petr Chaloupka for his indispensable help with finishing my thesis. Many thanks to Vojtěch Petráček, Jaro Bielčík and Boris Tomášik for organizing the physics seminars.

I would like to thank Elena for her friendship and Juraj for the motivation.

Finally, I want to thank my parents and my brother. Without your unconditional support this all would not be possible.

Declaration of Originality

This doctoral thesis contains results of my research carried out at the Nuclear Physics Institute AS CR between years 2006 and 2011. Most of this work was carried out within STAR Collaboration.

Excluding introductory parts, the research described in this thesis is original unless where an explicit reference is made to work of others. I further state that no part of this thesis or any substantially the same has been submitted for any qualification other than the degree of Doctor of Philosophy at the Charles University in Prague.

Prohlašuji, že jsem tuto disertační práci vypracoval samostatně a výhradně s použitím citovaných pramenů, literatury a dalších odborných zdrojů.

Beru na vědomí, že se na moji práci vztahují práva a povinnosti vyplývající ze zákona č. 121/2000 Sb., autorského zákona v platném znění, zejména skutečnost, že Univerzita Karlova v Praze má právo na uzavření licenční smlouvy o užití této práce jako školního díla podle §60 odst. 1 autorského zákona.

V Brně dne 14.12.2011 Podpis autora

Název práce:
Produkce jetů ve srážkách p+p a d+Au při $\sqrt{s_{\mathrm{NN}}} = 200$ GeV ve STARu

Autor: Jan Kapitán

Školící pracoviště: Ústav jaderné fyziky AV ČR, v.v.i.

Vedoucí disertační práce:
doc. Michal Šumbera, CSc., DSc., Ústav jaderné fyziky AV ČR, v.v.i.

Abstrakt:
Cílem této práce je měření efektů studené jaderné hmoty na produkci jetů v $\sqrt{s_{\mathrm{NN}}} =$ 200 GeV srážkách d+Au na Relativistic Heavy Ion Collider (RHIC). Po stručném teoretickém úvodu a popisu experimentálního zařízení je popsána analýza jetů a potřebné opravy. Jety jsou rekonstruovány ve srážkách p+p a d+Au z experimentu STAR pomocí jetového algoritmu anti $-$ k$_{\mathrm{T}}$. Inkluzivní p_{T} spektra jetů ve srážkách d+Au a jejich centralitní závislost jsou porovnány s referenčním měřením ve srážkách p+p a se škálováním podle binárních srážek. Korelace di-jetů jsou studovány v p+p a nejcentrálnějších srážkách d+Au pro měření k_{T} efektu a jeho možného jaderného rozšiřování. Tyto výsledky budou rovněž použity jako referenční měření pro probíhající studie produkce jetů ve srážkách těžkých iontů na RHICu.

Klíčová slova: jety, srážky d+Au, efekty studené jaderné hmoty, STAR, RHIC

Title: Jet production in p+p and d+Au collisions at $\sqrt{s_{\mathrm{NN}}} = 200$ GeV in STAR

Author: Jan Kapitán

Affiliation: Nuclear Physics Institute AS CR

Supervisor: doc. Michal Šumbera, CSc., DSc., Nuclear Physics Institute AS CR

Abstract:
The aim of this work is to measure the effects of cold nuclear matter on jet production in $\sqrt{s_{\mathrm{NN}}} = 200$ GeV d+Au collisions at Relativistic Heavy Ion Collider (RHIC). After a brief theoretical introduction and description of the experimental setup, jet analysis and the required corrections are described. The jets are reconstructed in p+p and d+Au collisions recorded by the STAR experiment using the anti $-$ k$_{\mathrm{T}}$ jet algorithm. Inclusive jet p_{T} spectra in d+Au collisions and their centrality dependence are compared to the reference measurement in p+p collisions and to the binary collision scaling. Di-jet correlations are studied in p+p and most central d+Au collisions to measure the k_{T} effect and its possible nuclear broadening. These results will also be used as a baseline measurement for ongoing studies of jet production in heavy-ion collisions at RHIC.

Keywords: jets, d+Au collisions, cold nuclear matter effects, STAR, RHIC

Contents

Introduction

Hot and dense QCD matter with deconfined quarks and gluons (Quark Gluon Plasma) is expected to be created in high energy heavy-ion (A+A) collisions at RHIC [1]. One of the QGP signals is the suppression of high-p_{T} hadron production ("jet quenching") due to jet interaction with the hot and dense medium produced in central Au+Au collisions. The large suppression [2] of inclusive high-p_{T} hadron production with respect to the expectation from rescaled p+p collisions and disappearance of back-to-back di-hadron correlation [3] in central Au+Au collisions are examples of such signals. With the data from d+Au collisions on the same observables [4] it became clear that initial nuclear state effects can not describe the observations in central Au+Au collisions. Only then jet quenching could be unequivocally attributed to the creation of hot and dense medium in the final state of the collision.

The studies of jet quenching using single particle spectra and di-hadron correlations are limited in their sensitivity to probe partonic energy loss mechanisms by surface and fragmentation biases [5]. Full jet reconstruction in heavy-ion collisions enables a complete study of the modification of jet structure due to energy loss. The goal of the present work is to provide a baseline measurement for ongoing studies of jet production in Au+Au collisions by the STAR collaboration and to measure the effects of cold nuclear matter in d+Au collisions, that is the modification of jet observables from p+p (or peripheral d+Au) collisions to central d+Au collisions at $\sqrt{s_{\mathrm{NN}}} = 200$ GeV.

The results presented in this thesis are based on application of anti$-\mathrm{k_T}$ jet algorithm to p+p and d+Au collision data from 2007-2008 run of RHIC collider collected by the STAR experiment. The fully corrected jet p_{T} spectrum in 0-20% most central d+Au collisions at midrapidity is calculated and compared to previous STAR measurements of jet p_{T} spectra from p+p collisions. Centrality dependence of jet yields in d+Au collisions is studied and comparison to scaling with mean number of binary collisions is conducted via the measurement of jet R_{CP}. The azimuthal correlations between two highest p_{T} jets in di-jet events from 0-20% most central collisions are studied and used to measure the k_{T} effect, in particular its Gaussian width $\sigma_{k\mathrm{T}}$. The results are discussed in relation to the theoretical expectations of

these observables. Comparison is also made to existing measurements of similar quantities coming from PHENIX experiment at RHIC or using different methods.

The thesis is structured as follows. Chapter 1 provides a brief introduction to Quantum Chromodynamics (QCD) and explains its basic principles. Jet production in high energy hadron collisions is described in Chapter 2 together with overview of jet-related measurements from nuclear collisions at RHIC. The experimental setup of the RHIC collider and the STAR experiment are the subject of Chapter 3.

Prior to the jet analysis the author completed his *service work* project for the STAR Collaboration, which was related to Heavy Flavor Tracker (HFT), one of the upgrades of the STAR experiment currently under way. This topic involved running simulations and analyzing the simulated data concentrating on D^0 and Λ_C reconstruction in central Au+Au collisions. The HFT upgrade project is briefly described and the simulations and their implication for the upgraded detector performance are presented in Chapter 4.

The data used for this analysis, jet reconstruction techniques and treatment of underlying event background are discussed in Chapter 5. Chapter 6 describes the corrections used in the inclusive jet analysis in d+Au. Inclusive jet p_T spectra in d+Au collisions are compared to a reference measurement from p+p collisions and centrality dependence of nuclear modification factor R_{CP} is studied. The measurement of di-jets in p+p and d+Au collisions is reported in Chapter 7. Finally, Chapter 8 contains the conclusion and outlook.

Chapter 1

Quantum Chromodynamics

The Quantum Chromodynamics (QCD) is the underlying theory of the phenomena being investigated at the Relativistic Heavy Ion Collider (RHIC). After a brief historical introduction the basics of QCD are described.

1.1 Historical introduction

The whole subject of nuclear physics has just marked only its 100th anniversary. Indeed, it was in 1911 when Ernest Rutherford discovered atomic nucleus by scattering α-particles off golden foil [6]. Further development in nuclear and particle physics in 1930s was paved by discoveries of new particles (in 1932 alone, positron and neutron were discovered [7, 8]) and by theoretical advancements: in 1934 a particle of a mass of approximately 100 MeV mediating the strong interaction was conjectured by Yukawa. The independence of nuclear forces of the nucleon charge led to the concept of isospin. The concept of the particle-mediated strong force invariant under transformation in the isospin space paved the way to unitary symmetry, quark model and eventually Quantum Chromodynamics.

The discovery of the so called "V" particles (today Λ^0, K^0_s) in 1950s led to the introduction of *strangeness*, a quantum number conserved in the strong interaction. Strangeness and isospin symmetry gave rise to the concept of $SU(3)$ flavor symmetry, leading to the prediction of further baryon states in both the octet and decouplet. The discovery of the Ω^- in the bubble chamber at BNL in 1964 [9] was a confirmation of $SU(3)$ flavor symmetry called by Gell-Mann the Eightfold Way [10, 11].

The *quark* model, that appeared soon after the Eightfold Way, described hadrons as composite objects made of constituent quarks - fermions - u, d, s and their antiquarks (mesons: $q\bar{q}$, baryons: qqq). However, and additional quantum number had to be present to satisfy the Fermi-Dirac statistics of fermionic quarks: the Δ^{++} with spin $+3/2$ is composed of 3 quarks of the same flavor (u) and spin ($+1/2$). This

problem was resolved in 1965 by assigning quark an additional quantum number: *color*, or color charge. Quark has one of three possible values of color charge: Red, Green, Blue and the hadrons are formed in such a way that their total color charge is zero (they are color-less objects). Colored quarks are *confined* to hadrons and a free quark (colored object) can not exist separately. Experimental search for a free quark (signature would be observation of a particle with fractional electric charge) has not been successful so far [12], in accordance with the concept of confinement.

Experiments with electron beams at SLAC facility in 1960s studying the internal structure of nucleon led to the discovery of *partons* (parton: part-of-proton). Many similarities between quarks (which were mostly mathematical objects) and partons led to their partial identification and to the concept of quark-parton model of hadrons. In the 1970s, two additional heavy quarks were discovered: c (charm, 1974) and b (bottom, 1977). Being very heavy, the top quark was only discovered in 1995, completing the third generation of quarks. The properties of the 6 quarks are briefly summarized in Table 1.1.

generation	quark	flavor	mass[MeV/c^2]	charge
First	u	up	1.3-3.0	$\frac{2}{3}$
	d	down	3-7	$-\frac{1}{3}$
Second	c	charm	1250±90	$\frac{2}{3}$
	s	strange	95±25	$-\frac{1}{3}$
Third	t	top	174200±3300	$\frac{2}{3}$
	b	bottom	4200±70	$-\frac{1}{3}$

Table 1.1: Main properties of quarks: mass (taken from [12]) and charge. Isospin is non-zero for u(+1/2) and d(-1/2) quarks only. Additional quantum numbers are defined for the 2nd and the 3rd generation quarks: s quark has *strangeness*=-1, c quark has *charm*=+1 and bottom quark has *bottomness*=-1. The top quark decays before it can form a hadron.

Strong interaction between quarks is mediated by *gluons*. The Deep Inelasting Scattering (DIS, in most cases e+p collisions) measured that quarks only contribute to about half of proton momentum and the other half was attributed to gluons. Direct experimental evidence for gluons were the 3-jet events in electron-positron collisions at DESY [13].

A much more detailed historical introduction can be found in [14] which includes references to many original works that paved the road to the modern QCD.

1.2 QCD Lagrangian

Similar to Quantum electrodynamics (QED), QCD is a gauge field theory. In gauge field theories, the dynamics of the field (quark field in the case of QCD, electron field in the case of QED) described by the Lagrangian of a free fermion field:

$$\mathcal{L} = \overline{\Psi}(i\gamma^\mu \partial_\mu - m)\Psi \tag{1.1}$$

stems from the requirement of the invariance to the local gauge symmetry ($\Psi \rightarrow e^{i\Lambda(x)}\Psi$). It is realized by introducing the *gauge field* (photon in QED) that is included in the *covariant derivative* D_μ, which replaces ∂_μ in the Lagrangian. Working out the math gives the interaction term and the Lagrangian of QED has the following form:

$$\mathcal{L} = \overline{\Psi}(i\gamma^\mu \partial_\mu - m)\Psi - e\overline{\Psi}\gamma^\mu A_\mu \Psi - \frac{1}{4}F_{\mu\nu}F^{\mu\nu}, \tag{1.2}$$

where $F_{\mu\nu}$ is the gauge field tensor, which in QED has a value of $F_{\mu\nu} = \partial_\mu A_\nu - \partial_\nu A_\mu$.

The gauge symmetry group of QCD is $SU(3)_C$ (where C stands for color). Color plays a crucial role in the gauge transformation in QCD: $\Lambda(x) = \alpha_a(x)T_a$. T_a are the generators of $SU(3)$ group, related to well known Gell-Mann matrices λ_a: $T_a = \frac{1}{2}\lambda_a$. The resulting covariant derivative for QCD has the following form:

$$D_\mu = \partial_\mu - igA^a_\mu T_a, \tag{1.3}$$

where a = 1,...,8 is the index marking the color of the gluon involved, and g is the coupling constant (that replaces e in QED Lagrangian).

Due to the fact that generators of $SU(3)$ do not commute (and QCD is hence a non-Abelian gauge field theory), an extra term has to be added into field tensor $F_{\mu\nu}$ to make the last term in Eq. (1.2) gauge invariant.

$$F^a_{\mu\nu,QCD} = \partial_\mu A^a_\nu - \partial_\nu A^a_\mu + g f_{abc} A^b_\mu A^c_\nu, \tag{1.4}$$

where f_{abc} are the structure constants of $SU(3)$. Inserting Eq. (1.4) into the last term in the Lagrangian (Eq. (1.2)) gives rise to new interaction terms: in addition to the QED-like interaction of 2 quarks with gluon, there are *self-interactions* of gluons: 3- and 4-gluon interactions. The 3 interaction vertices of QCD are shown in Figure 1.1.

1.3 Asymptotic freedom and perturbative QCD

The $SU(3)$ group is non-Abelian and one of its consequences is the gluon self-interaction. This in turn has profound consequences in perturbative solution of

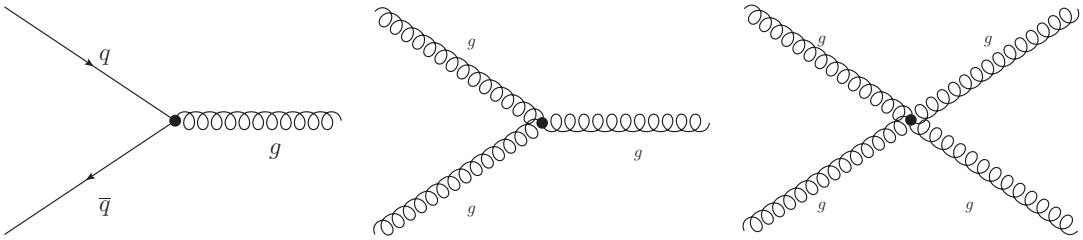

Figure 1.1: Interaction vertices of QCD: QED-like qqg vertex and 3-,4- gluon interaction vertices.

QCD when higher order diagrams are considered and renormalization is calculated. In the leading order (LO) perturbative expansion of QED, the coupling as a function of 4-momentum transfer q^2 behaves according to:

$$g^2_{\mathrm{QED}}(q^2) = \frac{4\pi\alpha}{1 - \frac{2}{3}\frac{\alpha}{4\pi}\ln\left(\frac{q^2}{m_e^2}\right)}, \tag{1.5}$$

where $\alpha = \frac{g^2(q^2=0)}{4\pi} \approx \frac{1}{137}$ is the fine structure constant. In other words, at large distances (small q^2) there is a screening of the electric charge and the interaction is weaker.

In QCD, on the other hand, the diagrams containing gluon loops cause the opposite asymptotic behavior. The renormalization of QCD coupling at leading order gives:

$$g^2_{\mathrm{QCD}}(q^2) = \frac{g^2(\Lambda^2)}{1 + 9\frac{g^2(\Lambda^2)}{(4\pi)^2}\ln\left(\frac{q^2}{\Lambda^2}\right)}, \tag{1.6}$$

where Λ is a scale introduced in the renormalization process. Compared to the case of QED, the coupling *decreases* at small distances (i.e., with increasing momentum transfer) and goes to zero for $Q^2 \to \infty$. This behavior of QCD is called *asymptotic freedom*. It was discovered in 1973 by Gross, Wilczek and Politzer [15, 16] and awarded with the Nobel Price in 2004. Unlike QED, QCD exhibits *antiscreening* of color charge.

A typical scale for measurements and calculations of the strong coupling constant $\alpha_s(q^2) = g^2(q^2)/4\pi$ is at the mass of the Z^0 boson ($M_{Z^0} = 91.2$ GeV/c^2). The current world average is $\alpha_s(M_{Z^0}) = 0.1189 \pm 0.0010$ [17] and the summary of its measurements is shown if Figure 1.2.

Due to the running coupling α_s, the perturbative approach to solve QCD equations can be used for processes with large momentum transfers Q^2. The relevant scale here is Λ from Eq. (1.6) and its value is $\Lambda \approx 200$ MeV (however its precise definition and value depends on the details of renormalization scheme).

In high energy collisions effects beyond leading order perturbative expansion become important and many QCD calculations are therefore performed in higher

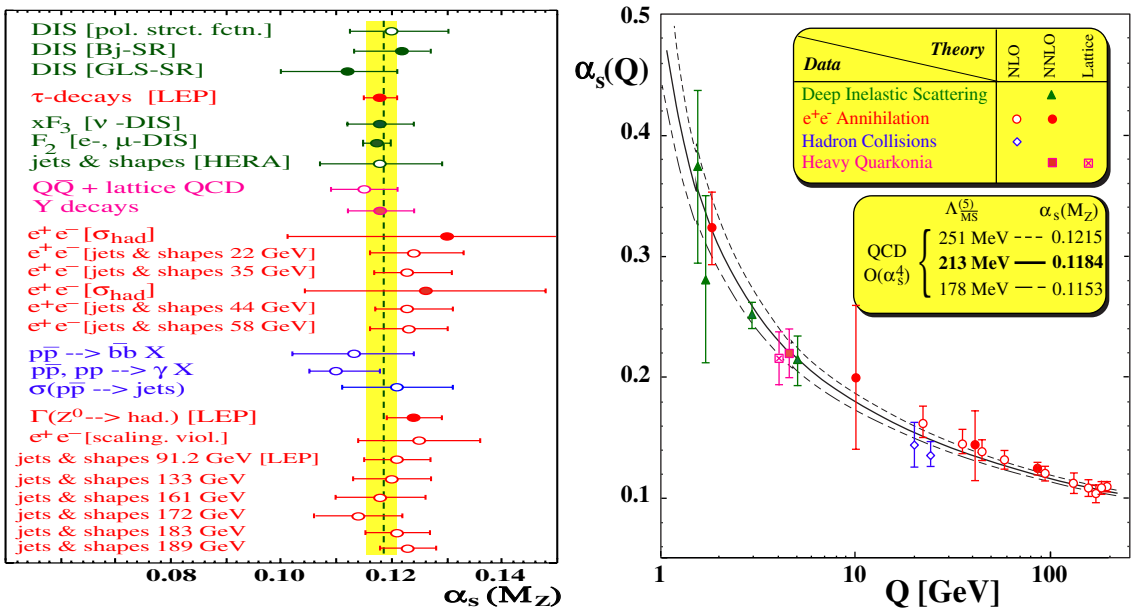

Figure 1.2: Left: Summary of measurements of QCD coupling $\alpha_s(M_Z)$. Right: The running coupling constant as a function of momentum transfer Q^2 determined from different processes. Taken from [17, 18].

orders of perturbation theory. For example the inclusive jet cross section in p+p collisions at $\sqrt{s} = 200$ GeV is well described by the next-to-leading order (NLO) pQCD calculation as shown in Figure 1.3. The higher order QCD processes in high energy particle collisions manifest themselves as multi-jet events. These can be studied exclusively or by measuring the so called Underlying Event (UE) that includes everything but the highest E_{T} jets in the event. Recent underlying event measurement in $\sqrt{s} = 200$ GeV p+p collisions at RHIC can be found in [19] together with references to UE measurements from the Tevatron.

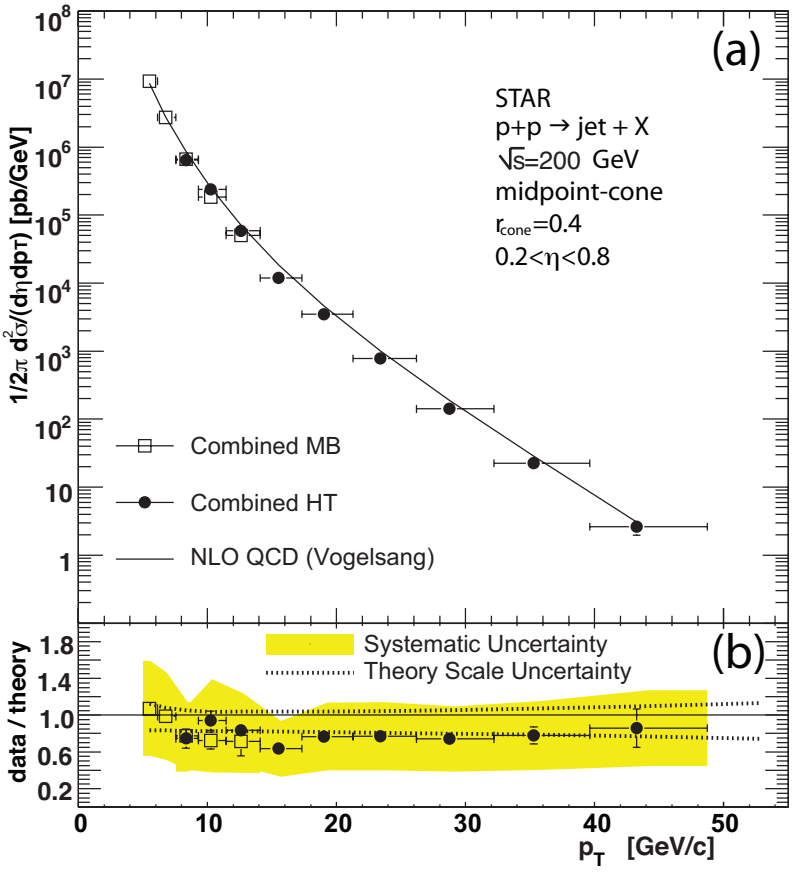

Figure 1.3: Jet p_{T} spectrum from $\sqrt{s} = 200$ GeV p+p collisions by STAR [20] and comparison to NLO pQCD calculation [21].

Chapter 2

Jet production in nuclear collisions

It is convenient to describe the initial state of high energy proton collision is the so called infinite momentum frame. Due to QCD, proton in this picture is not just an object made of two u and one d quarks (these are called valence quarks). Instead, it is described by its parton distribution function (PDF), which is a probability density $P(x)$ of finding a parton in proton with a momentum fraction x. It is defined for gluons ($G(x)$) and different quark flavors ($u(x)$, $d(x)$ etc.). Proton is a rather lively object, full of virtual gluons and quark-antiquark pairs. As QCD is quark-flavor blind, the following relations hold for PDFs of u and d quarks:

$$\begin{aligned} \int_0^1 (u(x) - \bar{u}(x))dx &= 2 \\ \int_0^1 (d(x) - \bar{d}(x))dx &= 1 \end{aligned} \tag{2.1}$$

2.1 Factorization

In processes with large Q^2 the characteristic time scale of the interaction is so small, that the interaction between partons (or photon and quark in case of DIS) factorizes from the subsequent evolution of the struck parton(s). The cross section for interaction of two protons producing particle F + anything can be thus written in a factorized form as:

$$\sigma_{p+p\to F+X} = \sum_{ijk} \int\int dx_1 dx_2 f_i(x_1) f_j(x_2) \sigma_{i+j\to k} \cdot D(k, F), \tag{2.2}$$

where $f_i(x_1)$ is proton PDF (probability of finding parton i with momentum fraction x_1 in proton) and $D(k, F)$ is the probability that parton k will hadronize into hadron

F (fragmentation function). $\sigma_{i+j\to k}$ is cross section of partonic interaction calculable in perturbative QCD.

Due to the possibility of quark radiating gluon or gluon turning into a quark-antiquark pair, depending on the momentum transfer Q^2, the PDF $f(x)$ and fragmentation function D in Eq. (2.2) acquire dependence on Q^2: $f_i = f_i(x, Q^2)$. Unlike the dependence of PDF on x which is a non-perturbative effect and has to be measured, the evolution of PDF with Q^2 for given x can be calculated using the DGLAP [1] [23, 24, 25] evolution equation:

$$Q^2 \frac{\partial f_i(x, Q^2)}{\partial Q^2} = \sum_j \int_x^1 \frac{dz}{z} \frac{\alpha_s}{2\pi} P_{ij}(z) f_j(\frac{x}{z}, Q^2), \tag{2.3}$$

where $P_{ij}(z)$ is the so called splitting function: the probability that parton j splits resulting into parton i with a momentum fraction z of the initial parton j. Quark can stay quark or can radiate gluon (which then interacts in the scattering process), gluon can stay gluon or can convert into quark-antiquark pair. Experimental measurements of PDFs and their theoretical study and extension to unmeasured Q^2 values led to establishment of standard sets of PDFs which are used in practical calculations of particle production: CTEQ [26], MRST [27], GRV [28].

Once a high energy parton emerges from the high-Q^2 scattering, it will first decrease its virtuality in partonic shower by radiating gluons (quark) of making $q - \bar{q}$ pairs (gluon). This initial development can be calculated by a DGLAP-like evolution. Once a non-perturbative scale is reached, a model of hadronization is required to turn the final state partons into hadrons. One of the models is the Lund string model that is used in PYTHIA [29]. Another approach is the independent fragmentation model, where the fragmentation function (probability of certain parton producing given hadron with some momentum fraction) is *measured* in electron-positron scattering, where the kinematics is much more under control than in p+p collisions.

The success of independent fragmentation model for charged pions can be seen in Figure 2.1, where a measurement of particle spectra in $\sqrt{s} = 200$ GeV p+p collisions from STAR is compared to the Next-to-Leading Order (NLO) QCD calculation. On the contrary, the theoretical result for the *proton* p_{T} spectrum in Figure 2.1 has large uncertainties coming from the choice of fragmentation function set.

2.2 Concept of jets

Quantum Chromodynamics has intrinsic infrared and collinear singularities which play an important role in the process of parton fragmentation into final state

[1] Dokshitzer,Gribov,Lipatov,Altarelli,Parisi

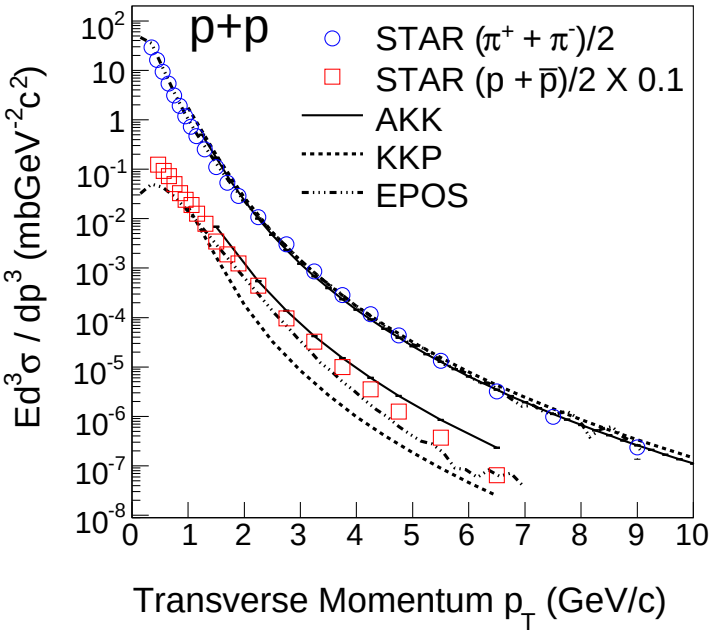

Figure 2.1: Midrapidity($|y| < 0.5$) p_{T} spectra for protons and charged pions measured in STAR experiment [22]. Contrary to protons the shape of the pion spectrum is less sensitive to the choice of different sets of fragmentation functions.

hadrons. To calculate hadron production cross-sections, fragmentation functions are needed. Due to their sensitivity to infrared singularities and other non-perturbative effects, the uncertainties of calculated hadron cross-sections are large.

The states with or without emission of soft or collinear gluons are degenerate, they have the same conserving quantum numbers and the same four momentum. Summing over these final states leads to the cancellation of the infrared and collinear singularities. The energy flow into given phasespace can thus be calculated in perturbative QCD and it is infrared and collinear safe quantity. This is a manifestation of a more general principle stated by the *Kinoshita-Lee-Nauenberg* (KLN) theorem [30, 31].

The application of the KLN theorem to parton fragmentation in QCD was described in [32] and guarantees its applicability to QCD *jets*. Jet is a collimated spray of hadrons (with some small fraction of photon radiation) originating from a single parton emerging from the hard scattering. Experimentally jets are reconstructed from the observed particles, so a model of fragmentation is still required if a correction is to be made to original parton level. However, the uncertainties on jet production coming from fragmentation models are much reduced compared to predictions for single particle spectra. Jet is therefore a proxy for the hard-scattered parton which is well defined both theoretically and experimentally and measure-

ment of jet production is one of the most sensitive tools for testing perturbative QCD.

An illustration of partonic kinematics in p+p collisions at RHIC ($\sqrt{s}$ = 200 GeV) is shown in Figure 2.2: jet production at $\sqrt{s} = 200$ GeV is dominated by the quark-gluon scattering for jet $p_{\mathrm{T}} < 30$ GeV/c. Importance of higher order QCD terms for p+p collisions at $\sqrt{s} = 200$ GeV is also shown in Figure 2.2.

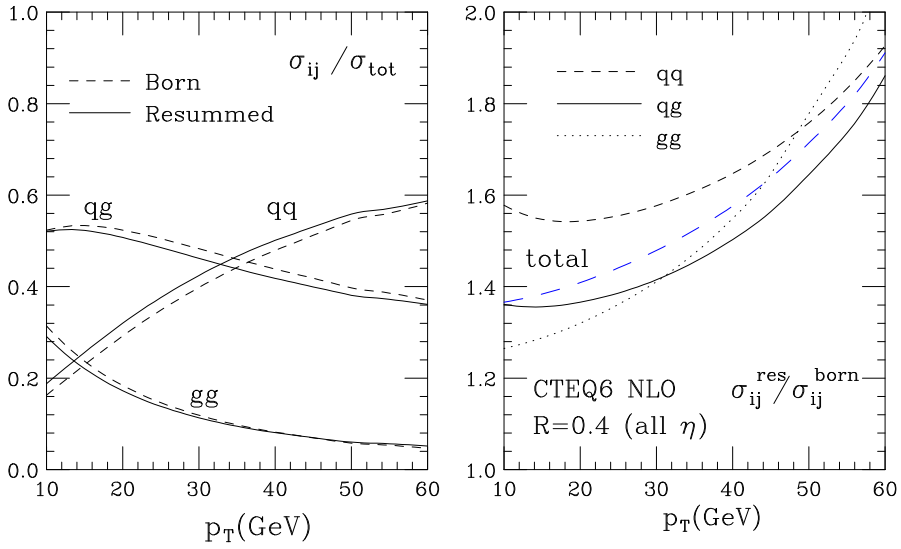

Figure 2.2: Left: Relative contribution of the various initial partonic configurations to the single inclusive jet cross section at $\sqrt{s} = 200$ GeV, at Born (leading order) and NLL level. Right: Importance of NLL resummation for various channels and the total. Taken from [33].

2.3 Jet algorithms

Jet algorithms are tools to assign the observed particles to jets, so that the jet properties (energy, direction etc.) best reflect the original parton. Given there are other particles produced in a p+p collision than those belonging to the jet of interest, there is ambiguity in this assignment. To compare experimental jet measurement to a theory prediction, the same jet algorithm therefore has to be run in both cases. There are two main classes of jet algorithms: cone algorithms and recombination algorithms. They act on detector objects (charged tracks, calorimeter clusters) characterized by their transverse energy or momentum ($E_{\mathrm{T}}, p_{\mathrm{T}}$) and direction (azimuthal angle ϕ defined in the plane perpendicular to the colliding beams and pseudorapidity η [2]). A recombination scheme must be chosen to define how jet

[2] pseudorapidity is defined as $\eta = -\ln(\tan(\theta/2))$, where θ is the angle with respect to the beam axis

4-momentum is determined form the 4-momenta of jet constituents. In this work, an *E-scheme* with massless particles is used: jet constituents are assumed massless and their 4-momenta are summed to obtain the jet 4-momentum.

Since the gluon radiation in jet fragmentation involves collinear and infrared divergences, a good jet algorithm should be safe with respect to these [34] (this property is referred to as *IRC safety*, coming from infrared and collinear). As an illustration consider a simple cone jet algorithm with a seed energy above some threshold. If the particle (or its originating parton) splits into two collinear particles, each with half of the initial energy, they may fall below the seed threshold. Also, soft particle emitted between two jets could influence reconstruction of those jets (for example merging them into one which would not have occurred without this soft particle). In other words, a simple cone algorithm is not IRC safe. Collinear safety is not an issue for cone jet algorithm as long as the seed threshold is much lower than the jet energies of interest. Also if calorimetry is used, there is limited sensitivity to angular separation of particles, so the calorimeter lateral segmentation works as a natural regulator of the collinear divergence.

Cone jet algorithms define jets as object inside a cone with radius R in $\eta - \phi$ space. *Protojets* are iteratively defined as cones with radius R in such a way that their momentum (sum of constituent momenta) coincides with the cone axis. To simplify this computationally difficult task [3], many cone algorithms are seeded: only seeds (tracks/towers with $E_{\mathrm{T}} > E_{\mathrm{T},cut}$) are used to determine the initial position of protojets. To overcome the obvious (IRC-safety-related) dependence on the seed cut $E_{\mathrm{T},cut}$, the Mid Point Cone (MPC) algorithm [34] (used at Tevatron and at RHIC) makes protojets also around the midpoints between the seeds in the $\eta - \phi$ plane. Finally, protojets that share some of their constituents have to be split/merged. In the MPC, the jets are merged if the shared energy exceeds fraction f of the lower-energy jets (in STAR, the value used is $f = 0.5$). Figure 1.3 shows that the jet spectrum from p+p collisions at STAR reconstructed with the MPC algorithm is in a good agreement with NLO theory prediction [20, 21]. This NLO calculation was performed using the CTEQ6M parton distribution functions [36].

The Gaussian filter [37, 38] is a cone-type jet algorithm that assigns different weights to the jet constituents based on their distance from the jet axis. This approach is favorable in the environments with large underlying event backgrounds, such as heavy-ion collisions where it can be naturally extended to allow a simple yet powerful discrimination of the so called *fake jets*. This approach is used by the PHENIX experiment at RHIC [39].

Unlike cone-type jet algorithms, sequential recombination jet algorithms do not have an a priori prescribed geometrical shape of the jet. They recombine in each step two closest entities in the new entity. At the beginning, the entities i are

[3] only recently, a fast seedless cone algorithm SISCone [35] appeared

the detector objects (particles/partons in case of a theory). The recombination is controlled by the definition of the distance measure d_{ij} between entities i and j:

$$d_{ij} = \min(p_{\mathrm{T}i}^{2p}, p_{\mathrm{T}j}^{2p}) \frac{\Delta_{ij}^2}{R^2}, \tag{2.4}$$

where $p_{\mathrm{T}i}, p_{\mathrm{T}j}$ are transverse momenta of the particles, $\Delta_{ij}^2 = (\Delta\eta)^2 + (\Delta\phi)^2$ is the geometrical distance in $\eta - \phi$ plane, R is the cone radius-like *resolution parameter* and p is a parameter controlling the p_{T} dependence of the recombination (to be discussed later in more detail). Another quantity is defined for each entity, the distance to the beam:

$$d_{iB} = p_{\mathrm{T}i}^{2p} \tag{2.5}$$

In each step, d_{ij} and d_{iB} are calculated and the minimum is found. If d_{iB} is the minimum, entity i is a new jet. If d_{ij} is the minimum, entities i and j are merged. Given the absence of seeds and the sequential recombination, the algorithm is naturally IRC safe. A recent theoretical progress an its implementation in the FastJet package [40] has made this class of algorithms computationally much less intensive, which is very important especially in the environments with large number of particles.

Depending on the value of parameter p, the Eq. (2.4) leads to the the $\mathrm{k_T}$ jet algorithm [41] ($p = 1$), Cambridge-Aachen algorithm [42] ($p = 0$) or the $\mathrm{anti-k_T}$ jet algorithm [43] ($p = -1$). The $\mathrm{k_T}$ algorithm is in fact the DGLAP in reverse (the splitting probability depends inversely on the radiated gluon momentum and angle, giving rise to collinear and soft divergences). It has a very flexible shape: it is adaptable to both soft and hard radiation. As such, it is quite sensitive to underlying event/pile-up and so it is not very useful in the environment of high energy nuclear collisions (or high luminosity p+p running at the LHC). On the other hand, the $\mathrm{anti-k_T}$ algorithm is resilient to soft radiation and so retains quite regular (cone) jet shape even in the presence of large underlying event.

An important aspect of jets related to the possible contamination by underlying event and/or pile-up is the *jet area* [44]. It is especially important for the sequential recombination jet algorithms, where the jet boundary is a priori unknown. The *passive* jet area is determined via scanning the whole $\eta - \phi$ space by one *ghost* (very soft artificial particle) at a time and determining the probability it falls into a given jet.

Due to the infrared safety of sequential recombination algorithms, the ghost particles can not change the reconstructed jets (their real particle content). However the large density of underlying event and pile-up (composed of many soft particles) in a given event can considerably change the jet areas. The *active* jet area is introduced to estimate this effect better than the passive area does. The active

jet area is determined using a dense population of ghost particles in one event and calculating how many of them fall into a given jet.

In this work, the active jet areas are used to subtract the d+Au underlying event background (details to be discussed in Chapter 5). Figure 2.3 illustrates the active jet area for several jet algorithms, run at the same event. For anti $-$ $\mathrm{k_T}$ algorithm, the hard jets are mostly circular and the active area of one-particle jets equals to πR^2.

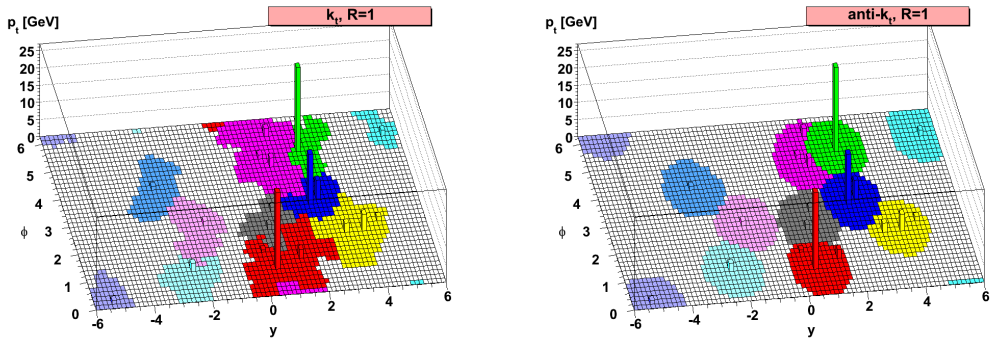

Figure 2.3: Active areas of $\mathrm{k_T}$ (a) and anti $-$ $\mathrm{k_T}$ (b) jets run at the same simulated event [43]. The anti $-$ $\mathrm{k_T}$ jets show roughly circular structure, while the $\mathrm{k_T}$ jets have flexible shapes.

2.4 Di-jet acoplanarity: k_{T} effect

Since the initial partons in a $2 \rightarrow 2$ hard scattering process are confined within the colliding protons, they have a transverse motion before the collision. As a result, the total transverse momentum $\vec{k}_{\mathrm{T}}$ of the outgoing parton pair is generally not zero. In other words, the two produced jets are not exactly back-to-back in azimuth (therefore they do not lie in the same plane with the axis of the colliding beams). This observation is usually referred to as di-jet acoplanarity or k_{T} effect [4]. Di-jet acoplanarity coming from partonic transverse motion within colliding protons is referred to as *intrinsic* k_{T}.

It was however realized [45] that intrinsic k_{T} alone does not explain the observed deviation of the transverse momentum (p_{T}) spectrum of produced particles from the naive pQCD expectation. It is the initial and final state radiation (ISR, FSR), that adds additional transverse kicks to the partons, resulting in the hardening of the observed p_{T} spectrum. A large part of the ISR, FSR is a soft gluon radiation that can not be calculated in pQCD, so a model is used in which the soft radiation

[4] to distinguish typographically the kt effect and the kt jet algorithm, the former is labeled k_{T} whereas the latter $\mathrm{k_T}$

is parametrized via a Gaussian k_{T} smearing with $\sigma_{k\mathrm{T}}$ as a parameter [46]. This is illustrated in Eq. (2.6) for a partonic process $ij \to kX$ with p_{T} being the transverse momentum of the final parton k:

$$\frac{d\sigma_{ij\to kX}(\vec{p}_{\mathrm{T,k}})}{d\vec{p}_{\mathrm{T,k}}} = \int \vec{k}_{\mathrm{T}} \int \vec{p}_{\mathrm{T}} \frac{1}{\sqrt{2\pi}\sigma_{k\mathrm{T}}} \exp(-\frac{k_{\mathrm{T}}^2}{2\sigma_{k\mathrm{T}}}) \delta(\vec{p}_{\mathrm{T,k}} - \vec{p}_{\mathrm{T}} - \vec{k}_{\mathrm{T}}) \frac{d\hat{\sigma}_{ij\to kX}(\vec{p}_{\mathrm{T}})}{d\vec{p}_{\mathrm{T}}}, \tag{2.6}$$

where $\frac{d\hat{\sigma}_{ij\to kX}(\vec{p}_{\mathrm{T}})}{d\vec{p}_{\mathrm{T}}}$ is calculated assuming total transverse momentum of the two partons involved is zero.

Hard pQCD (NLO) radiation is also involved in ISR, FSR, so the total k_{T} consists in fact of three parts:

$$k_{\mathrm{T}} = k_{\mathrm{T,intrinsic}} \oplus k_{\mathrm{T,soft}} \oplus k_{\mathrm{T,NLO}} \tag{2.7}$$

The hard NLO radiation presents itself as non-Gaussian power-law tails in the distribution of the 2-parton transverse momentum. Therefore the Gaussian k_{T} model is only applicable for small enough values of $|\vec{k}_{\mathrm{T}}|$ where the intrinsic and soft radiation parts are dominant.

2.5 Nuclear effects

High energy collisions involving nuclei (A+B) could naively be regarded as a simple superposition of nucleon-nucleon collisions and would only require the knowledge of the nuclear geometry (to be discussed in more detail in Subsection 2.5.2). In 1977 an observation [47] of nuclear effects in proton-nucleus collisions at Fermilab, referred to as *Cronin effect* was made, showing excess of production of large transverse momentum hadrons ($p_{\mathrm{T}} > 2$ GeV/c) over the expectation from proton-proton collisions. In 1980, Shuryak came up with the idea [48] of using heavy-ion collisions to reach and study the deconfined phase of QCD matter, that would result from the high energy densities created in ultrarelativistic heavy-ion collisions.

2.5.1 Cold nuclear matter effects

In addition to the Cronin effect, several other effects were observed in proton (deuteron) scattering off nuclei and in DIS on the nuclear target. Unlike the case of heavy-ion collisions, where *hot* QCD medium is likely produced, the nuclear matter involved in d+Au collisions is regular (cold), hence the term Cold Nuclear Matter (CNM) effects.

At low transverse momentum $p_{\mathrm{T}} < 1$ GeV/c a deficit of hadron production was observed with respect to expectation from p+p collisions. This is *shadowing*, a

deficit of low-x partons in the nucleus or, in other words, a modification of PDFs for nucleons in nucleus. The basis for shadowing is the fact that low-x partons have large dimensions, so are likely to interact with partons from the neighboring nucleons and possibly recombine to a parton with larger x. As a consequence, there is excess of partons at larger x, the *anti-shadowing*. One of the early reviews and a pQCD-based explanation of shadowing and anti-shadowing can be found in [49]. The European Muon Collaboration at CERN observed a modification of PDF in nucleus at large x [50]: a deficit of partons with $x > 0.5$ observed in muon DIS on iron target in comparison to deuterium target. This effect is called *EMC effect* and it has not been completely theoretically explained.

Currently these nuclear effects on PDF are parametrized in the sets of nuclear parton distribution functions (nPDF), for example the EPS08 [51]. They are based on DIS and fixed target nuclear experiments as well as on d+Au data from RHIC at both midrapidity and forward rapidity. Figure 2.4 shows the nuclear modification of parton distribution functions (ratio $PDF(A)/PDF(A=1)$) for different values of A. For heavy nuclei (lead $A = 208$, gold $A = 197$) the low x modification of gluon PDF is very strong, but this region is out of the reach of this analysis.

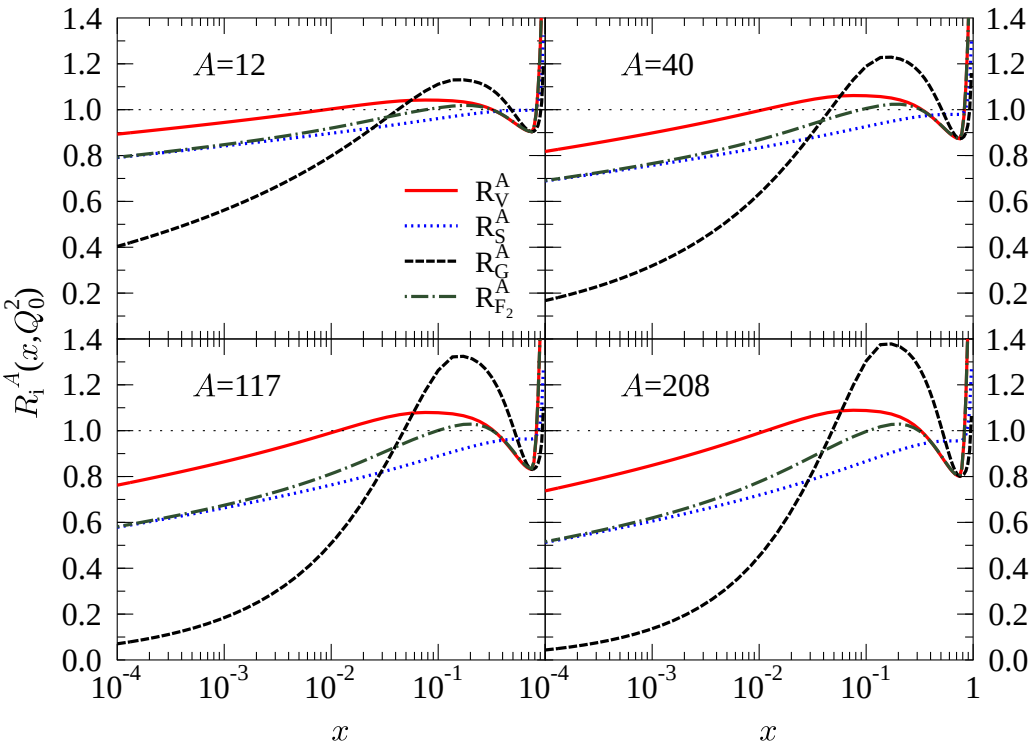

Figure 2.4: Nuclear modification (ratio $PDF(A)/PDF(A=1)$) for valence quarks, sea quarks, gluons and the corresponding DIS structure function modification as parametrized in the EPS08 nPDF set, for $Q_0^2 = 1.69$ GeV^2. Taken from [51]

It is instructive to derive the kinematics for $2 \rightarrow 2$ partonic process, that is observed as di-jet: pair of jets each with transverse momentum p_{T} and pseudorapidities η_3 and η_4 (starting in the center-of-mass system, where the jets are back-to-back). The formulas for x_1 and x_2 turn out as:

$$x_1 = \frac{p_{\mathrm{T}}}{\sqrt{s}}(e^{\eta_3} + e^{\eta_4})$$
$$x_2 = \frac{p_{\mathrm{T}}}{\sqrt{s}}(e^{-\eta_3} + e^{-\eta_4}) \tag{2.8}$$

In the presented analysis, the pseudorapidity acceptance of jets is $|\eta| < 0.55$. The accessible p_{T} range for jets in d+Au collisions is $10 - 30$ GeV/c, setting the accessible x range to $0.05 - 0.5$, the region of anti-shadowing.

Nuclear modification of PDFs does not seem to be sufficient to describe the high-p_{T} phenomena such as Cronin effect. The missing ingredients is the rescattering (before or after the hard process) in the nuclear matter. It can be described by several models with hadronic or partonic degrees of freedom [52]. Unlike the modification of PDF, the rescattering not only influences the *spectra* of produced particles, but also their azimuthal correlations. It is the k_{T} which will inevitably rise as a consequence of rescattering in nuclear matter (the soft and NLO parts of k_{T} as defined in Eq. (2.7) will obtain additional contributions from cold nuclear matter). One of the main goals of this work (to be discussed in detail in Chapter 7) is the comparison of k_{T} between p+p and d+Au collisions at $\sqrt{s_{\mathrm{NN}}} = 200$ GeV to quantify the possible nuclear effects.

2.5.2 Scaling of particle production in nuclear collisions

To quantify the differences in particle production (such as spectra) between p+p and A+B collisions, it is essential to have a good model for the initial geometry of the nuclear collision. The Glauber model (a recent review can be found in [53]) treats nucleus as superposition of nucleons and can be used for any collisions involving nuclei (d+Au, Cu+Cu, Au+Au in the case of RHIC). A nucleon-nucleon inelastic cross-section (slowly rising with the collision energy) allows to determine the average number of *binary collisions* $\langle N_{bin} \rangle$ and *participants* $\langle N_{part} \rangle$ for given impact parameter. Participant nucleon is a nucleon that underwent at least one inelastic collisions. The nucleons not participating in any collisions are called *spectators*. Collisions at small impact parameter have high number of participants and are called *central*, large impact parameter collisions are *peripheral*. Given the two-dimensional nature of impact parameter, very central collisions are rare.

Number of particles produced in the collision rises with both N_{bin} and N_{part}. In

Au+Au collisions at RHIC the fraction x_{hard} of particles produced in hard processes (i.e. scaling with $\langle N_{bin}\rangle$) is $\approx 10\%$. The value of x_{hard} was determined by fitting the multiplicity distribution coming from Glauber MC simulation to the multiplicity distribution in real data. The values of $\langle N_{bin}\rangle$ and $\langle N_{part}\rangle$ for centrality quantiles are then determined using the Glauber MC simulation. For example, 0-10% most central Au+Au collisions at $\sqrt{s_{\rm NN}} = 200$ GeV have $\langle N_{bin}\rangle = 940 \pm 68$, $\langle N_{part}\rangle = 326 \pm 5$. More details on the Glauber model and its implementation in d+Au collisions at RHIC can be found in Section 5.2 and in Appendix A.

To quantify the nuclear effects on produced particle spectra, the *nuclear modification factor* $R_{\rm AA}$ is used:

$$R_{\rm AA}(\eta, p_{\rm T}) = \frac{\frac{1}{\langle N_{bin}\rangle}\frac{1}{N_{events}}\frac{d^2N_{\rm A+A}}{d\eta dp_{\rm T}}}{\frac{1}{\sigma^{inel}_{\rm p+p}}\frac{d^2\sigma_{\rm p+p}}{d\eta dp_{\rm T}}}, \tag{2.9}$$

where $\frac{1}{N_{evts}}\frac{d^2N_{\rm A+A}}{d\eta dp_{\rm T}}$ is the per-event yield in A+A collisions, $\frac{d^2\sigma_{\rm p+p}}{d\eta dp_{\rm T}}$ is the cross section measured in p+p collisions and $\sigma^{inel}_{\rm p+p}$ is the inelastic p+p cross section. In the case of incoherent superposition of nucleon-nucleon collisions [5], the particle production in A+A collision scales with $\langle N_{bin}\rangle$ and $R_{\rm AA} = 1$ (with the exceptions of processes with QED vertex like direct photon production at very high $p_{\rm T}$, where valence quark differences between protons and neutrons start to play a role).

Given detector and trigger configurations in different RHIC runs and RHIC running schedule, the p+p reference measurement may not be available or has limited statistical precision. In this case, a $\langle N_{bin}\rangle$ scaled ratio of spectra in central and peripheral collisions, $R_{\rm CP}$, is often studied:

$$R_{\rm CP}(\eta, p_{\rm T}) = \frac{\frac{1}{\langle N_{bin}\rangle_{cent}}\frac{1}{N_{evts,cent}}\frac{d^2N_{cent}}{d\eta dp_{\rm T}}}{\frac{1}{\langle N_{bin}\rangle_{per}}\frac{1}{N_{evts,per}}\frac{d^2N_{per}}{d\eta dp_{\rm T}}} \tag{2.10}$$

2.5.3 Energy loss in QCD matter and jet quenching

The basic ingredient of any model of traversal of hot QCD medium (created in heavy-ion collisions) by a light quark or gluon is the *radiative energy loss* [54, 55]. It is described as gluon radiation induced by the medium (static scattering centers with some time-dependent density profile). For heavy quarks - c, b - the *collisional* energy loss may also be important. Energy loss is in fact a transfer of energy of the parton to the medium which manifests itself as increased production of soft particles.

The idea of jet reconstruction in heavy-ion collisions is to study this energy flow that goes to the medium (at least part of it will end up in the jet cone). There

[5] this is applicable to hard processes, whose typical time scales $\tau \propto 1/p_{\rm T}$ are short

are many models incorporating radiative energy loss in heavy-ion collisions, differing in medium description and in the scales involved (multiple soft emissions or a few hard scatterings in the medium etc.): BDMPS [56], ASW [57], GLV [58], AMY [59], Higher Twist [60, 61]. To connect the theory to experimental results, many Monte Carlo based codes were developed recently - for example JEWEL [62], QPYTHIA [63], YAJEM [64]. Recent review of theoretical concepts and experimental observations related to jet quenching can be found in [65].

As a result of partonic energy loss, the leading jet fragments have reduced p_{T}, which results into *suppression* of production of high p_{T} hadrons, referred to as *jet quenching*. This phenomenon was initial observed in $\sqrt{s_{\mathrm{NN}}} = 130$ GeV Au+Au collisions at RHIC [66], showing a suppression by factor 4 for production of high-p_{T} π^0. Many more measurements have been done at RHIC nominal energy $\sqrt{s_{\mathrm{NN}}} =$ 200 GeV, including measurements of direct photons which do not interact with the medium and their R_{AA} should therefore be 1, as opposed to factor ≈ 5 suppression of π^0. The R_{AA} of direct photons is shown in Figure 2.5 together with π^0 and η mesons, confirming this expectation. This justifies the use of R_{AA} to measure nuclear modification of particle production.

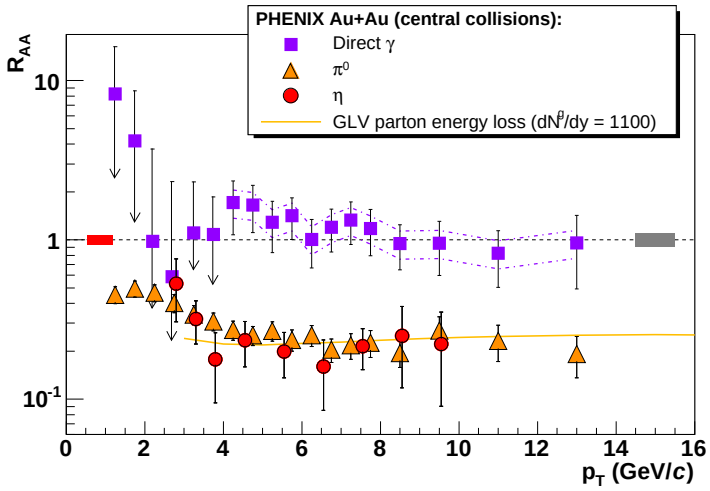

Figure 2.5: Nuclear modification factor of hadrons (π^0, η) and direct photons in Au+Au collisions by the PHENIX experiment at RHIC [80].

Another observation related to jet quenching is the absence of away-side peak in the azimuthal correlation of high-p_{T} hadrons [6] in central Au+Au collisions [3], shown in Figure 2.6. Figure 2.7 shows the result of simulation of the jet propagation in the medium created in heavy-ion collisions. It can be seen that the observed high-p_{T} hadrons come preferentially from hard scattering processes near the surface of the medium, so the away side jet traverses almost the whole medium and is eventually quenched.

[6] referred to as *di-hadron* analysis

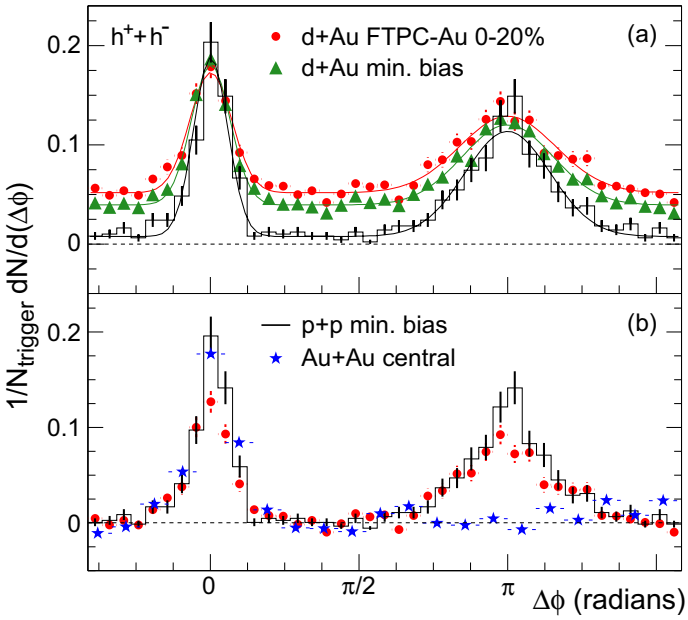

Figure 2.6: Di-hadron correlations for p+p, d+Au and Au+Au collisions from the STAR experiment [4]. The trigger is in range $4 < p_{\mathrm{T},trig} < 6$ GeV/c and the associated particle in range 2 GeV/$c < p_{\mathrm{T},asso} < p_{\mathrm{T},trig}$.

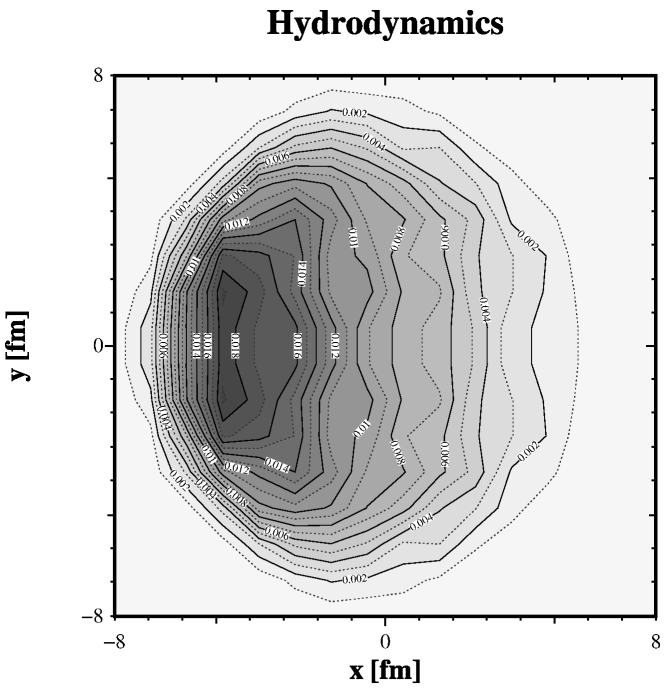

Figure 2.7: Probability density of finding a parton production vertex at (x,y) coordinates in the created QGP-like medium, given an event contains a high-p_{T} ($p_{\mathrm{T}} > 8$ GeV/c) hadron, propagating to the -x direction. Taken from [81].

It has to be noted however, that both R_{AA} and absence of away side peak could be explained by models involving initial state effects described in the previous subsection (such as strong shadowing of gluons in gold nucleus [67]). A review of the expectations for the reference d+Au measurements at RHIC can be found in [68].

In 2003, the d+Au run at RHIC helped resolve this observation and indeed showed, that these effects are caused mainly by the *final* state, that is by jet quenching in a hot and dense medium that is produced in central Au+Au collisions. Figure 2.8 shows only a minor nuclear modification of hadron spectra in d+Au collisions (Cronin effect), and the $\Delta\phi$ correlation shapes in Figure 2.6 show only very minor width modification in d+Au compared to p+p as opposed to the striking disappearance of the away side jet peak in central Au+Au collisions. This means that the initial state effects play only a very small role in these observables in Au+Au collisions.

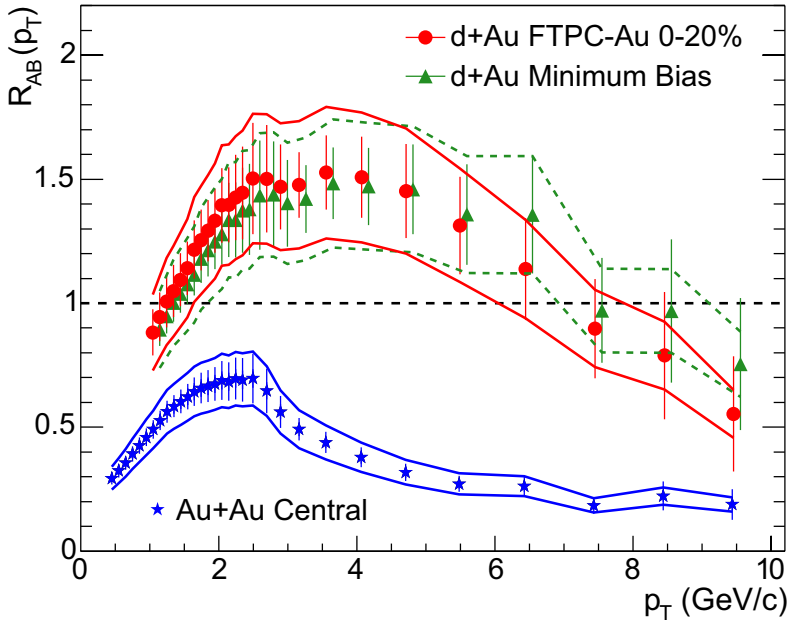

Figure 2.8: Nuclear modification factors of charged hadrons in d+Au and Au+Au collisions from the STAR experiment at RHIC [4].

However at very high p_{T} energy loss may start to play important role even in d+Au collisions. It was shown by the PHENIX collaboration, that there is a sizeable suppression of π^0 production in central d+Au collisions for $p_{\mathrm{T}} > 10$ GeV/c [69]. This can not be explained by PDF modification in nuclei, neither by rescattering (that has minor role at this high p_{T} and would lead to enhancement). The authors of [70] suggest that this observation may be due to energy loss in cold nuclear matter.

Developments in theory [40, 43, 44, 71] and experiment (STAR detector calorimetry upgrades and increased RHIC luminosity) finally enabled full jet re-

construction in heavy-ion collisions [72, 73]. Full jet reconstruction reduces the biases of indirect measurements and enables access to qualitatively new observables such jet profile and energy flow.

Figure 2.9 shows the nuclear modification factor of jets in 0-10% most central Au+Au collisions for two values of R parameter and for $\mathrm{k_T}$, anti $-$ $\mathrm{k_T}$ jet algorithms [74]. The jets with $R = 0.4$ show sizeable recovery of the "lost" energy compared to the jets with $R = 0.2$ and to single particle R_{AA} (≈ 0.2 for $p_{\mathrm{T}} > 5$ GeV/c). This effect can be also quantified with ratios of jet p_{T} spectra with different resolution parameters. The ratios $R = 0.2/R = 0.4$ of jet p_{T} spectra in p+p and Au+Au collisions shown in Figure 2.10 are suggestive of jet profile broadening from $R = 0.2$ to $R = 0.4$ in most central Au+Au collisions with respect to p+p collisions. Study of di-jets in Au+Au collisions [75] is also consistent with the picture of jet profile broadening.

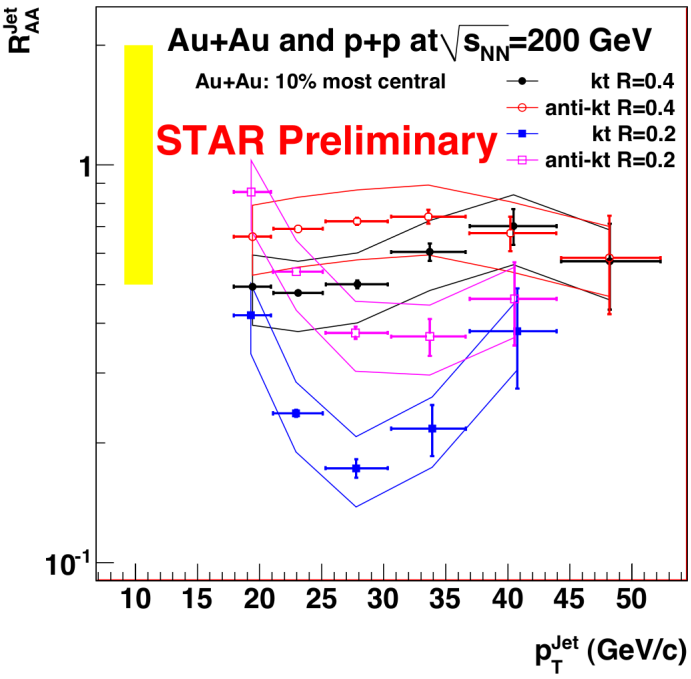

Figure 2.9: Nuclear modification factor R_{AA} for jets in Au+Au collisions [74]. Dependence on jet finder shows different sensitivity of $\mathrm{k_T}$ and anti $-$ $\mathrm{k_T}$ algorithms to the underlying event background.

A novel analysis method of jet modification in heavy-ion collisions, the *jet-hadron* correlations was presented in [76]. This analysis uses a fully reconstructed jet as a "trigger" in an azimuthal correlation study instead of a high-p_{T} particle used in di-hadron correlation analyses. It is studying possible jet modification by measuring charged hadrons on the away side ($\Delta\phi \approx \pi$ with respect to the trigger jet). Results

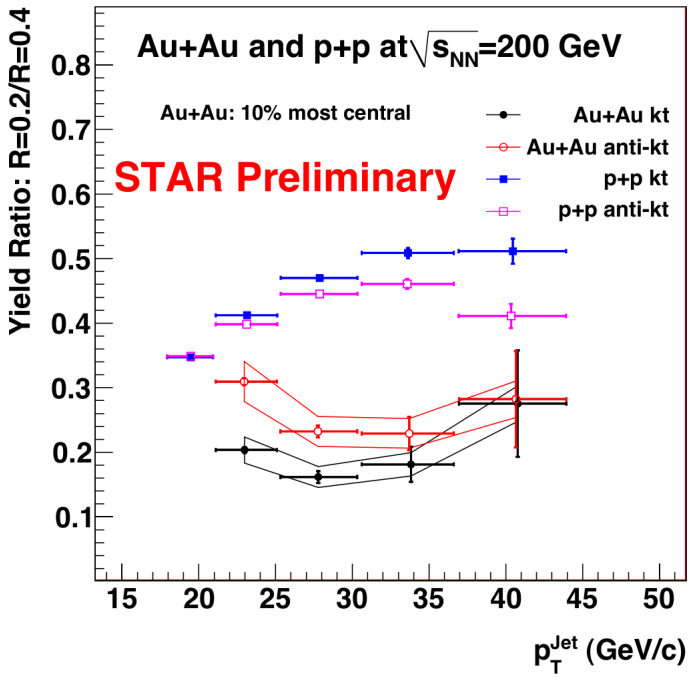

Figure 2.10: Ratio of the inclusive jet p_{T} spectra for different values of resolution parameter R [74]. Jet profile narrowing at high jet p_{T} is observed in p+p collisions, the jets in Au+Au collisions are much broader.

reported in [77] show signal consistent with jet broadening and softening due to radiative energy loss in the medium created in heavy-ion collisions.

A recent review of jet measurements in p+p, d+Au and Au+Au collisions at $\sqrt{s_{\mathrm{NN}}} = 200$ GeV from the STAR experiment can be found in [78, 79].

Chapter 3

STAR experiment at RHIC

The Relativistic Heavy Ion Collider (RHIC) [82] is located in the Brookhaven National Laboratory (BNL) on Long Island, NY, USA. For almost six decades, BNL has been on the forefront of high energy nuclear and particle physics research. This program is driven by the Alternating Gradient Synchrotron (AGS) that has been operating since 1960 and enabled research leading to three Nobel prizes in physics [1]. Apart from the fixed target experiments the AGS currently serves as an injector for Relativistic Heavy Ion Collider (RHIC). Approved in 1984, the construction of RHIC collider started in 1991 and the first Au+Au collisions for physics were provided in 2000.

In more than 10 years of its operation, the experiments at RHIC have collected huge amounts of physics data. The physics program at RHIC consists of 3 main branches: ultrarelativistic heavy-ion collisions (Au+Au,Cu+Cu), high energy spin physics (p+p collisions in various spin configurations) and investigation of initial state of nuclear collisions (d+Au). The STAR experiment [83] is one of the detectors collecting data from collisions provided by the RHIC collider.

3.1 Relativistic Heavy Ion Collider

The main goal of RHIC is study of QCD matter at extreme conditions. The collider provides collisions of heavy ions (various species up to uranium) for the research in phenomena like creation of QGP, QCD at high temperature and chiral symmetry restoration. Versatility of ion sources and the injection system allows to create asymmetric collisions such as d+Au (run in 2003 and 2007-2008) and Cu+Au (currently planned for 2012 or 2013). High energy spin physics is an important part of RHIC research program. RHIC can collide protons with both longitudinal and transverse polarization. The RHIC spin facility is described in detail in [84]. Apart

[1] 1976: S.Ting for J/Ψ discovery; 1980: J.Cronin and V.Fitch for CP violation; 1988: L.Lederman, M.Schwartz, J.Steinberger for discovery of muon neutrino

from spin physics, the p+p collisions serve also as a baseline to measurements done in d+Au and heavy-ion collisions.

The RHIC ion source and injection system is schematically depicted in Figure 3.1. The Tandem van de Graaf accelerator is used as ion source for RHIC [85]. In the case of Au nuclei, the negative ions (Au^{-1}) are produced by a pulsed sputter source [86] and accelerated by the 14 MV voltage of the Tandem. At this point they pass through a thin stripping foil removing 13 electrons and thus creating Au^{+13}. Accelerated back to the ground potential and passing through the second stripper foil they leave the Tandem. Through the Heavy Ion Transfer Line and the AGS Booster the beam reaches the AGS, where it is accelerated to 10 GeV/nucleon prior to injection to RHIC. In the case of deuterons, the sputter source is operated with TiO_2 cathode generating D^- ions. The Linac accelerator is used to produce protons in its hydrogen gas ion source and preaccelerate them prior to injection into the AGS Booster.

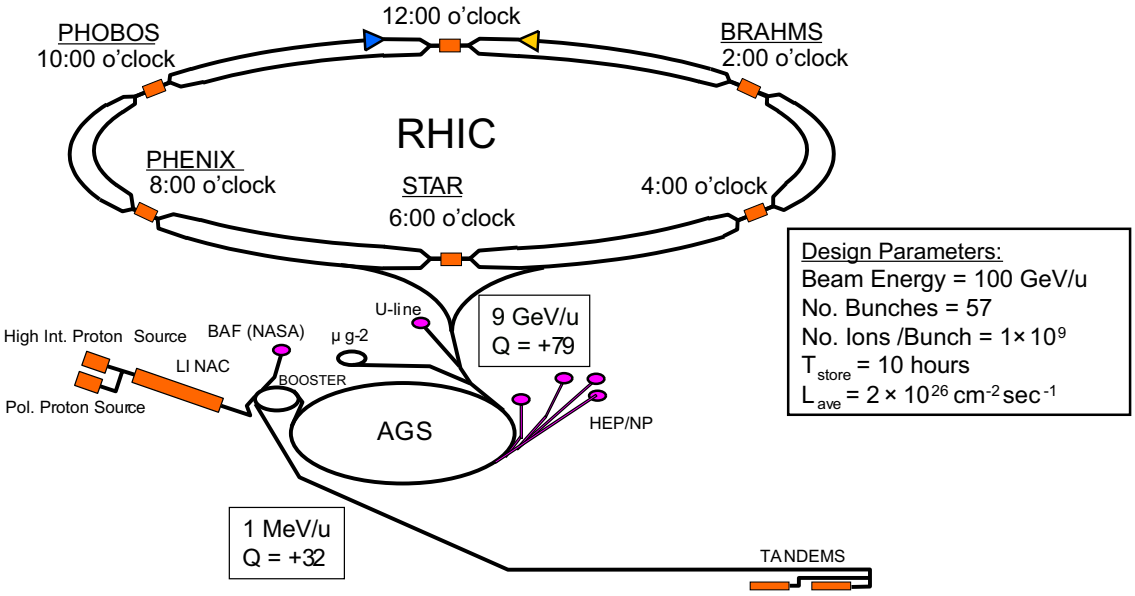

Figure 3.1: Scheme of the RHIC preaccelerator and injection system together with the RHIC collider and its experiments.

The RHIC collider consists of two concentric rings with circumference of 3.8 km, intersecting in 6 interaction points (IP). Three of them are currently occupied by running experiments: STAR, PHENIX and AnDY. Two smaller RHIC experiments, PHOBOS and BRAHMS, have already finished their operations. The maximum beam energy is 100 GeV/nucleon for Au nuclei and 250 GeV for protons. The key component of the rings are the 288 superconducting dipole magnets capable of producing magnetic field up to 3.5 T. They are typically operated with 120 bunches, giving the bunch crossing frequency of 10 MHz. In 11 years of its operation, numerous upgrades of the RHIC accelerator (such as stochastic beam cooling [87])

allowed to exceed the design luminosities and the luminosity is still being developed and improved. The luminosities achieved in 2011 [88] run were $50 \times 10^{26}\text{cm}^{-2}\text{s}^{-1}$ for Au+Au ($\sqrt{s_{\text{NN}}} = 200$ GeV) and $1.5 \times 10^{32}\text{cm}^{-2}\text{s}^{-1}$ for p+p ($\sqrt{s} = 500$ GeV).

3.2 STAR detector

The Solenoidal Tracker At RHIC (STAR) detector is a large multi-purpose experiment installed at 6 o'clock position at RHIC. It was built to study high-energy heavy-ion and proton-proton collisions at both mid- and forward-rapidity. The STAR coordinate system has its origin at the center of the IP. The z axis points to the west, the y axis points up and the x axis points outward from the RHIC ring (south). In the d+Au data taking, Au beam comes to the STAR IP from the west and deuteron beam comes from the east. All the mid-rapidity detector subsystems of STAR are located in a solenoidal magnet providing a field of 0.5 T. The mid-rapidity part of the STAR detector with several trigger detectors is shown in Figure 3.2.

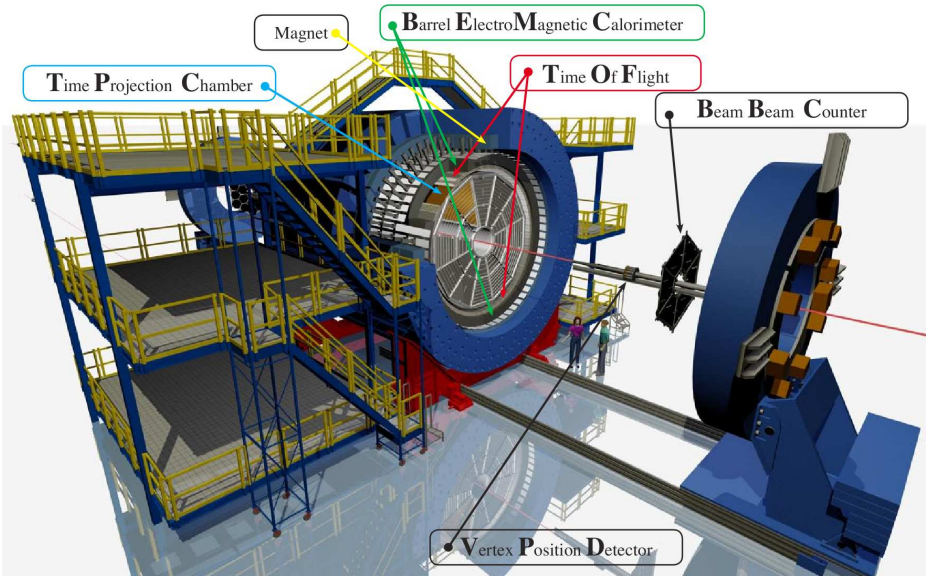

Figure 3.2: Schematic drawing of the central part of STAR. Picture courtesy of Alexander Schmah.

The detector systems used for the analysis presented in this thesis are the Time Projection Chamber and the Barrel Electromagnetic Calorimeter. The multiplicity of tracks in the east Forward Time Projection Chamber (FTPC) [89] ($-3.8 < \eta < -2.8$) is used to define centrality in d+Au collisions. Several trigger detectors are used to select events of interest and reduce the event rate from 150 kHz (d+Au interaction rate) to the nominal DAQ rate (50 Hz in 2007-2008 running).

3.2.1 Time Projection Chamber

The STAR Time Projection Chamber [90, 91] is one of the largest detectors of its kind ever built. The active volume of TPC is a 4.2 m long barrel with 0.5 m inner and 4 m outer diameter. For collision occurring at the center of the detector TPC covers pseudorapidity interval of $|\eta| < 1.8$ with full azimuthal coverage (given the TPC geometry, only tracks with $|\eta| < 1.3$ have enough reconstructed space points to achieve reconstruction quality needed for high-p_{T} tracks). The TPC is filled with P10 gas (10% Methane, 90% Argon) in which traversing particles leave ionization trail. The tracking volume is split in two, along the beam direction, with a high voltage cathode located at the center of the TPC. The cathode membrane is held at -28 kV and divides the detector into two separate drift regions. The chain of precision 2 MΩ resistors on the inner and outer field cage ensures the uniformity of the electric field of 135 V/cm in which the ionization electrons drift toward one of the endcaps with a velocity of 5.45 cm/μs. The maximum drift time is hence $\sim$ 40 μs. Maximum (i.e., for the maximum drift time) longitudinal diffusion of electrons is 5.2 mm. Lateral diffusion is reduced by the strong axial magnetic field and it maximum value is 3.2 mm. The TPC and its field cage is shown in Figure 3.3.

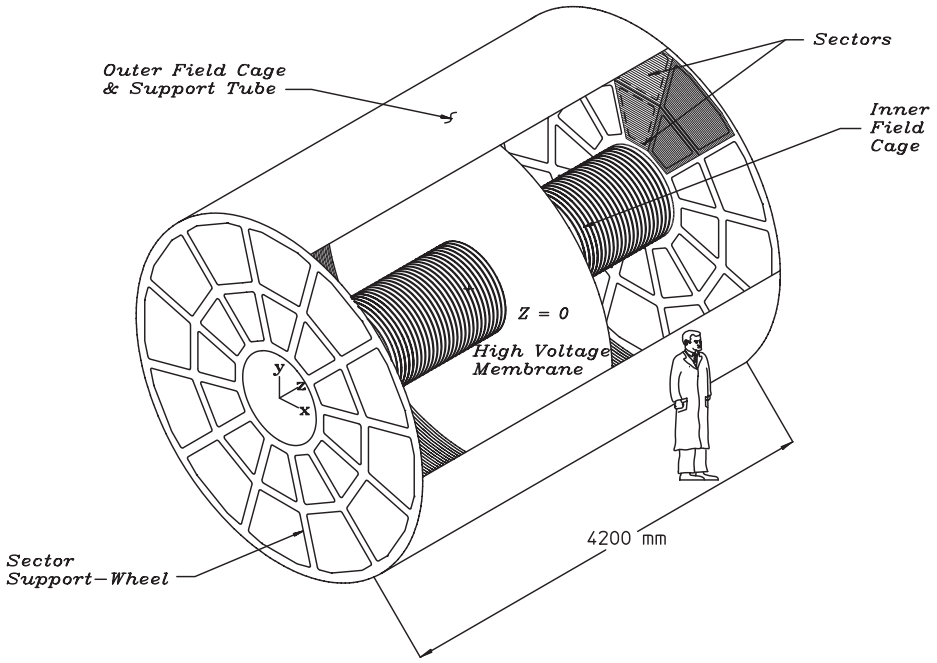

Figure 3.3: Diagram of the TPC field cage with central membrane (cathode) and endcaps (anodes). Taken from [91].

At each of the two TPC endcaps, 12 sectors with Multi Wire Proportional Chamber (MWPC) and cathode pad readout are mounted. As shown in Figure 3.4, there are three sets of wires. Unless the TPC is being read out, the *gating grid* is held in the closed state (the wires are alternately held at +75 V and −75 V from the equipotential value) to prevent electrons from the drift region from reaching the anode wires and positive ions to entering the TPC drift volume from the MWPC region. When a triggered event occurs, the gating grid is opened within 2 μs and the electrons reach the *anode* wires, which are held at +1000 V. The electron avalanche amplifies the signal $1000 - 3000$ times and the positive ions created in the avalanche induce signal on the readout pads, which then passes through preamplifier/shaper/digitizer system.

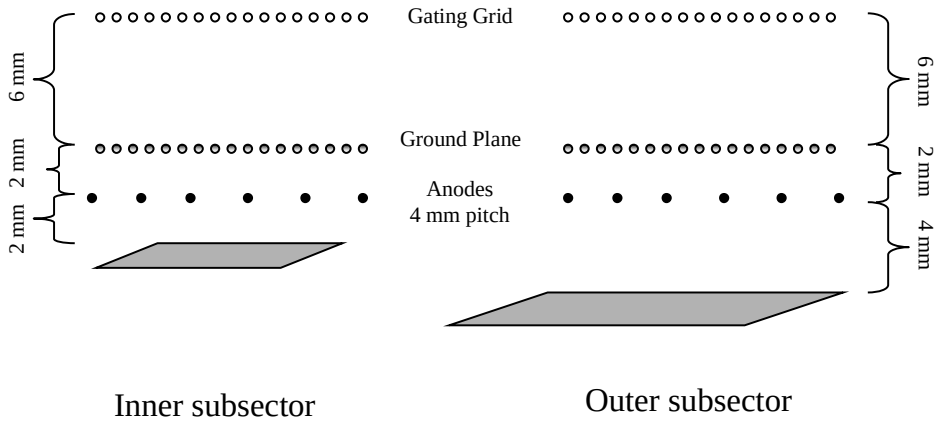

Figure 3.4: Schematics of the read-out part of the TPC endcaps. There are three sets of wires: gating grid (opened during readout of a triggered collison), ground plane and anode wires. Taken from [92].

Each sector is radially segmented into 45 padrows, which is also the maximum number of space points reconstructed for a charged track passing the volume of the TPC. The total number of TPC readout channels (pads) is $\sim 137,000$. The transverse momentum (p_{T}) resolution of a high-quality track with $p_{\mathrm{T}} = 10$ GeV/c is $\approx 10\%$ (without vertex constraint which leads to $\approx 5\%$). The quality of hit reconstruction is influenced by electric field distortions. In particular, *space charge* (slowly moving positive ions) created in the TPC volume causes apparent movement of reconstructed space points. This effect is becoming more pronounced as the RHIC luminosity is increasing and has to be accurately measured and corrected

for [93]. The p_{T} resolution and reliability of space charge correction allows for reconstruction of charged particle tracks up till $p_{\mathrm{T}} = 15$ GeV/c even in the high-luminosity environment of RHIC 2007-2008 d+Au run.

The precision measurement of track ionization energy loss in the TPC gas, dE/dx, also allows for powerful particle identification (not used in the jet reconstruction). Together with the TOF detector [94] it recently enabled STAR to publish the first observations of anti-alpha particle [95].

3.2.2 Barrel Electromagnetic Calorimeter

The Barrel Electromagnetic Calorimeter (BEMC) [96] is lead-scintillator sampling calorimeter covering $|\eta| < 1$ and full azimuth, surrounding the STAR TPC. It has a depth of about 20 radiation lengths (X_0) at $\eta = 0$. It is used to measure energy and position of incident particles (mainly electrons and photons) with energy resolution of $\frac{14\%}{\sqrt{E[\mathrm{GeV}]}} \oplus 1.5\%$. Thanks to its fast readout (scintillation signal with photomultipliers) the BEMC is used as L0 trigger detector to select events containing high p_{T} objects such as electrons, photons and jets.

The calorimeter consists of 120 modules, covering one unit of η and 0.1 rad in azimuth as shown in Figure 3.5. Each module contains two rows of 20 projective towers (covering 0.05×0.05 in $\Delta\eta \times \Delta\phi$ space), totaling 4800 towers in the BEMC. The inner two scintillators in each tower have a separate readout the *preshower* detector (PRS). The *shower max* detector (SMD) is located at the depth of $5X_0$. Both preshower and shower max detector can be used to distinguish electromagnetic and hadronic showers. The SMD detector can be used to separate the two γ from π^0 decay from a direct γ thanks to its fine $\Delta\eta \times \Delta\phi$ resolution (0.007×0.007). In the analysis of jets only the energies from the individual towers are used.

3.2.3 Trigger detectors

The Zero Degree Calorimeter (ZDC) [97] is a pair of tungsten-scintillator hadronic calorimeters positioned beyond the RHIC DX magnets that bend charged particles back to the beam pipes. It is thus sensitive to mainly spectator neutrons from the nuclear collisions. In d+Au collisions the signal in the east ZDC, in the fragmentation region of the Au nucleus, was used in the trigger.

The Beam Beam Counter (BBC) [98, 99] detector is a pair of scintillating counters in the pseudorapidity of $3.3 < |\eta| < 5.0$. The coincidence of the signals in the east and west BBCs forms a minimum bias trigger in p+p collisions with efficiency for non-singly diffractive events of $87 \pm 8\%$ [2]. The timing resolution of the BBC detector system does not allow to determine the primary vertex position to accuracy better than 40 cm.

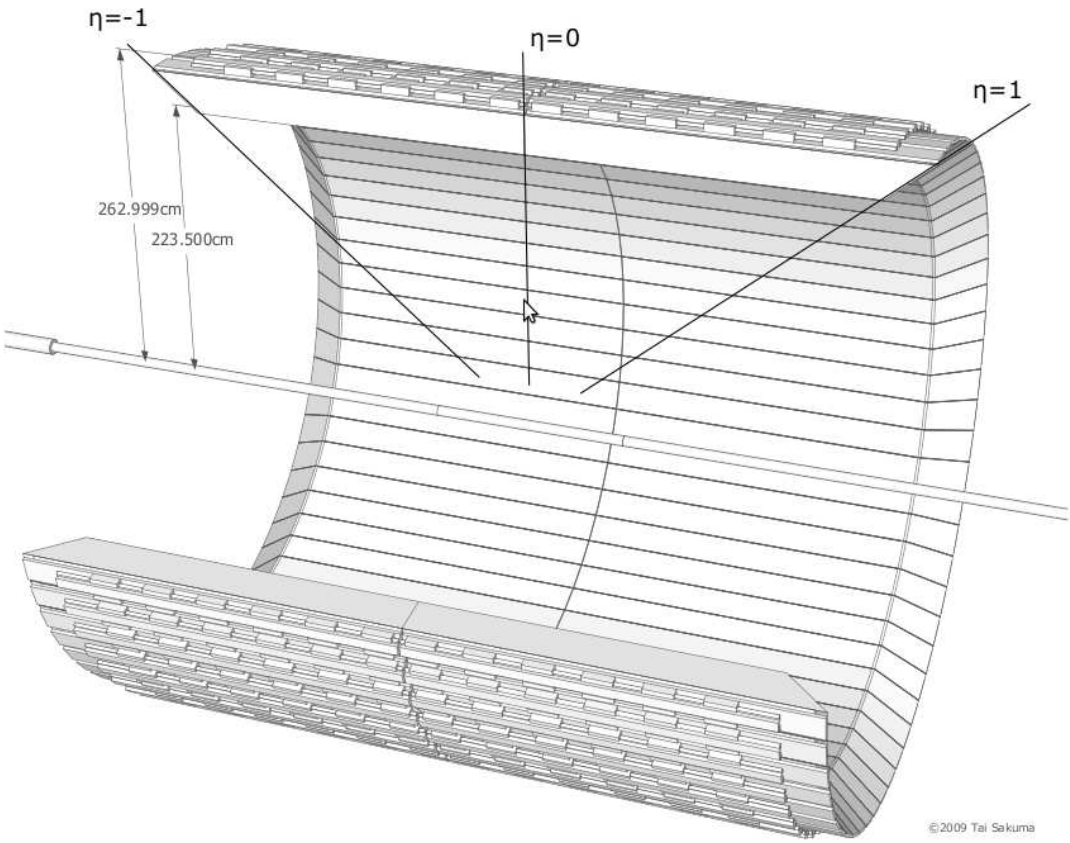

Figure 3.5: Diagram of the STAR Barrel Electromagnetic Calorimeter. Picture courtesy of Tai Sakuma.

The Upgraded Pseudo Vertex Position Detector (upVPD) [94] is a pair of detectors in pseudorapidities $4.24 < |\eta| < 5.1$. Each of them is composed of 19 tubes (lead converter, scintillator and photomultiplier) mounted around the beam pipe, as can be seen in Figure 3.2. Its main purpose is to measure the start time for the Time Of Flight system. To achieve its goal it has to have excellent timing resolution. The timing resolution of one tube is ≈ 140 ps. When multiple tubes are hit, the resolution scales as $1/\sqrt{(N)}$ where N is the number of hit tubes. Apart from measuring the start time for TOF, the upVPD can also serve to determine the collision vertex position *online*, which can then be used in the trigger. In 2007-2008 d+Au running, the average numbers were $\langle N_{east} \rangle = 10$ and $\langle N_{west} \rangle = 2$. This leads to the resolution of the collision vertex position of ≈ 3 cm, which is much better than what could be previously achieved with the BBC detector. In 2007-2008 d+Au running, the upVPD detector (coincidence with collision vertex position cut) was used in the minimum bias trigger together with signal in the east ZDC.

Chapter 4

Heavy Flavor Tracker

The heavy flavor quarks (c, b) are unique tool to probe the hot and dense matter created in heavy-ion collisions at RHIC [1]. Due to their large current masses (c: $\approx$ 1.3 GeV/c^2, b: $\approx$ 4 GeV/c^2 as shown in Table 1.1) they can not be thermally produced from the medium and also they stay heavy even in the case of chiral symmetry restoration. The measurement of heavy flavor hadrons can be used to test medium thermalization, mechanisms of energy loss and hadronization, as will be discussed in Section 4.1. These measurements can not however be done without a high precision micro vertex detector.

The Heavy Flavor Tracker (HFT), a proposed upgrade to the STAR experiment at midrapidity, was designed to reconstruct displaced decay vertices with high precision, enabling reconstruction of open charm hadrons down to very low p_{T} in the high-multiplicity environment of heavy-ion collisions. This will be achieved by using low mass MAPS sensors (PIXEL detector) together with fast strip detectors (IST,SSD), delivering high efficiency and ultimate pointing resolution at low p_{T} even in the high luminosity environment. The design of the detector is described in Section 4.2.

Numerous simulations have been carried out to fine tune and verify the design and to achieve approval for this project. The author of this thesis worked on some of these simulations as a part of his *service work* for the STAR Collaboration. On purpose, this work is not directly related to the main physics topic of this thesis. In particular, the focus of the service work project was on the simulations of D^0 and Λ_{C} reconstruction in Au+Au collisions which are reported in Section 4.3.

4.1 Physics of the HFT

The key measurement to probe the bulk effects in the heavy-ion collisions is the azimuthal anisotropy with respect to reaction plane ("elliptic flow" v_2). Good description of RHIC v_2 data with the ideal hydrodynamic simulation shows a very

efficient translation of the initial spacial anisotropy of the almond-shaped overlap region to the momentum anisotropy of the produced particles. Studies of v_2 for different particle species and particle spectra have identified the development of partonic collectivity in heavy-ion collisions at RHIC [1]. The assumption of the hydrodynamic models is an early thermalization of the produced medium, so it is important to *measure* if the medium is thermalized.

The key question then is whether or not charm quarks flow. If the elliptic flow of charm were comparable to the elliptic flow of the lighter quarks, this would be a clear indication of a thermalized state of matter because, in analogy to Brownian motion, it takes many interactions with lighter quarks and gluons, to cause a heavy quark to acquire the collective motion of the bulk matter. Measurement of of open charm hadrons to low transverse momentum (p_{T}) is of particular interest to address this question.

Currently most open heavy flavor analyses at RHIC use an indirect method by measuring their decay electrons. There is however an ambiguity in the fraction of these electrons coming from decays of c and b quarks. Also, especially at low p_{T}, the kinematics is not well constrained. Recent measurement by PHENIX Collaboration of v_2 of heavy flavor decay electrons is shown in Figure 4.1. It shows a non-zero value for $p_{\mathrm{T}} > 1$ GeV/c indicating flow of open heavy flavor hadrons. The flow of charm quark itself can however not be constrained by this measurement due to the aforementioned ambiguities.

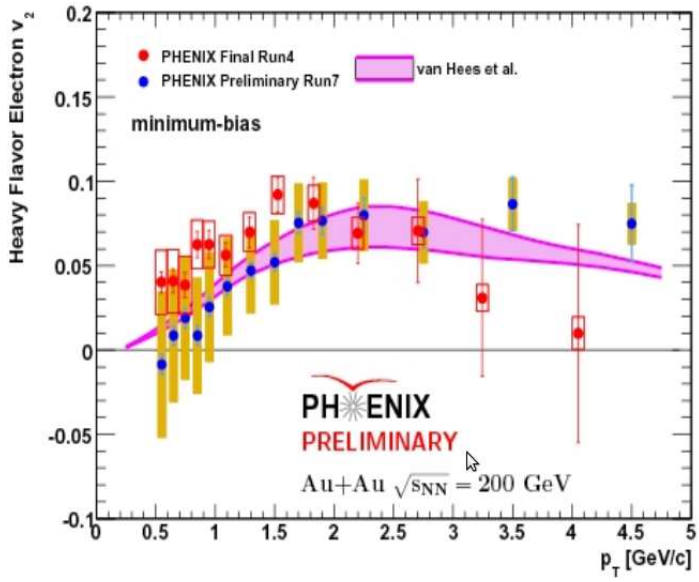

Figure 4.1: Elliptic flow of heavy flavor decay electrons measured by the PHENIX Collaboration [100]. A large value of v_2 at $p_{\mathrm{T}} > 4$ GeV/c (Preliminary Run7) may indicate a non-zero elliptic flow of b quarks.

Suppression of high p_{T} hadron production at RHIC [2, 4, 101] is commonly thought to arise from partonic energy loss in dense matter due to induced gluon radiation [102, 103]. Radiative energy loss of heavy quarks is expected to be suppressed due to the so called dead cone effect [104]. However, measurements of nuclear modification factor (R_{AA}) of heavy flavor decay electrons at high p_{T} [105, 106] indicate a significant energy loss of heavy quarks. As shown in Figure 4.2, the R_{AA} of heavy flavor decay electrons is consistent with charged hadrons (i.e., hadrons formed of *light* quarks) at high p_{T}. This is in contrary with the theoretical expectations, since the bottom quark decay contribution is not negligible in this p_{T} range and the dead cone effect should be visible.

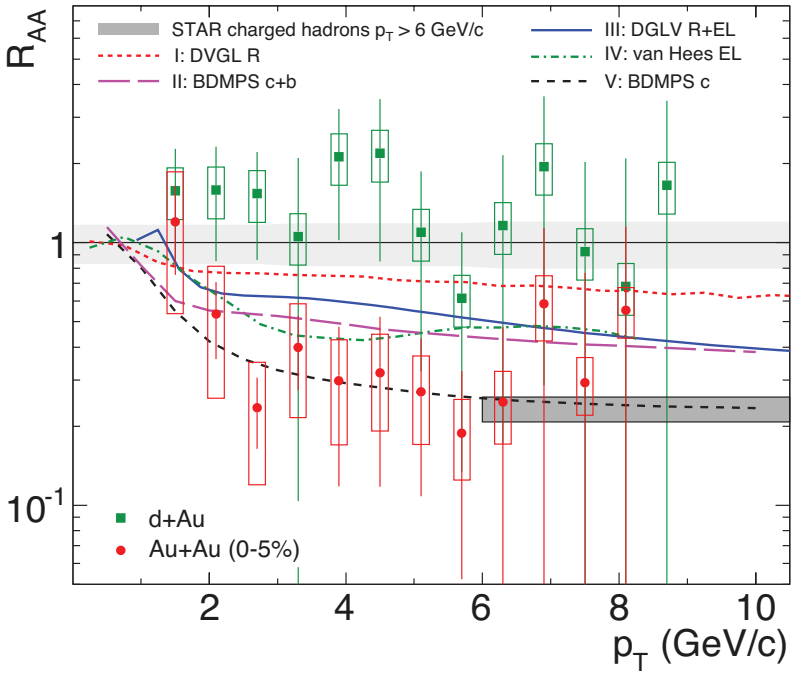

Figure 4.2: Nuclear modification factor R_{AA} of heavy flavor decay electrons [107]. The data in 0-10% Au+Au collision are well described by the model "V", which is however not realistic since it only considers electrons from charm decays, not from bottom decays.

Precise knowledge of the relative contributions of charm and bottom decays to electron spectra is crucial to interpret these results. Electron spectra from open charm hadron decays are also sensitive to relative Λ_{C}/D meson yield [108], due to different branching ratios of their inclusive electron decay channels.

In central Au+Au collisions at RHIC, a baryon/meson enhancement has been observed in the intermediate p_{T} region ($2 < p_{\mathrm{T}} < 6$ GeV/c) [109, 110, 111]. These results are usually explained by a hadronization mechanism involving collective multi-parton coalescence rather than independent vacuum fragmentation. The suc-

cess of the coalescence approach implies deconfinement and possibly thermalization of the light quarks prior to hadronization. A measurement of Λ/K^0_S ratio in p+p and Au+Au collisions is shown in Figure 4.3. A strong enhancement at intermediate p_T is observed in central Au+Au collision, in accordance with the expectations from coalescence hadronization models.

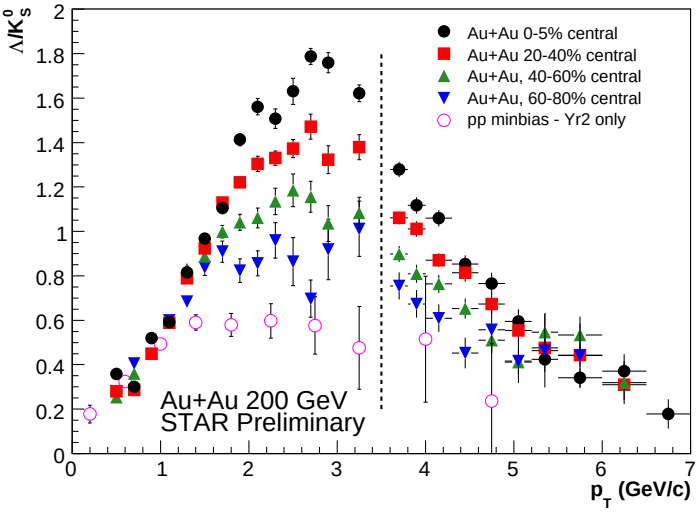

Figure 4.3: Measurement of Λ/K^0_S ratio in p+p and Au+Au collisions [112]. Strong enhancement in most central Au+Au collisions is observed in the $2 < p_T < 5$ GeV/c range.

Since Λ_C is the lightest charmed baryon and its mass is not far from that of the D^0 meson, a similar pattern of baryon/meson enhancement is expected in charm sector [113]. Λ_C/D^0 enhancement is also believed to be a signature of a strongly coupled quark-gluon plasma [114]. Therefore it is of interest to measure R_{CP} of Λ_C baryon and compare it to R_{CP} of D^0 mesons.

Direct reconstruction of open charm hadrons is necessary for these measurements. Given the large combinatorial backgrounds in heavy-ion collisions, topological reconstruction with a micro vertex detector is needed to achieve good signal significance.

4.2 HFT design

The HFT detector consists of three concentric subsystems: The PIXEL detector (2 layers), Intermediate Silicon Tracker (IST, 1 layer) and the existing Silicon Strip Detector (SSD) [115]. A sketch showing the individual components of the HFT detector is shown in Figure 4.4. While PIXEL and IST are completely new de-

tectors, the SSD was previously used in STAR and is currently having its readout upgraded. The HFT will not perform a stand-alone tracking, but will extend the tracks reconstructed by the TPC towards the interaction point. The parameters of the individual HFT subsystems are summarized in Table 4.1.

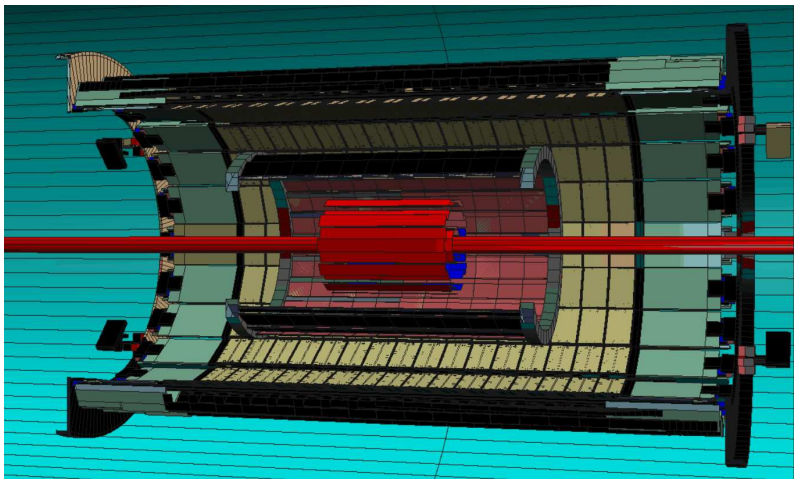

Figure 4.4: Heavy Flavor Tracker and its components (from outside in): Silicon Strip Detector (SSD, 1 layer), Intermediate Silicon Tracker (IST, 1 layer), PIXEL detector (2 layers).

layer	r (cm)	hit resol. $(r-\phi \times z)$ (μm $\times$ μm)
SSD	22	15 $\times$ 750
IST	14	115 $\times$ 2900
PIXEL2	8	9 $\times$ 9
PIXEL1	2.5	9 $\times$ 9

Table 4.1: Hit position resolutions of Heavy Flavor Tracker layers. Z direction is along the beam line, $r-\phi$ are the polar coordinates in the perpendicular plane. Values for the SSD taken from the beam test data [115], values for the IST and PIXEL are estimates.

The PIXEL detector is made of low-mass monolithic active pixel sensors (MAPS), fabricated by CMOS technology. Its scheme is shown in Figure 4.5: it does not use a voltage bias, so the depleted region is very thin and exists only around the n-well. The electrons created in the epitaxial layer thermally diffuse towards the low potential n-well region. The MAPS technology with 30 μm pixel pitch and a thickness of only 0.28% X_0 per layer enables high precision measurement close to the primary collision vertex. The PIXEL detector configuration is

shown in Figure 4.6. Inner layer sensors facing the beam pipe will improve STAR di-lepton capability by rejecting e^+e^- pairs from photon conversions (beam pipe thickness being only $\approx 0.15\%$ X_0).

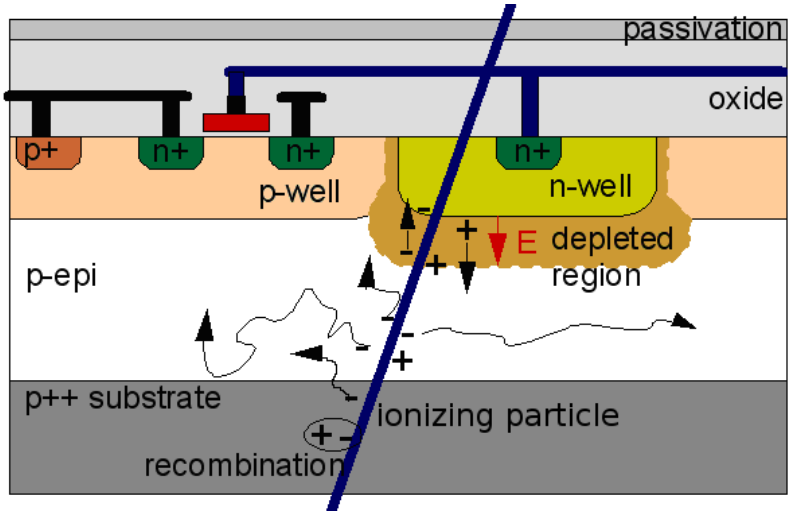

Figure 4.5: MAPS principle of operation: electrons created in the epitaxial layer thermally diffuse towards low potential n-well region. A small contribution to the total signal also exists from electrons created in the p++ substrate.

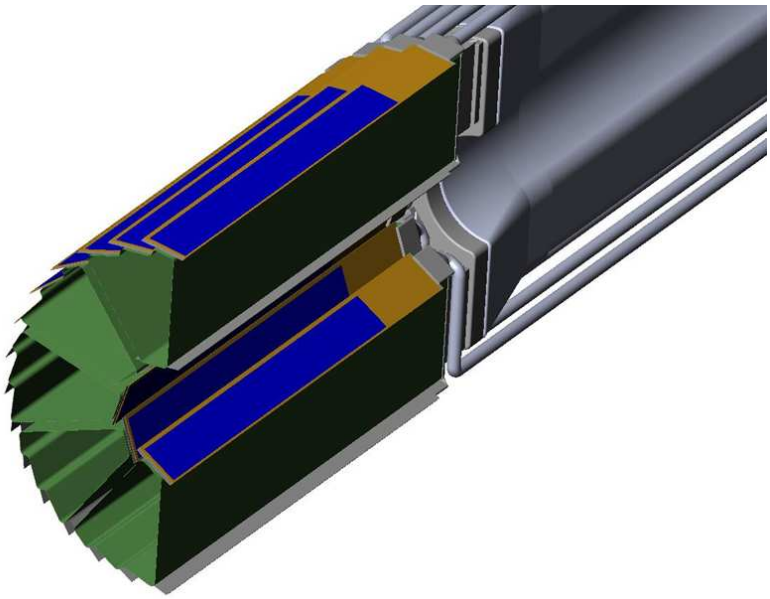

Figure 4.6: One half of the PIXEL detector with its support structure.

Since there is a very large number of pixels, the readout time of the PIXEL detector is relatively slow: ≈ 200 μs. Given the high Au+Au luminosity projected

for the RHIC-II [1] luminosity upgrade ($50 \cdot 10^{26}\mathrm{cm}^{-2}\mathrm{s}^{-1}$), the PIXEL detector will integrate over ≈ 10 minimum bias Au+Au collisions, creating pile-up hits.

The main role of the IST detector is to improve the pointing resolution to PIXEL2 layer, so that even low p_{T} tracks have negligible fake hit rate even in the presence of pile-up hits. The IST detector at radius of 14 cm is made of single-sided strip sensors. It is a fast detector, so there are no pile-up hits at IST detector layer.

The SSD detector is a double-sided silicon strip detector. The pitch of the strips is 95 μm and the angle between strips on both sides (stereo angle) is 35 mrad. The double-sided technology prevents from hit ambiguity even with long strips and so achieves a relatively good resolution along the strip direction. This resolution is 750 μm with the strip length of 42 mm. The SSD is a fast detector, so it does not accumulate pile-up hits.

4.3 Evaluation of HFT performance

To create realistic background for reconstruction of D^0 and Λ_{C}, HIJING [116] 200 GeV Au+Au events were generated with impact parameter $b = 0 - 3$ fm, corresponding to 0-10% most central collisions. To these simulated events, D^0 and Λ_{C} were added [2] and these hybrid events were filtered through GEANT and STAR detector response simulators. To assess the impact of pile-up, pseudo-random hits were added to PIXEL1 and PIXEL2 layers, corresponding to a minimum bias (MB) collision rate of 80 kHz and a primary vertex diamond size $\sigma_{PV\_Z} = 15$ cm. This is upper estimate of pile-up, in fact current RHIC-II projections show smaller luminosity (corresponding to MB collision rate ≈ 50 kHz) and bigger σ_{PV_Z}. Realistic simulation of electron transport in MAPS sensors is currently under development and the presented simulations use a simplified simulator instead (assuming resolutions given by pixel pitch and 90% hit finding efficiency).

The track impact parameter (pointing) resolution of the TPC+HFT tracking device is mainly delivered by the PIXEL detector (i.e., by the measurement of the two spacepoints closest to the primary collision vertex). This resolution is composed of these two terms:

$$\sigma_{\mathrm{pointing}} = \sqrt{\frac{\sigma_1^2 r_2^2 + \sigma_2^2 r_1^2}{(r_2 - r_1)^2}} \oplus \frac{r_1 \times \theta_{MCS}}{\sin(\theta)}, \tag{4.1}$$

where $\sigma_{1(2)}$ is the hit position resolution and $r_{1(2)}$ is the radius of the layers 1(2), θ is the particle angle with respect to the beam axis and θ_{MCS} is the angular standard deviation due to Multiple Coulomb Scattering (MCS) in the material of the 1st

[1] to be completed around the time of HFT detector installation to STAR experiment
[2] five to 30 D^0 or Λ_{C} per event were added

detector layer:

$$\theta_{MCS} = \frac{13.6 \text{ MeV}/c}{\beta p}\sqrt{\frac{X}{X_0}}, \tag{4.2}$$

where β and p are the particle velocity (fraction of speed of light c) and momentum and $\frac{X}{X_0}$ is the 1st detector layer thickness: $X \approx 0.43\% X_0$ inluding the beam pipe, which also contributes to the pointing resolution. Figure 4.7 includes results of the full simulation (points) compared to the lines from this simple calculation and shows they are in relatively good agreement.

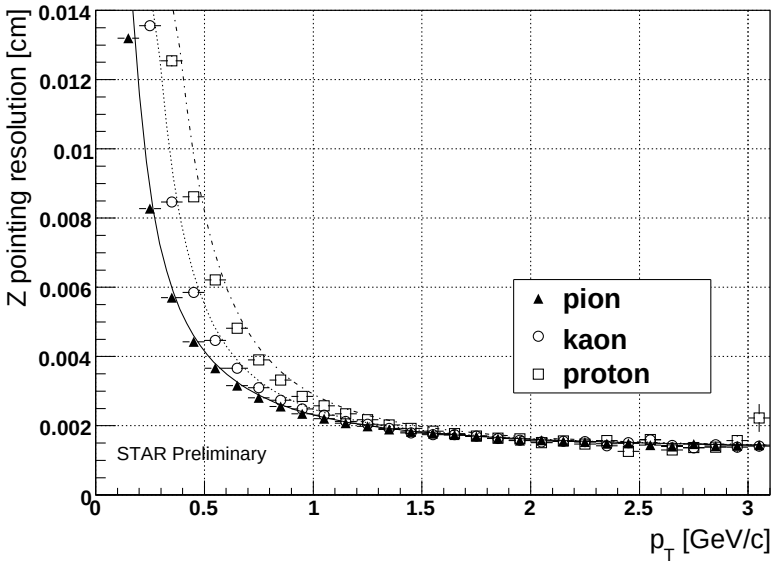

Figure 4.7: Track impact parameter resolution achieved with TPC+HFT tracking. Symbols: full detector simulation, lines: calculation for PIXEL detector only.

The decay modes used for reconstruction were $\mathrm{D}^0 \to \mathrm{K}^- + \pi^+$ (B.R. 3.8%) and $\Lambda_\mathrm{C} \to \mathrm{K}^- + \pi^+ + \mathrm{p}$ (B.R. 5.0%). For particle identification (PID) of daughter particles, the Time Of Flight detector [118] is used. This detector is an upgrade to STAR experiment and its full simulation was not available in the time of this study. Instead its performance parameters were estimated based on the design specifications. The $\mathrm{K} - \pi$ separation for $p_\mathrm{T} < 1.6$ GeV/c and $(\mathrm{K} + \pi) - \mathrm{p}$ separation for $p_\mathrm{T} < 3.0$ GeV/c is expected to be achievable with TOF. The estimated efficiency of TOF used in this study is 90%.

For Λ_C reconstruction, primary track combinatorial background is huge due to its very short decay length ($c\tau = 59.9$ μm) and three-body decay. To reduce this background, PID information of daughter tracks is required in some cases, limiting the acceptance. This cut is called GoodPID in the following. It is only used for $2 < p_\mathrm{T} < 4$ GeV/c. For Λ_C with higher p_T and for D^0 reconstruction, no PID

information is used once the daughter particle p_{T} exceeds the PID threshold of TOF. This PID strategy is marked RealPID. Other PID strategies will be tested in future. For example, most of the tracks seen in detector are charged pions, so requiring pion PID information may not be necessary.

Reconstruction efficiencies for D^0 and Λ_{C} without application of topological cuts are shown in Figure 4.8. The daughter tracks are required to be well reconstructed (at least 15 hits) in the TPC and have correctly associated hits in both PIXEL layers. Efficiency for Λ_{C} is smaller due to the fact that there are three daughter tracks with, on average, lower p_{T} than in the case of D^0. These efficiencies are the maximum achievable efficiencies and come solely from the requirement of reconstructing the daughter tracks of D^0 and Λ_{C}. After application of topological cuts for suppression of background they will decrease considerably.

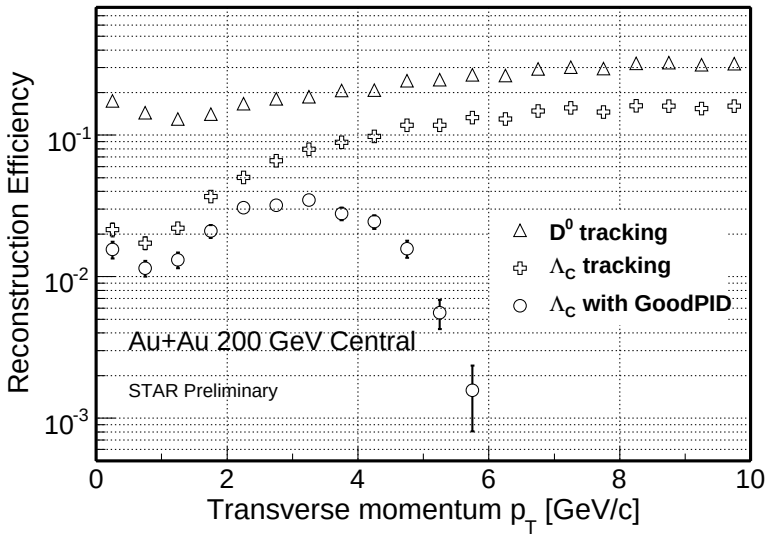

Figure 4.8: Efficiency of reconstructing daughter tracks of D^0 and Λ_{C} in $|\eta| < 1$. Note that no cuts to isolate signal from combinatorial background have been applied here. The efficiencies thus come solely from the requirement on reconstructing D^0 and Λ_{C} daughter tracks.

There is a large uncertainty in the total $c\bar{c}$ cross section at RHIC. The value measured by the STAR Collaboration [119] is higher than that measured by PHENIX experiment. Therefore, D^0 $dN/dy = 0.002$ per binary collision has been used for signal estimates, which is half of the value measured by STAR and roughly matches the value measured by PHENIX. The results hence show lower limit of the signal significance. $\Lambda_{\mathrm{C}}/\mathrm{D}^0$ ratio 0.2 was assumed for the case of no enhancement [113]. The shape of p_{T} spectra for D^0 and Λ_{C} in central Au+Au collisions was assumed to be a power-law:

$$\frac{1}{p_{\mathrm{T}}}\frac{dN}{dp_{\mathrm{T}}} = C \cdot (1 + \frac{p_{\mathrm{T}}}{p_0})^{-n} \tag{4.3}$$

$$p_0 = \langle p_{\mathrm{T}} \rangle \cdot \frac{n-3}{2}, \tag{4.4}$$

with mean transverse momentum $\langle p_{\mathrm{T}} \rangle = 1.0$ GeV/c, $n = 11$ and C being a normalization constant.

Given the hadronic decay channels of interest, there is no obvious fast [3] trigger available (such as BEMC tower with large E_{T} that is used to trigger for high p_{T} electrons or gammas). Therefore, the triggers considered for these simulations only include minimum-bias trigger and central (0-10% most central collisions) trigger. The peripheral collisions with centrality 60-80% will be extracted from the minimum bias data sample.

The signal (D^0, Λ_{C}) are rescaled between different centralities assuming their R_{CP} the same as charged hadrons measured by STAR [2]. The background tracks (K^-, π^+ and p coming from HIJING) are scaled assuming $\langle N_{part} \rangle$ scaling. This approach overestimates the backgrounds because in reality the scaling is somewhere between $\langle N_{bin} \rangle$ and $\langle N_{part} \rangle$ and $\langle N_{bin} \rangle$ has stronger centrality dependence. The respective values of $\langle N_{bin} \rangle$ and $\langle N_{part} \rangle$ used are shown in Table 4.2.

centrality	$\langle N_{bin} \rangle$	$\langle N_{part} \rangle$
0-10%	940	326
60-80%	21.2	20.9
min.bias	293	126

Table 4.2: Centrality parameters $\langle N_{bin} \rangle$ and $\langle N_{part} \rangle$ in 200 GeV Au+Au collisions used for rescaling signal and background in the simulations of D^0 and Λ_{C} reconstruction with the HFT. Minimum bias is taken as 0-80% centrality here. Systematic uncertainties on $\langle N_{bin} \rangle$, $\langle N_{part} \rangle$ of $\approx 10\%$ are not considered further. They would be a part of normalization uncertainty in the measurement of R_{CP}, but would cancel out in R_{CP} ratios. The details on the Glauber model calculation used to obtain these values can be found in Appendix A.

Data taking rate of about 500M events per month is expected with data acquisition at 500 Hz and beam up time 40%, which makes it possible to collect up to 2000M events in one RHIC run (6 months). This achievement is realistic in the light of STAR data taking experience from 2010 Au+Au running, when 800M events (with TPC readout) were taken in less than 3 months [120].

[3] i.e., not requiring readout of tracking detectors

4.3.1 Simulation results: D^0 reconstruction

For the simulation of D^0 reconstruction, 20000 HIJING events are used with added D^0 (10 per event with 100% branching ratio to $K^-\pi^+$ channel). The input p_T spectrum of D^0 was flat, so reweighting to realistic (power-law) spectrum had to be applied to calculate the yield in addition to accounting for artificially increased yield and branching ratio. The same setting was used for the sample with pile-up hits added to PIXEL detector layers, except only 10000 events were generated. The results were presented in [121].

To search for D^0 candidates, pairs of tracks compatible with K^- and π^+ PID assumptions with Distance of Closest Approach (DCA) to Primary Vertex (PV) $DCA_{PV} > 50$ μm were used. Further cuts used to get a clean sample of D^0 include:

- fitted decay vertex (V0) [4] within 50 μm of both track helices: $DCA_{V0} < 50$ μm
- pair invariant mass $1.83 < m_{inv} < 1.90$ GeV/c^2
- $\cos(\theta) > 0.98$, where θ is the angle between pair (D^0 candidate) momentum and the vector connecting Primary vertex to Decay vertex

The schematic drawing of D^0 decay with the cut variables is shown in Figure 4.9.

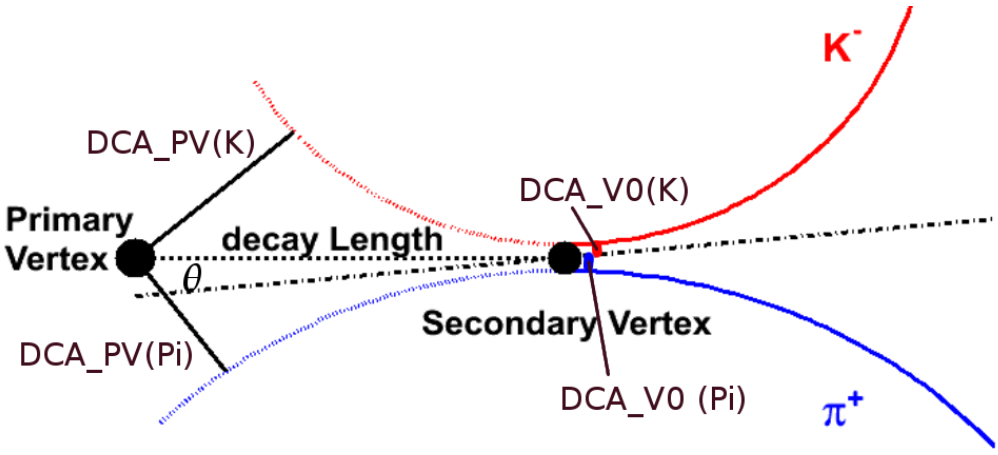

Figure 4.9: Schematic drawing of the decay $D^0 \rightarrow K^- + \pi^+$. The DCA variables used for cuts on daughter tracks: DCA_{V0}, DCA_{PV} are shown together with the angle θ used for a cut applied to the D^0 candidate: θ is the angle between the D^0 candidate momentum vector and vector from the primary vertex (PV) to the secondary vertex (V0).

[4] linear interpolation between the two points of closest approach of the two track helices is used to obtain the decay vertex candidate, simulations with Kalman filter [122] are currently under study

Signal significance ($\frac{S}{\sqrt{S+B}}$) of $D^0 + \overline{D^0}$ from 100×10^6 central Au+Au collisions is shown in Figure 4.10. It is possible to reconstruct D^0 in the broad transverse momentum range $0.5 < p_T < 10$ GeV/c with signal significance greater than 10σ. The effect of pile-up in the PIXEL detector is significant, but even with it the expected performance is still very good. A fine tuning of cuts will be needed in the region $p_T < 0.5$ GeV/c, where the current cuts do not suppress the background enough. The good significance of D^0 signal will enable the measurement of D^0 azimuthal anisotropy v_2 and p_T spectra to construct the nuclear modification factor R_{CP}.

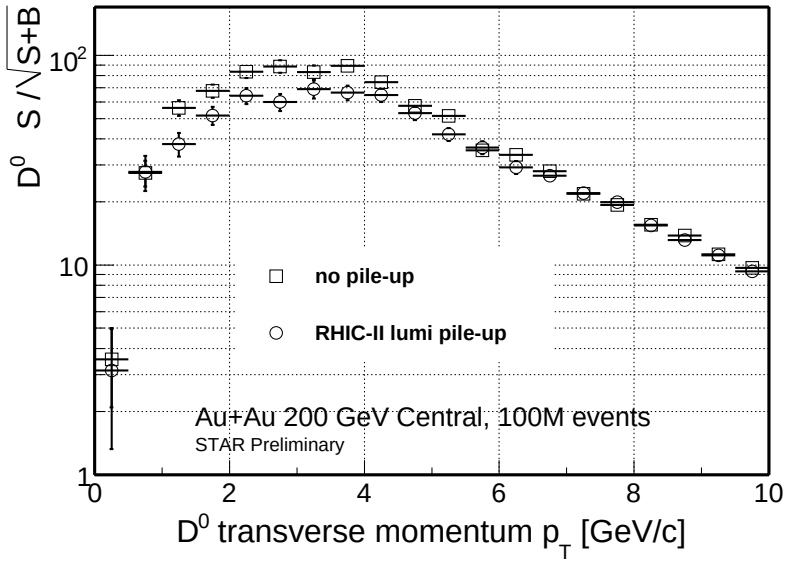

Figure 4.10: D^0 signal significance in central Au+Au events. The track reconstruction was performed with and without pile-up in the PIXEL detector. The additional pile-up hits in the PIXEL detector are occasionally picked by the tracker instead of the correct hits, which results in degradation of track pointing resolution. The probability of this wrong hit association is higher at low p_T, where the track pointing resolution is worse than at high p_T, causing ambiguities in hit association to the track.

Estimated statistical errors on v_2 measurement of D^0 meson are shown in Figure 4.11. In this picture the v_2 is expected to be carried by the constituent quarks of D^0 meson prior to hadronization and so translated into v_2 of the meson. This assumption is consistent with the so called constituent quark scaling of v_2 observed for light flavor hadrons at RHIC [123]. For $p_T > 1.0$ GeV/c, the HFT will be able to distinguish between extreme elliptic flow scenarios: zero elliptic flow of the charm quark and elliptic flow equal to that of light quarks.

The data sample for R_{CP} measurement (500×10^6 minimum bias events) includes 62.5×10^6 central and 125×10^6 peripheral events. The estimated statistical errors

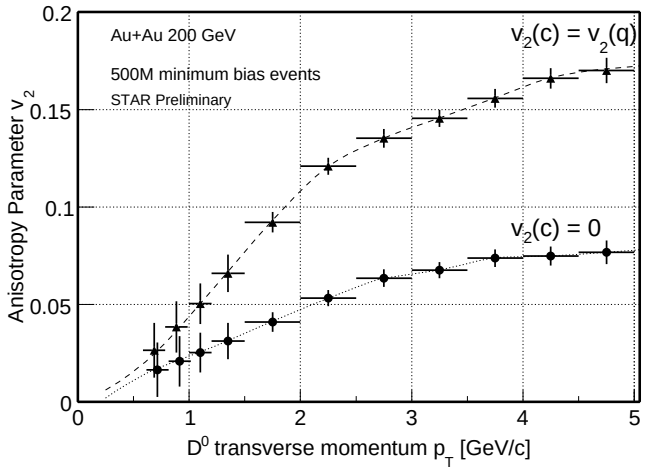

Figure 4.11: The estimated statistical errors of v_2 (elliptic flow) measurement of D^0 meson ($D^0 + \overline{D^0}$, $|\eta| < 1.0$), with the v_2 values for two scenarios of charm quark elliptic flow: zero or equal to the elliptic flow of light quarks.

on D^0 R_{CP} measurement are shown in Figure 4.12. At highest p_T, the relative error is 20%, which is a good precision for this region. The assumed p_T dependence of R_{CP} in Figure 4.12 is taken from the measurement of charged hadrons. At low p_T it is close to N_{part} scaling, the "bulk" particle production. At high p_T it shows a strong energy loss, since the binary collisions scaling would lead to $R_{CP} = 1$. The charm quarks are expected to be suppressed less than light quarks for $p_T < 4$ GeV/c, where the dead cone effect is expected to play an important role.

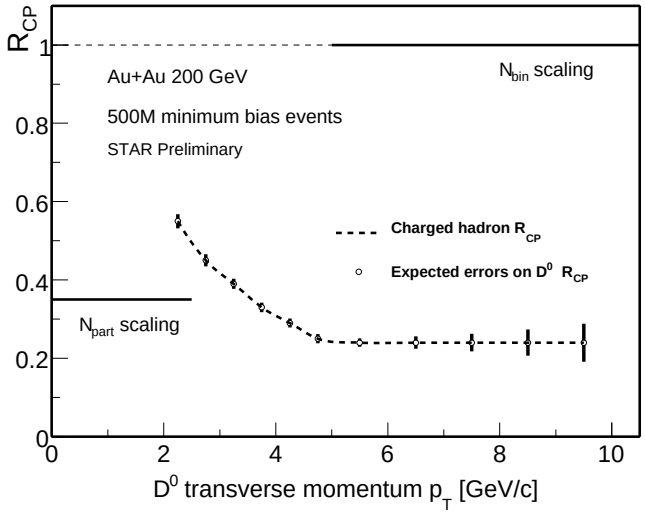

Figure 4.12: Estimated statistical errors for R_{CP} measurement of D^0 meson, in 500×10^6 minimum bias Au+Au events. The points with the estimated errors are superimposed on a curve of measured R_{CP} of charged hadrons.

4.3.2 Simulation results: Λ_C reconstruction

The simulated data sample for Λ_C reconstruction was 19.5k central HIJING events. Half of it had 5 Λ_C added per event, the other half had 30 Λ_C added per event, all with 100% branching ratio to $K^- + \pi^+ + p$ and flat p_T distribution. The pile-up in PIXEL detector at level of RHIC-II luminosity was simulated. The yield of Λ_C in central collisions was estimated to be either 20% of D^0 yield at all p_T or the enhancement of Λ_C/D^0 ratio was considered of the same magnitude as the Λ/K^0_S enhancement observed in 200 GeV Au+Au colisions by STAR [111]. The yield of Λ_C in peripheral (60-80%) collisions was taken to be 20% of D^0 yield at the same p_T. The results presented here are based on [124] with improvement in topological cut optimization.

The same set of cut variables was used to select the Λ_C candidates as the one used for D^0, except the cut DCA_{V0} was rescaled by track pointing resolution [5]. The invariant mass cut was fixed at $2.27 < M_{inv} < 2.31$ GeV/c^2. The other three cuts were automatically tuned (3-dimensional scanning of the parameter space) to achieve the highest signal significance. This was performed separately for 3 p_T bins ($2-3, 3-4, 4-5$ GeV/c), three different signal and background assumptions (central collisions, central collisions with enhancement, peripheral collisions) and two different PID options (optional requirement of all three tracks being below TOF PID separation thresholds: GoodPID, or allowing for contamination by other particle species: RealPID).

For the measurements of Λ_C/D^0 enhancement, statistics of 2×10^9 minimum bias and 250×10^6 central triggered events was assumed, giving 500×10^6 central and 500×10^6 peripheral events used for R_{CP}. The maximum signal significances reached are shown in Table 4.3. The need for RealPID in the highest p_T bin is given by the fact that background is not so severe there and the signal acceptance drops fast (as shown in Figure 4.8).

	$2 < p_T < 3$ GeV/c		$3 < p_T < 4$ GeV/c		$4 < p_T < 5$ GeV/c	
centrality	best $\frac{S}{\sqrt{S+B}}$	PID	best $\frac{S}{\sqrt{S+B}}$	PID	best $\frac{S}{\sqrt{S+B}}$	PID
central	2.7	Good	4.6	Good	5.5	Real
central enhanced	6.6	Good	11.6	Good	10.1	Real
peripheral	4.3	Good	6.6	Good	8.3	Real

Table 4.3: Maximum signal significances reached for Λ_C reconstruction for 500M events. "PID" marks whether GoodPID or RealPID option was used to reach the quoted signal significance.

[5] so the cut applied was $DCA_{V0}/\sigma < cut$ where σ is the pointing resolution which is p_T and particle species dependent as shown in Figure 4.7

Statistical errors on $R_{\mathrm{CP}}(\Lambda_{\mathrm{C}})/R_{\mathrm{CP}}(\mathrm{D}^0)$ are shown in Figure 4.13. This result shows that the measurement can distinguish between the case of Λ/K^0_S-like enhancement and the ratio flat in p_{T}. The latter would mean that the hadronization of Λ_{C} is not influenced by the medium created in central Au+Au collisions. This information is crucial to determine if the model of hadronization via the collective multi-parton coalescence at intermediate p_{T} can be applied to charm sector.

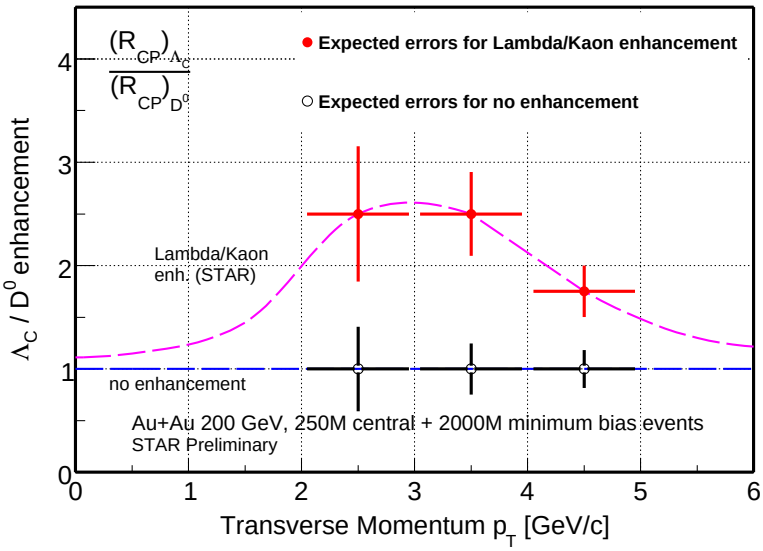

Figure 4.13: Expected statistical errors on $\Lambda_{\mathrm{C}}/\mathrm{D}^0$ measurement, assuming 500×10^6 central and 500×10^6 peripheral collisions. The lines show two possible scenarios of $\Lambda_{\mathrm{C}}/\mathrm{D}^0$ R_{CP} ratios: one is a ratio flat in p_{T} while the other one expects enhancement of $\Lambda_{\mathrm{C}}/\mathrm{D}^0$ ratio same as the Λ/K^0_S enhancement [111].

4.4 Summary

The simulation described in this Chapter started in 2007 with the study of $\mathrm{D}^0 \rightarrow \mathrm{K}^-\pi^+$ decay. The physics addressed by these studies were charm collectivity and energy loss. The results were included in the proposal of the HFT project [117] that was submitted to the main funding agency [6] for *CD0* [7] review. The author of this thesis participated in this review that took place at BNL on February 25-26, 2008. The results of D^0 reconstruction were presented in a poster at Quark Matter 2008 conference [121].

The studies of Λ_{C} reconstruction with emphasis on measurement of $\Lambda_{\mathrm{C}}/\mathrm{D}^0$ ratio started in 2008 and were presented in two conferences [124, 126]. After the detector

[6] U.S.Department of Energy (DOE) Office of Science

[7] CD: "Critical Decision". CD0 review approves the physics need for the project. More on the procedures of project reviews by the U.S. DOE can be found in [125]

design was changed (number of new strip layers changed from 2 to 1), new simulations were carried out in 2009 that were included in the Conceptual Design Report document [127], submitted for the *CD1*, that took place at BNL on November 12-13, 2009. In 2010 the project received positive CD1 approval and is moving towards installation of small acceptance prototype of PIXEL in 2012, to be followed by the full detector in 2013 (ready for 2014 RHIC run).

Heavy Flavor Tracker is the crucial upgrade of the STAR experiment. Its performance with the proposed design was evaluated by extensive simulations, of which the Λ_C and D^0 reconstruction was presented. The measurement of open charm hadrons over a broad p_T range will enable precision study of charm collectivity, energy loss and baryon/meson ratios. These are important ingredients for a systematic study of the dense medium created in heavy-ion collisions at RHIC.

Chapter 5

Jet analysis in p+p and d+Au

Full jet reconstruction in heavy-ion collisions brought new insights in the mechanism of jet energy loss and in comparison to theoretical models improves the understanding of the medium created in Au+Au collisions at RHIC. The importance of d+Au reference measurement of inclusive hadron p_{T} spectra and di-hadron correlation measurements [4] to interpret the observations from heavy-ion collisions was discussed in Section 2.5.

Study of jet production and properties in d+Au in combination with similar studies in p+p can therefore be considered an essential baseline to the jet measurements in heavy-ion collisions. The study of jet production in d+Au collisions in comparison to p+p and as a function of collision centrality can also be used to measure the effects of cold nuclear matter.

This analysis uses $\sqrt{s_{\mathrm{NN}}} = 200$ GeV data from the RHIC 2007-2008 run (RHIC *run 8* [1]). The following sections describe the d+Au data and the jet reconstruction methodology common to p+p and d+Au. The specifics of p+p data from run 8 will be described separately in Chapter 7. The results of the inclusive jet analysis are presented in Chapter 6 and the di-jet analysis is the subject of Chapter 7.

5.1 Run 8 d+Au data

The amount of minimum bias d+Au collisions recorded by the STAR experiment in RHIC run 8 more than doubled the available statistics from the previous d+Au run (2003). What is even more important is the fact that this was the first d+Au run when the full BEMC calorimeter was installed (the acceptance was only half in 2003).

The *minimum bias* trigger is set up in a way to be the least sensitive to the collision details: it should trigger on all inelastic events. The STAR implementation

[1] the d+Au collisions data were taken from December 6th, 2007 till January 27th, 2008 and the p+p data were taken between February 12 and March 10, 2008

in run 8 used in this analysis is the "VPD-ZDCE" trigger, that combines the signal from the east ZDC detector with a coincidence of the VPD detectors. The signal in the east ZDC (detecting spectator neutrons from the Au nucleus) has to be above threshold. The VPD coincidence uses a timing cut to select only events with primary collision vertex [2] close to the center of the detector in the z direction (along the beam axis). However, due to the small acceptance of VPD and small multiplicity of particles produced in the peripheral d+Au collisions, this trigger has efficiency that depends on centrality. This has to be corrected for and will be described in more detail in Section 5.2. In addition, even east ZDC alone has finite efficiency: $95 \pm 3\%$ [4].

In run 8, the total of 48 million events with VPD-ZDCE trigger were collected. Several further event selections were performed to select the data useful for jet analysis:

- only events with TPC, BEMC and FTPC in the readout
- only events with reconstructed primary vertex less than 30 cm from the detector center along the z axis: $|VertexZ| < 30$ cm.
- only events with high quality primary vertex

The quality of primary vertex is determined by its *ranking*, a quantity based on number of TPC tracks used in the vertex finding matched to BEMC and number of TPC tracks crossing the central membrane [128]. Both these criteria are used to minimize the contamination by pile-up vertices, since tracks from up to 12 pile-up collision are present in one TPC readout frame in addition to the triggered collision in run 8 d+Au data. The *ranking* has to be greater than -2.5 to accept the event. In addition, at least one TPC track used for vertex finding that is matched to a tower in the BEMC is required. The efficiency of these event cuts and the respective numbers of events are summarized in Table 5.1. After application of the event cuts about 60% of the total recorded statistics are used for the jet analysis.

5.2 Centrality selection

The multiplicity $mult_{FTPCE}$ of high quality tracks reconstructed in the East FTPC ($-3.8 < \eta < 2.8$) [3] was used as centrality measure for d+Au collisions in run 8. Due to varying performance of the FTPC during the data taking (causing azimuthal acceptance changes, thus different track multiplicity for given centrality), the data

[2] referred to as *primary vertex* in the following

[3] track selection criteria: track fitted successfully to event primary vertex within distance of closest approach $DCA < 2$ cm, not marked as pile-up track, track transverse momentum $p_{\mathrm{T}} < 3$ GeV/c, number of FTPC fit points: 6 to 11

event label	number of events (M)	% of all events
all taken	48.0	100
with detectors	44.2	92
available	40.0	83
$\|VertexZ\| < 30$ cm	30.5	64
primary vertex quality	29.4	61

Table 5.1: Data (million of events) available after the various event selection criteria are subsequently applied. "Available" means that the raw data were reconstructed off-line and can be used for physics analysis.

were divided into three run periods in which the FTPC acceptance remained unchanged. P1: from the start of the run till January 8th 2008, P2: from January 9th till January 20th 2008, P3: from January 21st 2008 till the end of the run. The distributions of $mult_{FTPCE}$ for the three run periods are shown in Figure 5.1. It can be clearly seen that in the P3 period the acceptance of East FTPC was much smaller than in the other two. On the other hand, dependence on $VertexZ$ is not very strong (as illustrated for P1) and will not require $VertexZ$ - dependent centrality cuts.

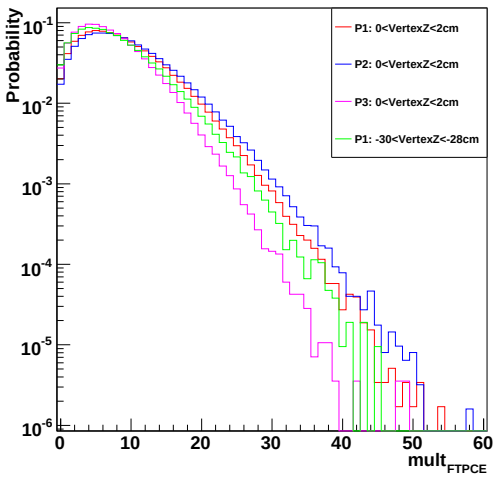

Figure 5.1: Run period and $VertexZ$ dependence of East FTPC multiplicity.

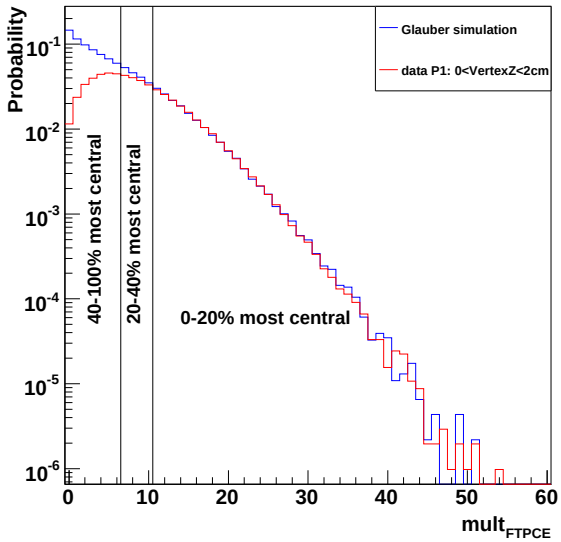

Figure 5.2: Comparison of East FTPC multiplicity distributions between data from run period P1 and Glauber simulation.

A Glauber Monte Carlo simulation was used to connect the initial nuclear geometry to the track multiplicity in $-3.8 < \eta < -2.8$. Woods-Saxon density profile with radius $R = 6.5$ fm and skin depth $c = 0.535$ fm was used for the Au nucleus and the Hulthen form [129] of the wave function was used to describe the deuteron. Generating impact parameter b probability distribution $dN/db \propto b$ and initial nu-

cleon positions according to the aforementioned density profiles of the Au and d nuclei, the nucleon-nucleon collisions occur for nucleons with transverse distance:

$$d < \sqrt{\frac{\sigma_{inel}}{\pi}}, \tag{5.1}$$

where $\sigma_{inel} = 42$ mb is the inelastic nucleon-nucleon cross section at $\sqrt{s} = 200$ GeV. This way the number of participants N_{part} and the number of binary collisions N_{bin} are determined for a given simulated collision. More details on the Glauber model implementation used to define centrality in STAR can be found in [130] and in Appendix A.

Multiplicity distributions in p+p collisions were measured by the UA5 experiment [131] and they are well described by the Negative Binomial Distribution (NBD). The probability of a collision with multiplicity n is:

$$P_{\mu,k}(n) = \frac{\Gamma(n+k)}{\Gamma(n+1)\Gamma(k)} \cdot \frac{(\mu/k)^n}{(\mu/k+1)^{n+k}}, \tag{5.2}$$

where parameter μ is the mean multiplicity and parameter k controls the shape of the distribution (for $k \to \infty$ the distribution becomes Poisson). Assuming $\langle N_{part} \rangle$ scaling of produced particle multiplicity, for given μ and k parameters the NBD distribution is sampled N_{part} times to obtain the multiplicity distribution for a collision with given N_{part}. The resulting multiplicity distribution can then be fit to the real data to obtain the values of NBD parameters μ, k. An additional free parameter is introduced to better describe the real data in the three run periods in the presented analysis: tracking efficiency.

The fit was performed for one run period and the same μ, k were used to fit the tracking efficiency for the other two run periods. Given lower efficiency of the trigger for low multiplicity events $mult_{FTPCE} < 10$ this range is excluded from the fits. The final parameters for the three run periods are shown in Table 5.2. The quantiles of the distribution of $mult_{FTPCE}$ in the Glauber simulation are determined to define the centrality: 0-20% (central), 20-40% (semi-peripheral), 40-100% (peripheral). Figure 5.2 shows the distributions of $mult_{FTPCE}$ for data (P1) and Glauber simulation, normalized in the high-multiplicity region $mult_{FTPCE} > 20$. A deficit of low multiplicity events in the data is clearly seen. This is attributed mainly to trigger efficiency.

A detailed study of the multiplicity of tracks in the TPC [4] revealed deficit at low multiplicity (caused partially by trigger and partially by inefficiency of primary vertex finding). Therefore to correct for the inefficiencies at low multiplicities (East

[4] track selection criteria: track pseudorapidity $|\eta| < 0.5$, track fitted successfully to event primary vertex within distance of closest approach $DCA < 3$ cm, not marked as pile-up track, number of TPC fit points greater than 9, quality of fit through primary vertex $chi2_{PV} < 6$ - details to be found in Section 5.3

	Run period P1	Run period P2	Run period P3
fit parameters			
NBD μ	1.18	1.18	1.18
NBD k	0.76	0.76	0.76
tracking efficiency	79%	83%	61%
$mult_{FTPCE} = M$ cuts			
0-20%	$M > 10$	$M > 10$	$M > 8$
20-40%	$6 < M \leq 10$	$6 < M \leq 10$	$4 < M \leq 8$
40-100%	$0 \leq M \leq 6$	$0 \leq M \leq 6$	$0 \leq M \leq 4$

Table 5.2: Centrality selections via the multiplicity of tracks in the East FTPC for the three run periods in run 8 d+Au running [132].

FTPC, TPC), 2-dimensional reweighting based on distributions of $mult_{FTPCE}$ and $mult_{TPC}$ in data and Glauber simulation was performed. An example of this distribution in data is shown in Figure 5.3. Given the previously observed dependences on run period and $VertexZ$ value, this reweighting was done separately for each of the three run periods and in 30 $VertexZ$ bins, 2 cm wide. An example of the weight for one particular bin is shown in Figure 5.4. These weights were applied to all measurements done in an event with given value of $mult_{TPC}$ and $mult_{FTPCE}$. The summary of the centrality definition is depicted in Table 5.3. It is clearly seen that after reweighting the event numbers in centrality bins correspond well to the centrality quantiles (20:20:60).

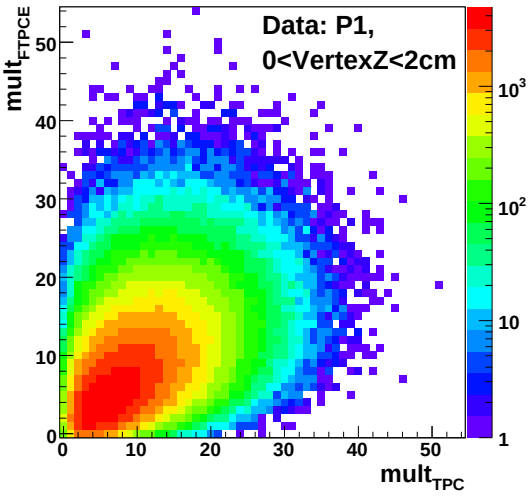

Figure 5.3: Distribution of $mult_{TPC}$ and $mult_{FTPCE}$ in data for run period P1 and one particular bin in $VertexZ$.

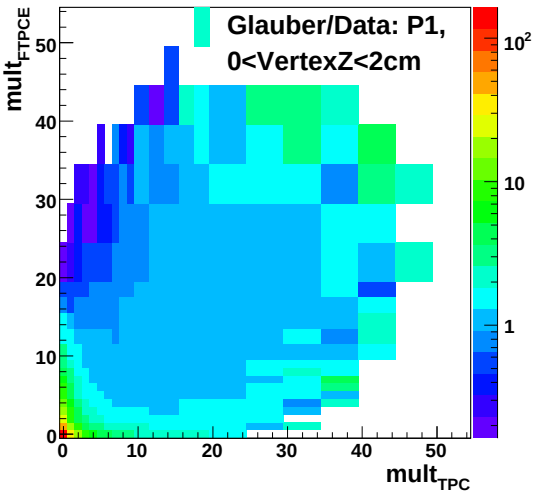

Figure 5.4: 2-dimensional weight based on $mult_{TPC}$, $mult_{FTPCE}$ shown for run period P1 and one bin in $VertexZ$. The weight is normalized to unity in the region $mult_{TPC} \geq 10, mult_{FTPCE} \geq 10$.

	0-20%	20-40%	40-100%
raw events	8.9	8.1	11.6
reweighted events	8.4	8.2	28.2
$\langle N_{bin} \rangle$	14.6 ± 1.3	10.8 ± 1.0	4.8 ± 0.4
$\langle N_{part} \rangle$	15.2	11.4	5.6
$\langle b \rangle$	3.6 fm	4.6 fm	6.7 fm

Table 5.3: Glauber model related values $\langle N_{bin} \rangle, \langle N_{part} \rangle$, mean impact parameter $\langle b \rangle$ and numbers of events (in million) before and after reweighting for the three centrality bins in run 8 d+Au running. The errors on $\langle N_{bin} \rangle$ are systematic and are discussed in the main text in detail. The systematic errors of $\langle N_{part} \rangle$ have not been determined but are not needed for the analysis in this thesis. The statistical errors of $\langle N_{bin} \rangle$ are negligible in comparison to the systematic ones.

The systematic uncertainties on centrality definition (in particular interest here is the impact on $\langle N_{bin} \rangle$) were determined by varying Woods-Saxon profile parameters and σ_{inel} within their uncertainties. Additional "experimental" contribution to the systematic uncertainty comes from from variation of $mult_{FTPCE}$ cuts and from the level of agreement of reweighted multiplicities to those in the Glauber simulation. The total systematic uncertainty on $\langle N_{bin} \rangle$ is $\approx 9\%$. Each of the uncertainties of σ_{inel} and the "experimental" uncertainties contribute roughly half of the total, the other sources of uncertainties are negligible. In the following the systematic uncertainty on $\langle N_{bin} \rangle$ is therefore composed of two parts of the same magnitude $6.4\% = 9\%/\sqrt{2}$. The part coming from σ_{inel} is taken totally correlated between different centralities, the part related to experimental aspects of centrality selection is taken uncorrelated between different centralities.

5.3 Selection of tracks from the Time Projection Chamber

The tracks reconstructed in the Time Projection Chamber (TPC) are used to obtain the charged component of jets. The TPC tracking algorithm starts with the reconstructed hits and going from large radius to the smaller radius it forms track segments and tracks. Kalman filter [122] is used to account for ionization energy losses while traversing material. This way *global* tracks are formed, having up to 45 fit points (minimum number of fit points is 10). Global tracks passing close to the beam axis are used to fit the z position of the primary vertex, while its x, y position is taken from the beam line parametrization. Global tracks with distance of closest approach $DCA < 3$ cm to the primary vertex are marked *primary* and their momentum is refit using the primary vertex as a high precision space point. Tracks

which failed this refit have a negative value assigned to its *flag* and are discarded.

Primary tracks with $|\eta| < 1.0$ are used for jet analysis. As the jet measurement is very sensitive to the quality of high p_{T} tracks, further cuts have are applied:

- discard post crossing tracks [5]: $flag < 1000$.
- Distance of closest approach to primary vertex: $DCA < 1$ cm.
- Number of TPC fit points: $fitpts > 20$.
- Protection against split tracks: $fitpts/possible > 0.52$, where *possible* is the maximum number of fit points in the TPC given by the track geometry.
- Good fit to primary vertex: $chi2_{PV} < 6$ [6]

To check that the centrality defined in the previous section and these tracks produce results consistent with previous measurements [4, 133], a comparison of inclusive charged hadron R_{CP} (see Eq. 2.10) was made. Track p_{T} spectra were measured for the three centrality bins and their $\langle N_{bin} \rangle$ weighted ratio R_{CP} was constructed. No corrections to the p_{T} spectra are made, but centrality dependent effects are at maximum 1% level and other effects cancel out in the ratio. The result in Figure 5.5 shows that R_{CP} with centrality definition and the track cuts described above is consistent with the STAR measurements from run 2003 [4, 133].

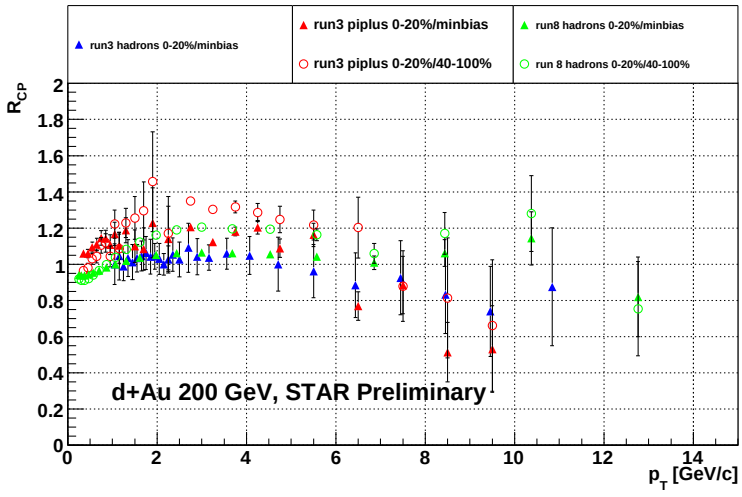

Figure 5.5: Comparison of inclusive charged hadron R_{CP} to previously published STAR data: run 2003 charged hadrons [4] and run 2003 π^+ [133].

[5] tracks with drift path longer than half of the TPC, meaning they came from a pile-up event which happened *after* the triggered event

[6] $chi2_{PV}$ is the χ^2 of the primary vertex point in the primary track refit

5.4 Reconstruction of jet neutral energy using the BEMC

When a particle such as photon or electron hits the BEMC detector near the center of one of its towers, it leaves most of its energy in that tower. The signal deposited in the BEMC tower is digitized via a 12-bit ADC. The voltages in photomultiplier tubes are set with an η dependence, so that ADC is proportional to the transverse energy, E_{T}, with a maximum of about 60 GeV ($\approx$ 70 ADC units corresponds to 1 GeV of E_{T} and the maximum ADC is 4095).

Detector noise, *pedestal*, is calculated for each tower from time-averaged data and is subtracted off the measured ADC value. The average pedestal is about 30 and its RMS around 1 ADC. To protect from statistical fluctuation of detector background and from channels with wrong pedestal determination, the towers used for further analysis have to satisfy the following cuts: $pedestal > 0.1$, $(ADC - pedestal) > 4$ and $(ADC - pedestal) > 3 * RMS_{pedestal}$. Before the output of BEMC is useful for analysis, the signal has to be calibrated.

The relative calibration of the BEMC towers in one η ring is done via their MIP response [134]. The absolute calibration for the 40 η rings ($\Delta\eta = 0.05$) is done using the electron tracks reconstructed in the TPC [135]. The calibration of the outermost η rings turned out to be problematic, therefore only the towers in the $|\eta| < 0.95$ region are used. Of the remaining 4560 towers, 341 had problems with hardware, calibration or pedestal and are not used in the analysis either. Examination of the remaining towers (hit energy, hit frequency) revealed another 68 "hot" towers which were also excluded. The resulting BEMC acceptance is 91% in $|\eta| < 0.95$.

The BEMC was designed to measure electromagnetic showers coming from incident electron and photons, but different particle species also leave signal in the BEMC towers. A charged particle leaves in the calorimeter a MIP signal with energy:

$$E_{MIP} = \frac{1 + 0.056\eta^2}{\sin(\theta)} 0.261 \text{ GeV}, \tag{5.3}$$

where η is tower pseudorapidity and θ is its angle relative to the beam axis. But since the BEMC is about 1 nuclear interaction length thick, there is a non-negligible probability of hadronic showering by both charged and neutral incident hadrons (most probable for anti-nucleons).

Charged particle often deposits energy in the BEMC, resulting in energy double counting when TPC tracks and BEMC towers are combined in jet reconstruction. Previously the so called MIP subtraction (subtracting MIP energy deposit from the tower for each charged track pointing to it) was used in STAR jet analyses, but it suffered from large upward energy fluctuations in case of electron/hadronic

showers. Recently a new method subtracting 100% of incident track momentum from the tower energy deposit was introduced in STAR, which does not have these large fluctuations and results in better jet energy resolution [136]. This method is referred to as *100% hadronic correction* because it is mainly targeted at hadronic showers, and it is used in the present analysis of jets in d+Au. If tower energy reaches zero via this subtraction, it stays at zero (energy used in jet finder can not be negative).

5.5 Jet finder settings

In this analysis, k_T and $anti-k_T$ algorithms from the FastJet package [40] with resolution parameter $R = 0.4$ are used. Even though this value of R parameter does not capture 100% of the jet, it is a good choice since a smaller R parameter brings less underlying event background. Moreover $R = 0.4$ is the default choice for jet analyses in Au+Au collisions in STAR, as opposed to $R = 0.7$ which is often used for jet analyses in p+p collisions. The fraction of jet energy captured for different values of R is illustrated in Figure 5.6. It can be seen that for $R = 0.4$ the jet finder captures nearly 80% of energy of a 20 GeV jet. For higher jet energies this fraction is even more since the jets get more and more collimated. It should be noted that the jet observables are not corrected back to the original parton energy.

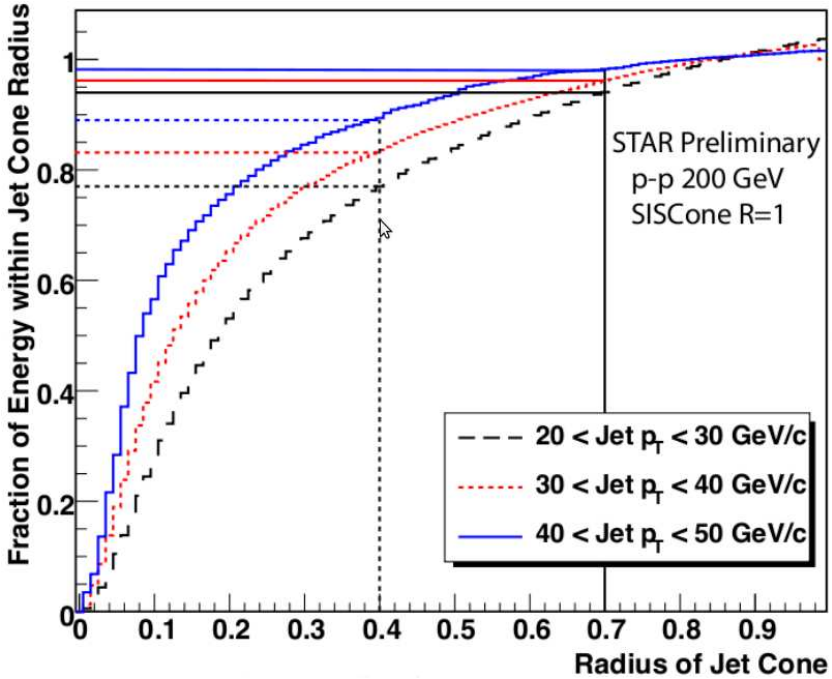

Figure 5.6: Cone radius R dependence of jet energy captured by SISCone [35] jet finder. Figure from [137].

The following steps are applied to the d+Au data being analyzed and also to the output of the detector response simulation that is described in detail in Section 5.7. After subtracting energy deposits from charged tracks off the BEMC towers, the tracks and remaining towers are used as an input to the jet finder. Kinematic cuts given only by detector acceptance are applied to the input tracks ($p_{\mathrm{T}} > 0.2$ GeV/c) and towers ($E_{\mathrm{T}} > 0.2$ GeV) to make the least possible bias to the jets. In the following this cut is marked $p_{\mathrm{T,cut}}$. Pseudorapidity cut applied to tracks and towers is $|\eta| < 0.95$. FastJet clustering is run with $\mathrm{k_T}$ and $\mathrm{anti-k_T}$ algorithms and only jets within the acceptance $|\eta| < 0.95 - R = 0.55$ are considered for further steps. Energy recombination scheme with zero mass assumption of initial towers and tracks is used to combine two protojets together.

To reject jets affected by possible occasional dead region of BEMC detector and/or BEMC detector backgrounds, the Neutral Energy Fraction NEF (fraction of jet energy coming from BEMC towers) is required to be within $0.1 < NEF < 0.9$. Due to uncertainty of the TPC tracking performance at very high p_{T}, jets containing reconstructed TPC track with $p_{\mathrm{T}} > 15$ GeV/c are rejected from further analysis.

5.6 Underlying event background subtraction

As described in Chapter 2, jets are remnants of a hard collision of two partons coming from two colliding nucleons. Even in this simple case, there are particles produced in the event which are not coming from the hard scattering and these are referred to as *underlying event* (UE). The UE was studied by the STAR collaboration in p+p collisions [19] and its study in d+Au collisions is ongoing [138]. In d+Au the underlying event is much stronger than in p+p because the mean number of binary collisions $\langle N_{bin} \rangle$ is large. In a given event it is not possible to distinguish which particle is part of UE or the jet. Instead, average density of underlying event (GeV per unit area in $\eta \times \phi$ space) is determined and subtracted from the jet energy.

Active jet areas are assigned to jets as defined in [44] and described in detail in Section 2.3. Ghost particles with nearly zero p_{T} are added to the physics event (tracks and towers) with density 100 ghosts per unit area in $\eta - \phi$ space. Active jet areas are plotted as a function of raw jet p_{T} in Figure 5.7 for $\mathrm{k_T}$ and $\mathrm{anti-k_T}$ jet algorithms. As expected, even at high p_{T} the $\mathrm{k_T}$ algorithm produces jets with larger area. But more importantly, for the $\mathrm{k_T}$ algorithm the area depends on jet p_{T} much more than for the $\mathrm{anti-k_T}$ algorithm. Also its RMS is larger, because the $\mathrm{k_T}$ algorithm is more sensitive to underlying event background. For this reason, the $\mathrm{k_T}$ algorithm will be used for background estimation in further analysis, while the $\mathrm{anti-k_T}$ algorithm will be used for the actual jet measurements.

A significant underlying event background present in d+Au collisions has to be handled. A method is used based on event-by-event determination of the back-

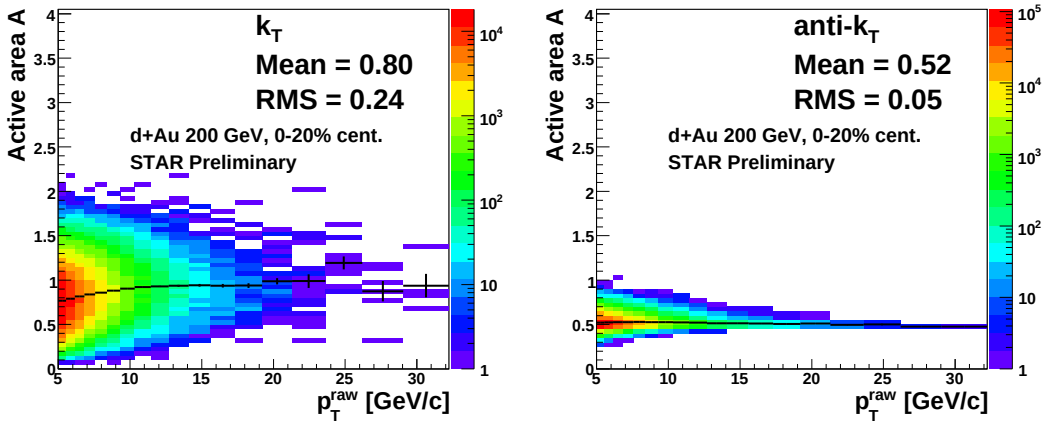

Figure 5.7: Active jet areas for $\mathrm{k_T}$ (a) and anti $-$ $\mathrm{k_T}$ (b) algorithms as a function of jet transverse momentum before background subtraction.

ground and subtraction using the active jet areas [71]. The background density ρ is determined from jets found with the $\mathrm{k_T}$ algorithm (without any jet p_T cuts):

$$\rho = \left\{ \frac{p_\mathrm{T}}{A} \right\}, \tag{5.4}$$

where p_T is jet transverse momentum and A is its active area. The information about jets and ρ is saved only for events containing at least one jet with $p_\mathrm{T} > 3$ GeV/c. For 0-20% centrality, these are about 4 million of the total 8.9M events. The distribution of background density ρ for this centrality selection is shown in Figure 5.8.

The respective background under given jet is subtracted from its measured transverse momentum:

$$p_\mathrm{T} = p_\mathrm{T}^{raw} - A \cdot \rho, \tag{5.5}$$

where A is the active area of the jet. The aforementioned background subtraction is applied by default at all levels (real data, simulation with/without background) so the underlying event is subtracted even in the case of simulated p+p collisions, where its magnitude is very small compared to d+Au.

Given that d+Au colliding system is asymmetric, the particles belonging to the underlying event will be also asymmetric in pseudorapidity. Therefore also the background will be η dependent. Since the STAR pseudorapidity acceptance for the jets is not very wide, there is no room to use the afore stated method to determine ρ in pseudorapidity bins.

Instead the tracks and towers distribution of pseudorapidity weighted by their p_T was constructed as shown in Figure 5.9. A linear parametrization was used to rescale the η-averaged background density ρ to get the η-dependent background.

At the edges of pseudorapidity acceptance the background level differs by $\approx 10\%$ with respect to the average value and the effect of this correction on inclusive jet p_{T} spectrum is only a few percent. Therefore the systematic uncertainty coming from this particular treatment of the pseudorapidity dependence of background can be neglected.

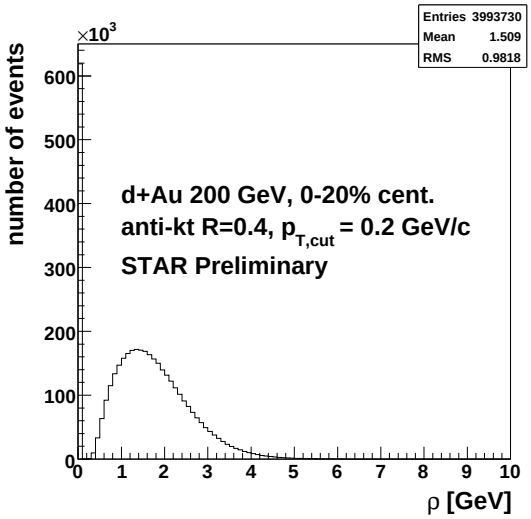

Figure 5.8: Background density ρ in 0-20% most central d+Au events. Only for events with at least one $\mathrm{k_T}$ jet with $p_{\mathrm{T}} > 3$ GeV/c.

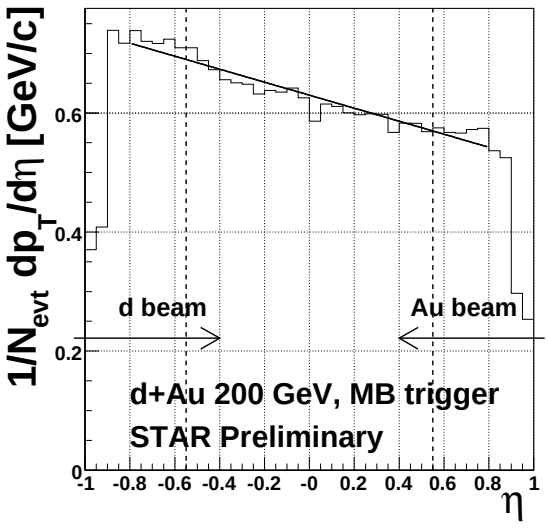

Figure 5.9: Pseudorapidity dependence of underlying event background in 0-20% most central d+Au events. The arrows show the direction of incoming beams of d and Au, the vertical lines show the fiducial jet acceptance $|\eta| < 0.55$.

With this procedure jet p_{T} is corrected for the average underlying event background in a given event. Background fluctuations within an event may still smear the jet p_{T} even if its mean value is correct. This effect is handled via mixing of jets into d+Au event as described in Section 5.7.

5.7 Monte Carlo simulation for jet corrections

The Monte Carlo (MC) simulated events are used to connect the measured jet spectrum to hadron level, that is to correct for detector effects. In addition, the simulated jet events are used to estimate and correct the residual effect of d+Au underlying event background. This chapter describes the MC events at each simulation level and the related jet reconstruction.

5.7.1 Production of MC events

Since the expected modification of jet structure in d+Au collisions is not very large (unlike the case of heavy-ion collisions), using MC jet event generator for p+p collisions such as PYTHIA [29] is justified. PYTHIA version 6.410 with CDF Tune A setting [139] was used to generate QCD jet events. To cover sufficient range of jet p_{T}, the kinematic parameters CKIN(3) and CKIN(4) of PYTHIA have to be used: it would be very computationally expensive to generate minimum bias events, because the jet p_{T} spectrum is steeply falling.

In PYTHIA $\hat{p}_{\mathrm{T}}$ is the p_{T} of hard scattered partons in their center-of-mass frame, also referred to as "pt hard". Due to initial and final state interaction, $\hat{p}_{\mathrm{T}}$ is only indirectly connected to the jet p_{T} and therefore a wider range of $\hat{p}_{\mathrm{T}}$ has to be used for jet study in a particular jet p_{T} region. For this work 11 intervals of $\hat{p}_{\mathrm{T}}$ are selected by PYTHIA parameters CKIN(3) and CKIN(4). Events in separate pt hard bins are weighted (in addition to the usual $1/N_{events}$ weighting) by their cross section σ to get a smooth distribution of jet p_{T} over the range covered by this simulation. The details about the 11 pt hard bins are shown in Table 5.4.

PYTHIA is set to treat weekly and electromagnetically decaying particles as stable (that is, the octet of pseudoscalar mesons, the baryon octet, the Ω^- and the corresponding anti-baryons are not decayed in PYTHIA) and these particles from the PYTHIA record are used to run the jet finder at hadron level. Figure 5.10 shows the weighted contributions of the individual pt hard bins to the total inclusive jet p_{T} spectrum in $|\eta| < 0.55$ and their sum. As expected the resulting p_{T} spectrum is flat. This sample of jets found at PYTHIA hadron level will be referred to as "PyMC" in further text.

CKIN(3)	CKIN(4)	Number of events	$\sigma(m\mathrm{b})$
3	4	720000	1.30
4	5	720000	3.15×10^{-1}
5	7	420000	1.36×10^{-1}
7	9	419000	2.30×10^{-2}
9	11	418000	5.50×10^{-3}
11	15	416000	2.22×10^{-3}
15	25	400000	3.90×10^{-4}
25	35	498000	1.02×10^{-5}
35	45	119000	5.02×10^{-7}
45	55	118000	2.86×10^{-8}
55	65	120000	1.45×10^{-9}

Table 5.4: Kinematic cuts CKIN(3) and CKIN(4), number of events and event cross section for MC events generated by PYTHIA.

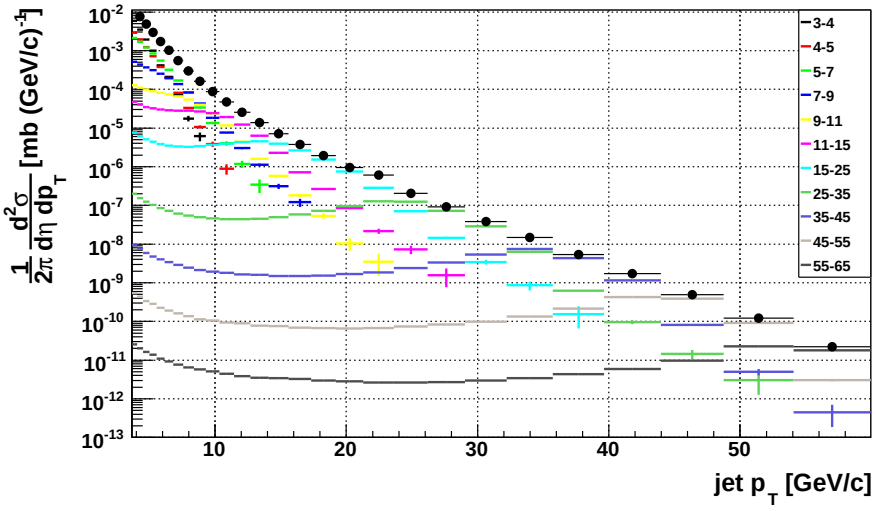

Figure 5.10: Jet spectrum for PYTHIA hadron level (anti $-$ k_T algorithm, R=0.4). The weighted jet p_T spectra from the 11 individual pt hard bins are shown by the color lines and the weighted sum is shown by the black points.

5.7.2 Detector response

Using GEANT 3 based detector model, the particles from PYTHIA events are propagated through the STAR detector, including their electromagnetic and weak decays and their products. Based on the GEANT energy deposits, the response of the detectors is simulated using STAR simulation software: TPC Response Simulator (TRS) and BEMC simulator (StEmcSimulatorMaker).

The BEMC simulator translates the energy deposit in the scintillation layers to the number of primary photoelectrons and simulates their multiplication on the individual dynodes of the photomultiplier, including the Poisson smearing of the electron counts at each step (leading to the desired energy resolution). The same acceptance for the BEMC as in the real data is achieved by masking out the BEMC towers which are either dead or hot in the real data (see Section 5.4 for details).

The TRS simulates the drifting of electrons, their multiplication with the MWPCs and the readout electronics, delivering the ADC signal in the same format as in real data. This information is then used to find the clusters and the standard tracking software is used to reconstruct tracks. The same cuts are applied as to those in the real data. However, due to the large detector backgrounds (especially event pile-up in the TPC), the tracking efficiency in the TPC may be in fact lower than that obtained from this pure simulation. To quantify this effect, the simulation of single particle π^+ embedded into raw data (this is referred to as *embedding*) was performed and the resulting tracking efficiency compared to that from the pure simulation. Figure 5.11 shows that the realistic performance of the TPC is about 10% worse than in the pure simulation.

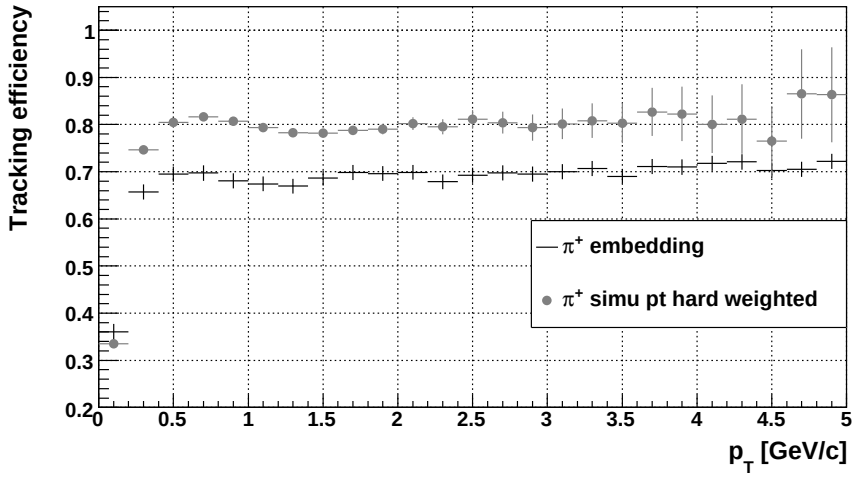

Figure 5.11: Tracking efficiency for π^+ in embedding and simulation (weighted average over the pt hard bins).

To correct for this rather big difference, the reconstructed tracks from the simulation are artificially randomly discarded according to the difference in the tracking efficiencies, so that the realistic ("embedding") tracking efficiency is achieved. These tracks and towers from the BEMC simulator are then used to define jets at detector level, marked as "PyGe".

Even after underlying event background subtraction according to Eq. 5.5 there is a remaining effect of background fluctuations within one event. To assess this, simulated tracks and towers are mixed with tracks and towers from real d+Au events (with centrality selection of interest) and jet finder is run at the hybrid events, producing the "PyBg" sample of jets.

5.7.3 Jet reconstruction performance

To measure the jet reconstruction performance, the PyMC, PyGe and PyBg jets reconstructed in each event are matched. For each PyMC jets the nearest (based on $r = \sqrt{\Delta\phi^2 + \Delta\eta^2}$) jet in PyGe and PyBg jets is found and the matching is done if $r < 0.2$. In the following figures, the PyBg jets are reconstructed in events with centrality 0-20%.

Figure 5.12 shows the distribution of angular $(\Delta\phi, \Delta\eta)$ difference between PyGe jets and PyMC jets selected within $20 < p_{\mathrm{T}} < 30$ GeV/c. It can be seen from Figure 5.13 that the angular resolution (determined as standard deviation of the distribution) for PyBg jets is slightly worse than for PyGe (effect of d+Au UE background) and that the resolution improves with increasing jet p_{T}. Given these resolutions, it is obvious that the cut $r < 0.2$ for matching is broad enough and

could be even lowered if the background was more severe.

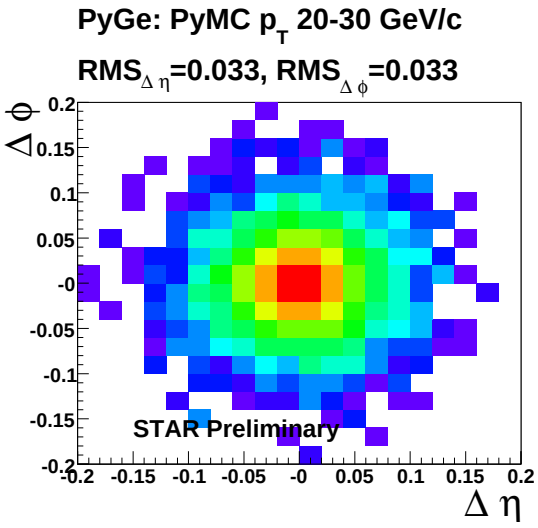

Figure 5.12: Angular difference of PyGe jets found as nearest to PyMC jet with $20 < p_{\mathrm{T}} < 30$ GeV/c.

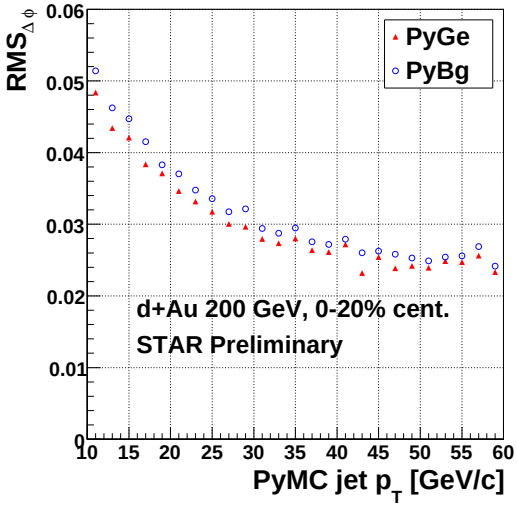

Figure 5.13: Angular resolution (standard deviation) of PyGe and PyBg jets (0-20% centrality) as function of PyMC jet p_{T}.

The jet energy scale (JES) is shown in Figure 5.14, where mean jet p_{T} in PyGe and PyBg samples is plotted versus PyMC jet p_{T}. The overall deficit is caused by detector inefficiencies (TPC tracking efficiency, BEMC acceptance), missing of some neutral particles (especially $\mathrm{K}^0_{\mathrm{L}}$ and neutrons) and 100% hadronic correction [7]. Figure 5.15 shows the mean PyMC jet p_{T} contributing to given jet p_{T} in the PyGe (PyBg) sample. This folds the steeply falling jet p_{T} spectrum and the detector (detector+background) effects and shows a big effect of jet p_{T} smearing.

The relative jet p_{T} resolution is plotted in Figure 5.16: PyBg resolution is slightly worse than PyGe due to underlying event background. PyGe p_{T} resolution remains nearly constant around 22% and is given mainly by the fluctuation of undetected jet components, since the TPC and BEMC momentum resolutions are both below 10% for majority of jet particles.

As discussed in Section 5.5 the jets are only accepted if the maximum p_{T} of any track in the jet is not greater than 15 GeV/c. Figure 5.17 shows the fraction of jets in the PYTHIA simulation satisfying this condition. It is above 80% for jets with $p_{\mathrm{T}} < 30$ GeV/c.

The simulation jet samples (PyMC, PyGe, PyBg) and their matching will be used to correct the measured jets to hadron level. Corrections will slightly differ for individual measurements and will be described in detail in the corresponding sections.

[7] described in Section 5.4

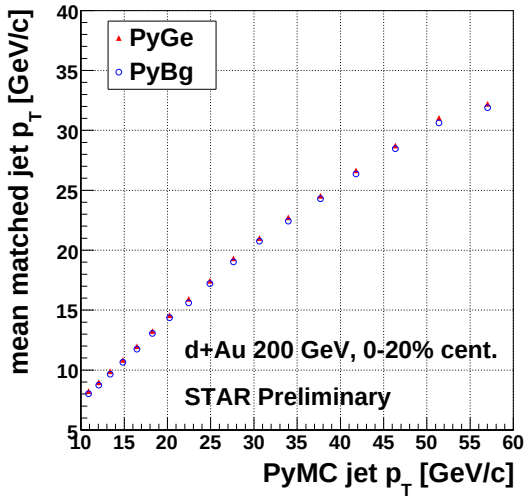

Figure 5.14: Jet energy scale for PyGe and PyBg (0-20% centrality) jets.

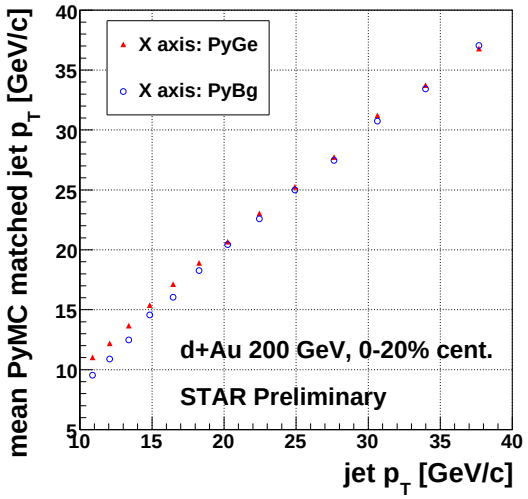

Figure 5.15: Mean hadron level (PyMC) jet p_{T} contributing to given jet p_{T} at PyGe, PyBg energy scale.

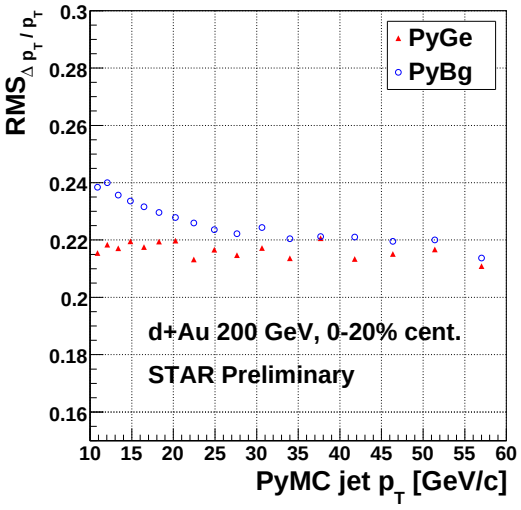

Figure 5.16: Relative jet p_{T} resolution with respect to the PyMC jets. Note the suppressed zero in the Y axis.

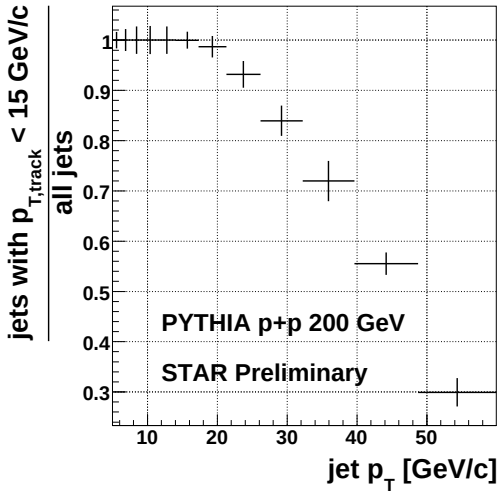

Figure 5.17: Fraction of jets in PYTHIA simulation (detector level) accepted by the cut on maximum p_{T} of a track in the jet $p_{\mathrm{T},track} < 15$ GeV/c.

Chapter 6

Inclusive jet measurement

Extracting per-event inclusive jet yield involves reconstructing jets from the data and applying the corrections based on MC simulation. This includes estimation of the systematic uncertainties coming from the techniques used, such as various selection criteria and the level to which the simulation describes the reality. In this chapter two main physics results are presented: jet yield measurement in central (0-20%) d+Au collisions in comparison to an older measurement in p+p collisions and new measurement of centrality dependence of jet R_{CP} in d+Au collisions. The jet spectrum in 0-20% d+Au collisions was presented in [140], using the same method but differing in the centrality definition and in the calculation of systematic uncertainties.

6.1 Corrections to jet spectra

The PYTHIA simulation described in Section 5.7 is used for the correction of detector effects (PyGe vs. PyMC) and background fluctuations. For this purpose, the PyBg jet sample is used, but one has to keep in mind that it contains jets from both PYTHIA and real d+Au events that the PYTHIA events were mixed with. The weights for pt hard bins apply to the real d+Au events also, since they are given to the whole hybrid events - PYTHIA plus real d+Au data. In the lowest pt hard bins the event weights are large, therefore the jets from real data will be most visible there.

If the PYTHIA was minimum-bias (i.e., pt hard going to zero), the ratio of per-event jet yields in PYTHIA and in d+Au real data would be $1/\langle N_{bin}\rangle$, assuming $\langle N_{bin}\rangle$ scaling of jet production and PYTHIA cross-section same as in p+p. Even though the simulation is enhanced in jets - the total cross-section of PYTHIA events taken from Table 5.4 is 1.8 mb, only 4% of the total p+p inelastic cross section of 42 mb - the jets coming from real d+Au events can not be neglected. Therefore in the following, only those PyBg jets are used that are matched to PyGe jet with

$r < 0.15$ (distance in $\Delta\eta \times \Delta\phi$ space), to reduce the contamination by jets from real d+Au events. This jet sample will be referred to as "PyBgMatched".

The method used for spectrum correction is the so called bin-by-bin correction. It is based on the ratio of jet spectrum in the MC simulation "before" and "after" the effect to be corrected. In practice, the ratio of PyMC to PyBgMatched is calculated and used as correction factor that is applied bin-by-bin to the measured jet p_{T} spectrum. This ratio is plotted in Figure 6.1. The statistical errors in individual p_{T} bins of PyMC and PyBgMatched spectra are not completely independent, which has to be taken into account in the calculation of the statistical errors for the correction. Let us define MC to be the yield of PyMC jets, Bg that of PyBgMatched jets with σ_{MC}, σ_{Bg} marking their statistical errors. Further σ_{Cov} is the statistical error for jets which are in the same bin for both PyMC and PyBgMatched samples. Then taking this covariance into account the statistical error on the ratio is calculated as:

$$\sigma\left(\frac{MC}{Bg}\right) = \frac{MC}{Bg}\sqrt{\frac{\sigma_{MC}^2}{MC^2} + \frac{\sigma_{Bg}^2}{Bg^2} - 2\cdot\frac{\sigma_{Cov}^2}{MC\cdot Bg}} \tag{6.1}$$

The detector response and background fluctuations cause migration between the bins in jet p_{T} spectrum. The effect of this migration on the spectrum depends on the *shape* of the spectrum. Therefore, the shape of the spectrum in the real data (uncorrected) and in the simulation (PyBgMatched) has to be the same for the bin-by-bin correction to be applicable. This comparison is shown in Figure 6.2, where the ratio is plotted and is consistent with constant within 10%, which is sufficient. The agreement is good keeping in mind that jet yield drops by three orders of magnitude over the p_{T} range considered.

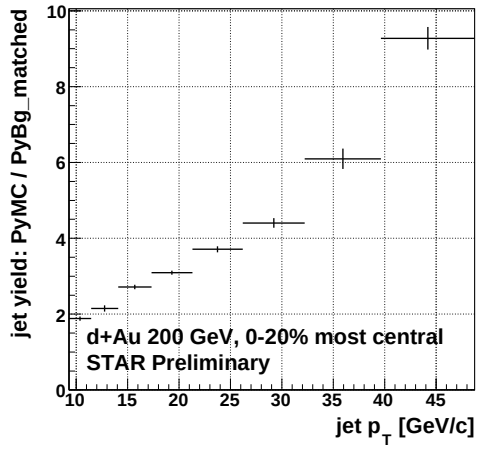

Figure 6.1: Ratio of jet p_{T} spectra from the simulation: PyMC / PyBgMatched, used in the bin-by-bin correction.

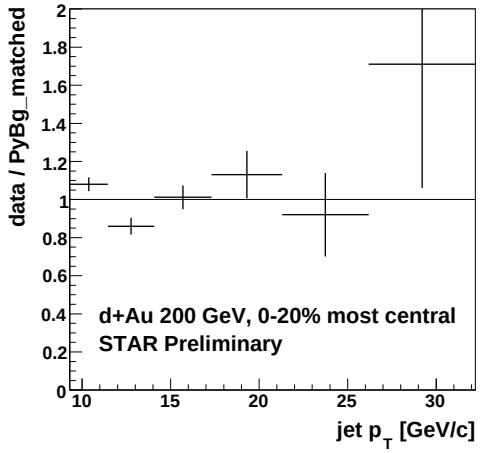

Figure 6.2: Ratio of jet p_{T} spectrum in data over that in simulation (PyBgMatched). It is consistent with constant within 10 %.

The agreement of data and simulation jet spectrum shown in Figure 6.2 also indicates that the background fluctuations are properly described by the simulation for reconstructed jet $p_{\mathrm{T}} > 9$ GeV/c. In other words the contribution of fake jets, the objects found by jet finder not connected to the hard scattering, is negligible in this p_{T} range. As an independent cross check for fake jets an azimuthal di-jet correlation method is used, described in more detail in Chapter 7. Figure 7.2 shows a clear di-jet peak with no significant uncorrelated background even for jet p_{T} as low as 7 GeV/c. If there was a significant contribution of fake jets it would be visible in this plot.

6.2 Jet spectrum in 0-20% most central d+Au collisions

The inclusive jet spectrum was extracted from 0-20% most central d+Au collisions in the acceptance $|\eta| < 0.55$ and the range $9.3 < p_{\mathrm{T}} < 32.2$ GeV/c. The jet p_{T} bins were taken from a previous jet measurement in STAR [20] to make a direct comparison possible. The bin-by-bin correction was used to correct the spectrum to hadron level including the correction for underlying event background. Apart from the inherent statistical precision of the simulation, the correction procedure involves several systematic uncertainties, coming from the understanding of the detector response and the treatment of the underlying event background.

6.2.1 Systematic uncertainties

The detector response simulation that translates PYTHIA hadron level jets to detector level jets depends on the accurate knowledge of the TPC tracking efficiency and on the energy scale of the BEMC in the real data. These will influence the Jet Energy Scale (JES) and as such represent a major contribution of the total systematic uncertainty. The possible uncertainty coming from the requirement of a specific jet fragmentation by the cut track $p_{\mathrm{T}} < 15$ GeV/c is negligible, since the acceptance of this cut is very high in the jet p_{T} range covered by this analysis, as shown in Figure 5.17.

The simulation uses the accurately determined tracking efficiency of positive pions to scale the tracking efficiencies of other particles (as described in Section 5.7). This π^+ embedding has itself systematic uncertainty of tracking efficiency around 5%. Since its use for other particle species may introduce other effects, a conservative value for the TPC tracking efficiency uncertainty is used: 10%. To evaluate its impact on the jet spectrum the tracking efficiency in the simulation was artificially altered by $\pm 10\%$ and the jet finder was run.

The uncertainty of the BEMC energy scale in run 8 d+Au data is 5%. This involves both uncertainties due to its calibration and due to accuracy of modeling of electromagnetic showers. Its impact was evaluated by increasing (decreasing) the neutral energy of jets by 5% and observing its effect on the spectrum. This was done in both real data and the simulation, showing good agreement. The final uncertainties were taken from the simulation due to better statistical precision.

The treatment of background relies on matching the jets in the PyBgMatched sample. The nominal proximity cut for matching in the $\Delta\eta \times \Delta\phi$ space is $r < 0.15$. Values of $r = 0.1$ and $r = 0.2$ were used to set the systematic uncertainty coming from this cut.

6.2.2 Results

The normalized per-event jet yield ($\frac{1}{2\pi}\frac{1}{N_{evt}}\frac{d^2N}{d\eta dp_{\mathrm{T}}}$) was measured and corrected in six p_{T} bins and the values span over almost three orders of magnitude. The results are detailed in Table 6.1, including the break down of the systematic uncertainty. Tracking efficiency uncertainty represents the major contribution to the systematic uncertainty in this measurement.

p_{T} [GeV/c]	$yield \pm stat. \pm syst.$ [(GeV/c)$^{-1}$]	systematic uncertainties [(GeV/c)$^{-1}$]		
		tracking	BEMC	background
$9.3 - 11.4$	$(6.07 \pm 0.21^{+1.09}_{-1.28}) \times 10^{-5}$	$^{+0.85}_{-1.03} \times 10^{-5}$	$^{+0.61}_{-0.55} \times 10^{-5}$	$^{+0.32}_{-0.53} \times 10^{-5}$
$11.4 - 14.1$	$(1.41 \pm 0.07^{+0.30}_{-0.29}) \times 10^{-5}$	$^{+0.25}_{-0.23} \times 10^{-5}$	$^{+0.16}_{-0.16} \times 10^{-5}$	$^{+0.06}_{-0.10} \times 10^{-5}$
$14.1 - 17.3$	$(4.61 \pm 0.29^{+1.05}_{-0.94}) \times 10^{-6}$	$^{+0.88}_{-0.78} \times 10^{-6}$	$^{+0.55}_{-0.46} \times 10^{-6}$	$^{+0.15}_{-0.24} \times 10^{-6}$
$17.3 - 21.3$	$(1.35 \pm 0.15^{+0.34}_{-0.29}) \times 10^{-6}$	$^{+0.28}_{-0.24} \times 10^{-6}$	$^{+0.18}_{-0.15} \times 10^{-6}$	$^{+0.03}_{-0.06} \times 10^{-6}$
$21.3 - 26.2$	$(2.48 \pm 0.59^{+0.68}_{-0.59}) \times 10^{-7}$	$^{+0.57}_{-0.47} \times 10^{-7}$	$^{+0.37}_{-0.35} \times 10^{-7}$	$^{+0.05}_{-0.08} \times 10^{-7}$
$26.2 - 32.2$	$(9.19 \pm 3.49^{+2.82}_{-2.55}) \times 10^{-8}$	$^{+2.20}_{-1.93} \times 10^{-8}$	$^{+1.75}_{-1.65} \times 10^{-8}$	$^{+0.15}_{-0.25} \times 10^{-8}$

Table 6.1: Inclusive jet yield $\frac{1}{2\pi}\frac{1}{N_{evt}}\frac{d^2N}{d\eta dp_{\mathrm{T}}}$ in 0-20% most central d+Au collisions in $|\eta < 0.55|$.

As the first step to estimate the cold nuclear matter effects on jet production in d+Au collisions the jet spectrum was compared to the existing jet spectrum measurement in $\sqrt{s} = 200$ GeV p+p collisions from STAR [20], that was done with the Mid Point Cone algorithm with $R = 0.4$. The p+p cross-section was rescaled to the level of per-event yield in d+Au collisions assuming binary collisions scaling:

$$yield = \sigma * \frac{\langle N_{bin} \rangle}{\sigma_{\mathrm{inel}}}, \tag{6.2}$$

where $\langle N_{bin} \rangle = 14.6 \pm 1.7$ is for 0-20% d+Au collisions and $\sigma_{inel} = 42$ mb is the p+p inelastic cross section.

The d+Au spectrum and the rescaled p+p spectrum are shown in Figure 6.3. The normalization uncertainties include 8% uncertainty on the luminosity in p+p and 6.4% uncertainty of $\langle N_{bin} \rangle / \sigma_{inel}$. As described in Section 5.2, half of the total 9% systematic uncertainty on $\langle N_{bin} \rangle$ comes from uncertianty of σ_{inel}, so this contribution gets canceled in the ratio.

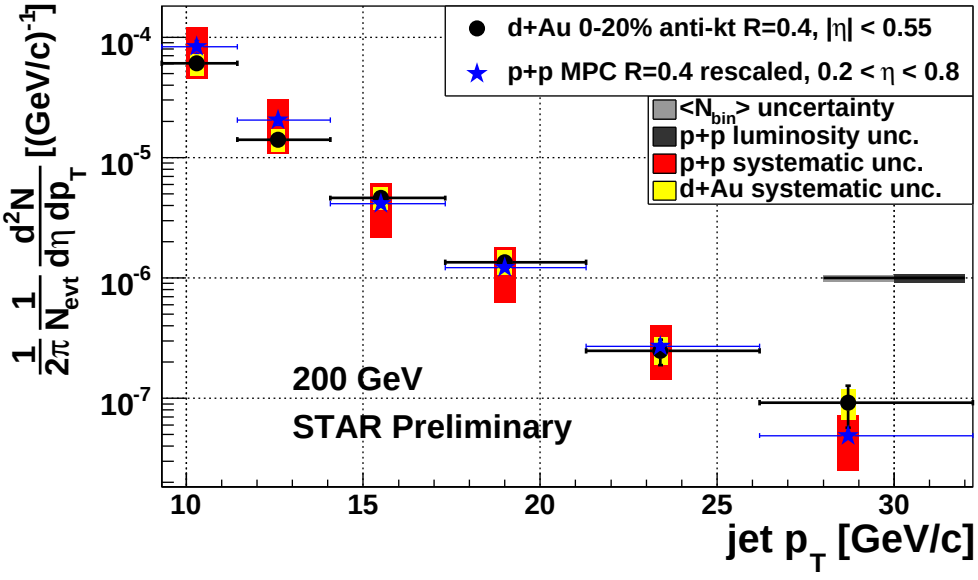

Figure 6.3: Jet spectrum in 0-20% d+Au collisions compared to the $\langle N_{bin} \rangle$ scaled spectrum in p+p, taken from [20].

With the current large systematic uncertainties, the $\langle N_{bin} \rangle$ rescaled p+p spectrum is consistent with the result from d+Au. There are several ways to measure the cold nuclear matter effects with smaller systematic uncertainties. These will be further discussed.

It is important to verify the effect of different pseudorapidity acceptances between the d+Au and p+p jet spectra shown in Figure 6.3. For this purpose jet reconstruction with $R = 0.4$ anti $-$ k$_T$ algorithm was run in hadron level PYTHIA simulation for the two acceptances: $0.2 < \eta < 0.8$ and $|\eta| < 0.55$. The comparison shown in Figure 6.4 shows that the effect is around 10% in the p_T range $10 - 30$ GeV/c. At larger p_T this effect becomes much stronger, which can be easily understood in the $2 \rightarrow 2$ partonic kinematics as phase space effect. With rising jet p_T the pseudorapidity distribution of jets becomes narrower and at kinematic limit of $p_T = 100$ GeV/c the jets must have $\eta = 0$ otherwise the energy would not conserve. This effect has to be kept in mind for a quantitative comparison.

A newer, not yet published, jet p_T spectrum from p+p collisions is available from

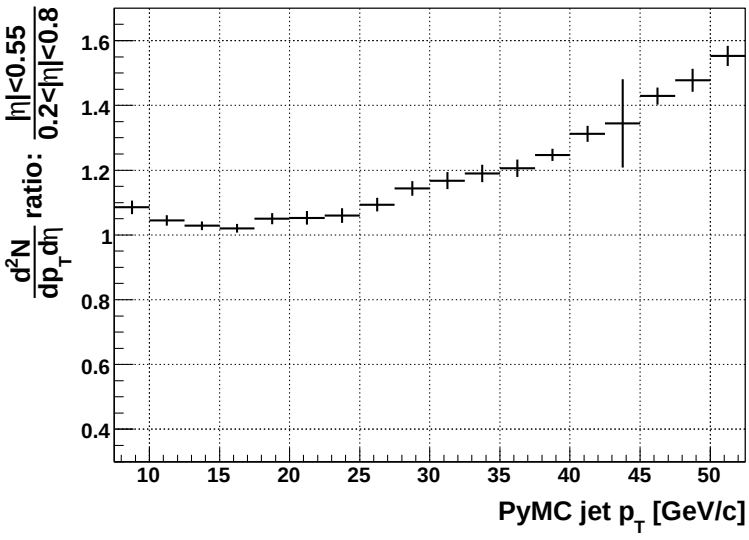

Figure 6.4: Ratio of PYTHIA hadron level jet p_{T} spectra for different pseudorapidity selections.

STAR [141] with reduced systematic uncertainties and also symmetric pseudorapidity interval. The jet finder used is again the Mid Point Cone with $R = 0.4$ and binary collisions rescaling was done to compare to d+Au collisions. The normalization uncertainty due to luminosity is 7.6%. The comparison to d+Au collisions shown in Figure 6.5 shows again that within the current uncertainties the jet production in 0-20% d+Au collisions shows scaling with $\langle N_{bin} \rangle$.

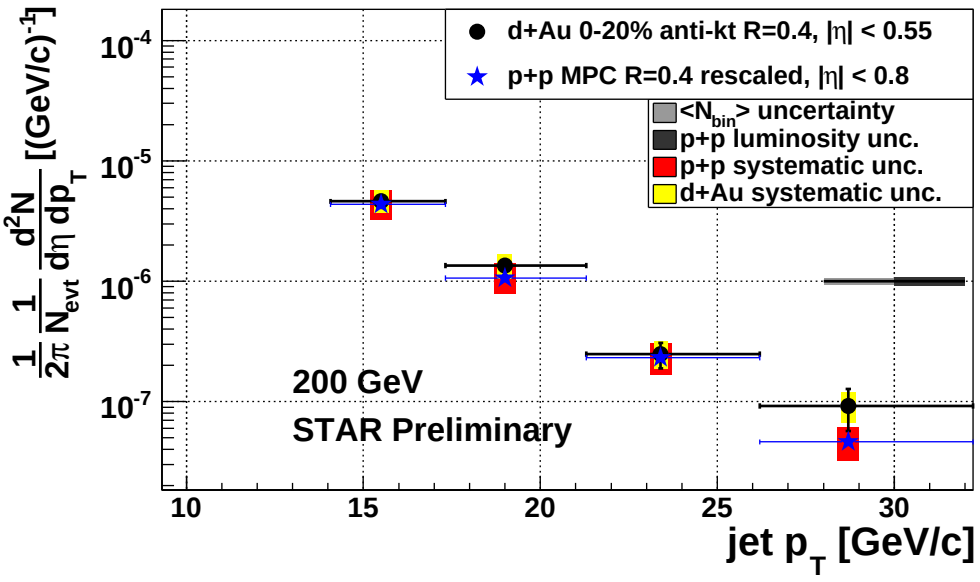

Figure 6.5: Jet spectrum in 0-20% d+Au collisions with the rescaled preliminary spectrum in p+p, taken from [141].

The values of the data points for the jet cross section in p+p collisions used in the previous comparisons are shown in Table 6.2. The systematic uncertainties of the preliminary [141] p+p cross section are dominated by the 4.8% uncertainty on BEMC calibration. It has, however, much bigger impact than in the case of the presented results from d+Au collisions, because the p+p measurement is based on BEMC-triggered data. The events are triggered by a deposit of $E_{\mathrm{T}} > 8.3$ GeV in a patch of BEMC and the efficiency of this trigger depends on BEMC calibration. Also the use of this trigger naturally increases the neutral energy fraction in jets with respect to the the unbiased one (as in d+Au). Therefore the sensitivity to BEMC calibration is much higher in p+p than in d+Au.

p_{T} [GeV/c]	$\sigma \pm \delta\sigma(stat.) \pm \delta\sigma(syst.)$ [pb (GeV/c)$^{-1}$] published	$\sigma \pm \delta\sigma(stat.) \pm \delta\sigma(syst.)$ [pb (GeV/c)$^{-1}$] preliminary
$9.3 - 11.4$	$(2.40 \pm 0.30 \pm 1.10) \times 10^5$	-
$11.4 - 14.1$	$(5.90 \pm 0.60 \pm 2.80) \times 10^4$	-
$14.1 - 17.3$	$(1.19 \pm 0.10 \pm 0.57) \times 10^4$	$(1.25 \pm 0.05^{+0.39}_{-0.33}) \times 10^4$
$17.3 - 21.3$	$(3.50 \pm 0.20 \pm 1.70) \times 10^3$	$(3.05 \pm 0.10^{+1.05}_{-0.78}) \times 10^3$
$21.3 - 26.2$	$(7.80 \pm 0.40 \pm 3.70) \times 10^2$	$(6.67 \pm 0.33^{+2.17}_{-1.83}) \times 10^2$
$26.2 - 32.2$	$(1.41 \pm 0.09 \pm 0.68) \times 10^2$	$(1.33 \pm 0.06^{+0.44}_{-0.39}) \times 10^2$

Table 6.2: Inclusive jet cross section $\sigma : \frac{1}{2\pi}\frac{d^2\sigma}{d\eta dp_{\mathrm{T}}}$ in $\sqrt{s} = 200$ GeV p+p collisions. Published results from [20] and preliminary results [141].

Despite the improvement in the reference p+p jet cross section, the systematic uncertainties are still large to be able to construct meaningful nuclear modification factor R_{dAu} for jets. Work is currently ongoing to achieve smaller uncertainty of TPC tracking efficiency in the simulation for d+Au collisions. The simulated PYTHIA jet events will be embedded into d+Au detector background events at raw data level. This will decrease the tracking efficiency uncertainty below 5%.

Another way is to use as a reference system for 0-20% most central d+Au collisions measurement that has correlated systematic uncertainties. One option is a use of p+p collisions from RHIC run 8 (here the BEMC calibration is identical) - jet spectrum analysis using this data is planned in the future. Another option, presented in Section 6.3, is to use different centralities in the same d+Au dataset, that is to construct the R_{CP} ratio. In this case, almost all uncertainties related to detector are correlated between different centralities.

6.3 Centrality dependence of d+Au jet yields: jet R_{CP}

This section presents centrality dependence in the form of $\langle N_{bin} \rangle$-scaled spectra ratios of jet yields in d+Au collisions. The jet spectra are not corrected to hadron level. Instead, they are only corrected for the centrality dependent background fluctuations, so the jet energy scale of the resulting R_{CP} corresponds to detector level jets, which is acceptable due to very modest p_{T} dependence of R_{CP}. The approximate mapping to hadron level jet energy scale can be made using the jet energy scale shown in Figure 5.15.

As seen in the previous section, except for the highest jet p_{T} the measurement of jet spectra are dominated by systematic uncertainties. Even though the statistical errors are larger in the peripheral bins (20-40%, 40-100%), the uncorrelated systematic uncertainties between various centralities are very small. The only major detector-related uncertainty between central and peripheral collisions is 0.5% uncertainty on TPC tracking efficiency, determined from π^+ embedding. It is not surprising that the difference is small: uncorrected charged track densities $dN_{ch}/d\eta$ are between 7 (peripheral) to 17 (central) in d+Au coillisions, while the TPC was designed to measure central Au+Au collisions with $dN_{ch}/d\eta \approx 500$. Its impact on R_{CP} is about 1% which is much less than other uncertainties.

Two different correction methods with different treatment of d+Au underlying event background are presented: bin-by-bin correction and a method based on a more detailed study of background fluctuations (denoted as Δp_{T}). The systematic uncertainty of R_{CP} coming from centrality definition (via the ratio of $\langle N_{bin} \rangle$) is 9%: summing in quadrature the 6.4% part of $\langle N_{bin} \rangle$ uncertainty that is not correlated between different centralities (see Section 5.2 for details).

6.3.1 Bin-by-bin correction

To obtain the corrected R_{CP} via the bin-by-bin correction, the following formula is applied bin-by-bin to two centralities:

$$Corrected(c,i) = \frac{Raw(c,i)}{PyBgMatched(c,i)} \times PyMC(i), \tag{6.3}$$

where c is centrality bin, i is p_{T} bin and Raw is the measured p_{T} spectrum. Because the $PyMC(i)$ terms cancel out in the ratio of corrected spectra when constructing the R_{CP}, the resulting formula can be written as:

$$R_{\mathrm{CP}}(c1/c2,i) = \frac{Raw(c1,i)}{Raw(c2,i)} \times \frac{PyBgMatched(c2,i)}{PyBgMatched(c1,i)} \times \frac{\langle N_{bin} \rangle (c2)}{\langle N_{bin} \rangle (c1)} \tag{6.4}$$

The term $\frac{PyBgMatched(c2,i)}{PyBgMatched(c1,i)}$ is the correction for background fluctuations and its value for the centrality ratios 0-20%/40-100% and 20-40%/40-100% is shown in Figure 6.6. The nominal value of the proximity cut in $\Delta\eta\times\Delta\phi$ space for PyBgMatched jet matching is $r < 0.15$. The values of $r < 0.1$, $r < 0.2$ are used to estimate the systematic uncertainty coming from background treatment.

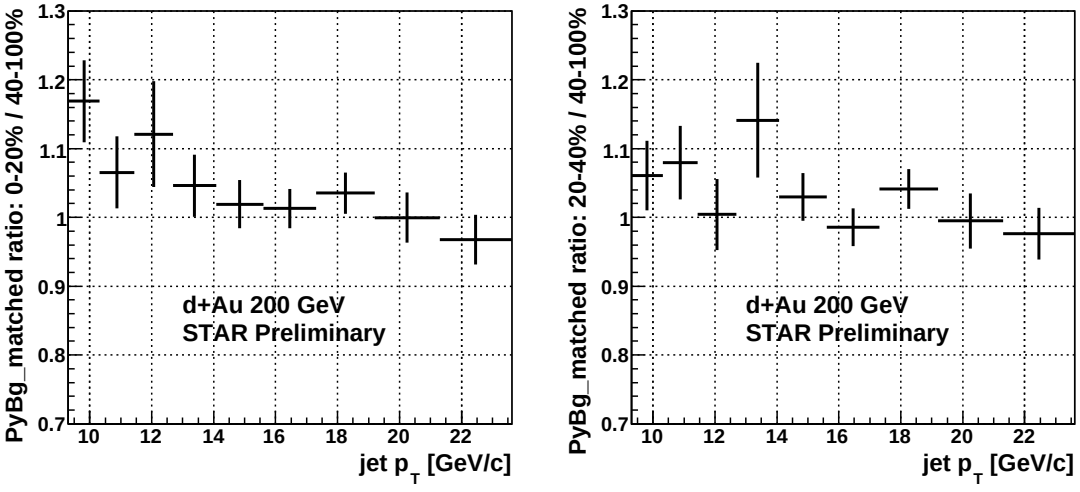

Figure 6.6: Bin-by-bin correction used to obtain jet $R_{\rm CP}$. Left: 0-20% centrality, right: 20-40% centrality. Nominal value $r < 0.15$ for proximity matching (PyBgMatched) is used.

Applying the correction of Eq. 6.4 to the measured jet $p_{\rm T}$ spectra leads to the corrected $R_{\rm CP}$, as shown in Figure 6.7. The systematic uncertainties due to the background treatment are shown by the blue lines and only play significant role for most central bin and lower $p_{\rm T}$ jets. The $p_{\rm T}$ integrated values of $R_{\rm CP}$ in intervals $9.3 < p_{\rm T} < 14.1$ GeV/c, $p_{\rm T} > 14.1$ GeV/c with statistical errors are shown in the figures. The $R_{\rm CP}$ shows a significant enhancement for jets with $9.3 < p_{\rm T} < 11.4$ GeV/c in 0-20% most central collisions.

6.3.2 Background fluctuations in detail: $\Delta p_{\rm T}$ correction

An approach to study the background fluctuations on jet-by-jet basis rather than their inclusive effect on spectra (as in bin-by-bin collisions) has been used in jet analyses in Au+Au collisions in STAR [74, 142]. The idea is to extract the distribution of jet $p_{\rm T}$ difference between the matched jets in PyBg and PyGe jet samples:

$$\Delta p_{\rm T} = p_{\rm T}(PyBg) - p_{\rm T}(PyGe), \tag{6.5}$$

where the UE background was already subtracted from $p_{\rm T}(PyBg)$, contrary to the definition of $\delta p_{\rm T}$ in [142]. It was shown in [142] that the $\Delta p_{\rm T}$ distribution in central

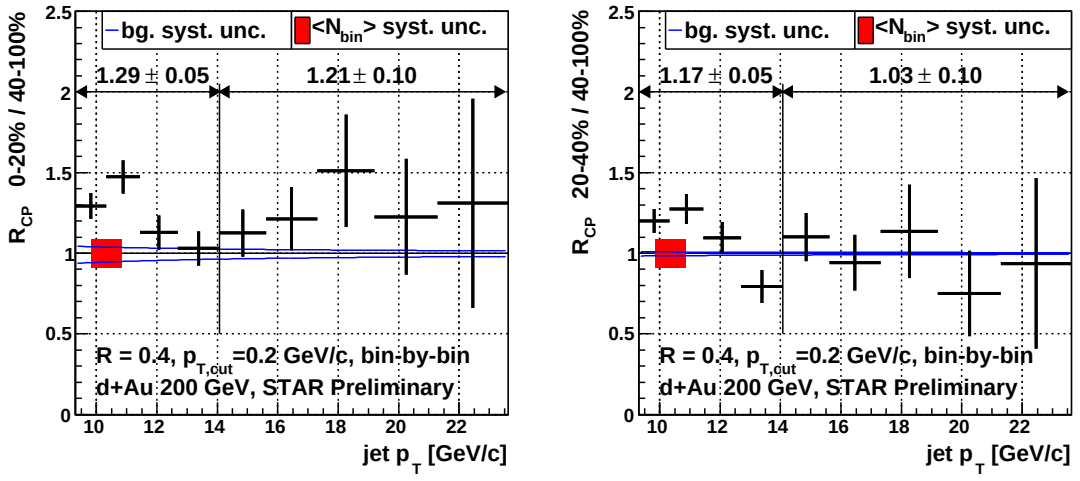

Figure 6.7: Jet R_{CP} in 200 GeV d+Au collisions obtained for two centrality bins using the bin-by-bin correction. Jet algorithm anti $-$ k$_{\mathrm{T}}$ with $R = 0.4$ and $p_{\mathrm{T,cut}} = 0.2$ GeV/c was used. The p_{T} integrated R_{CP} values with statistical errors are shown in the figures.

Au+Au collisions is well described by the independent emission model [143].

To construct the Δp_{T} distribution the nearest (in $\Delta\eta \times \Delta\phi$ space) PyBg jet to a given PyGe jet is found within $r < 0.2$. The distribution of Δp_{T} for jets with $10.3 < p_{\mathrm{T}}(PyGe) < 19.2$ GeV/c is shown in Figure 6.8, showing a narrow Gaussian centered approximately around zero with wide tails both negative and positive. The negative ($\Delta p_{\mathrm{T}} << 0$) tail does not play an important role for the jet spectrum, as expected for downwards fluctuations on a steeply falling spectrum. But it is easily avoided by setting a new ("balance") condition for matching: $p_{\mathrm{T}}(PyBg) > 0.75\ p_{\mathrm{T}}(PyGe)$. This was applied also to the bin-by-bin correction as systematic cross check but it did not change the final spectrum by more than 1%. The Δp_{T} distribution using this balance condition is shown in Figure 6.9.

The distribution of Δp_{T} clearly shows a non-trivial structure which can not be described by the independent emission model. Instead a double Gaussian fit was used to describe the shape of Δp_{T} distribution with no particular physics justification. An example of the fit result can be seen in Figure 6.9. The main Gaussian is peaked at slightly negative Δp_{T} (this may be due to a contamination of background density ρ with jets, causing a slight over-subtraction of background). This fit describes the distribution over three orders of magnitude. Even though it does not get the remaining $\Delta p_{\mathrm{T}} >> 0$ tail completely, it is sufficient to account for the bulk of the background fluctuations. To estimate the systematic uncertainty coming from this fit, the procedure was repeated for different values of matching parameter ($r < 0.1$, $r < 0.2$), p_{T} ranges: $10.3 < p_{\mathrm{T}}(PyGe) < 19.3$ GeV/c, $p_{\mathrm{T}}(PyGe) > 19.3$ GeV/c and with and without the balance cut $p_{\mathrm{T}}(PyBg) > 0.75\ p_{\mathrm{T}}(PyGe)$. The resulting fit

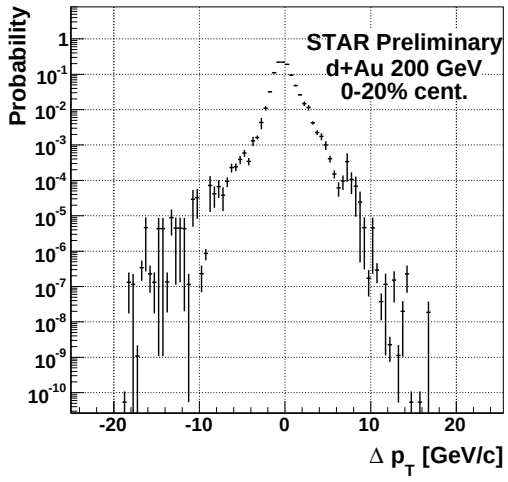

Figure 6.8: Distribution of $\Delta p_{\rm T}$ for jets with $10.3 < p_{\rm T}(PyGe) < 19.3$ GeV/c, matching condition $r < 0.2$.

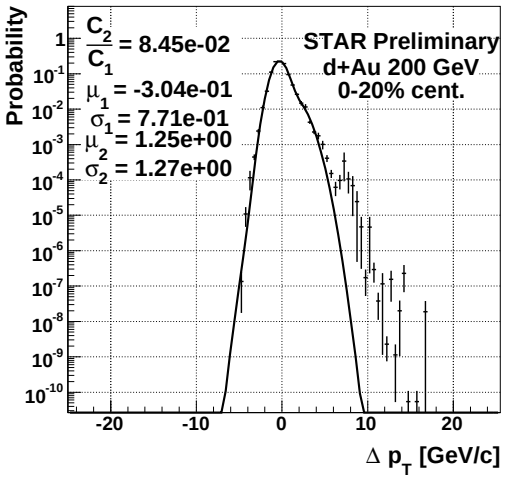

Figure 6.9: Distribution of $\Delta p_{\rm T}$ for jets with $10.3 < p_{\rm T}(PyGe) < 19.3$ GeV/c, matching condition $r < 0.2$ and $p_{\rm T}(PyBg) > 0.75\ p_{\rm T}(PyGe)$. Double Gaussian fit applied.

parameters were then varied within the ranges given by the different fit options to obtain the final systematic uncertainty on the jet $R_{\rm CP}$.

The double-Gaussian fit of $\Delta p_{\rm T}$ was done for the three centrality bins: 0-20%, 20-40%, 40-100%. Unfolding the measured $p_{\rm T}$ spectra for the background fluctuations described by the $\Delta p_{\rm T}$ distributions may introduce additional systematic uncertainties and is in fact not necessary. Instead, additional $\Delta p_{\rm T}$ smearing was applied to the $p_{\rm T}$ spectra measured for different centralities, so that the numerator and denominator in the $R_{\rm CP}$ ratio have the same level of smearing due to the background fluctuations. After this correction they are divided to obtain the final nuclear modification factor $R_{\rm CP}$. The details of this procedure are displayed in Table 6.3.

$R_{\rm CP}$	applied to numerator	applied to denominator
0-20%/40-100%	$\Delta p_{\rm T}(40-100\%)$	$\Delta p_{\rm T}(0-20\%)$
20-40%/40-100%	$\Delta p_{\rm T}(40-100\%)$	$\Delta p_{\rm T}(20-40\%)$

Table 6.3: Additional $\Delta p_{\rm T}$ smearing applied to jet $p_{\rm T}$ spectra used to construct the $R_{\rm CP}$ ratio.

The resulting $R_{\rm CP}$ coming from the "$\Delta p_{\rm T}$" correction is shown in Figure 6.10. The $p_{\rm T}$ integrated values of $R_{\rm CP}$ in intervals $9.3 < p_{\rm T} < 14.1$ GeV/c, $p_{\rm T} > 14.1$ GeV/c with statistical errors are shown in the figures. For jet $p_{\rm T} < 14.1$ GeV/c there is $\approx 40\%$ enhancement for centrality 0-20% and $\approx 20\%$ enhancement for centrality 20-40%. The systematic uncertainty due to the variation of $\Delta p_{\rm T}$ fit parame-

ters was estimated to 5%. This is more than in the case of bin-by-bin correction. On the other hand the *statistical* errors of R_{CP} are smaller: they come solely from the data, but they have a contribution from the simulation in the bin-by-bin correction.

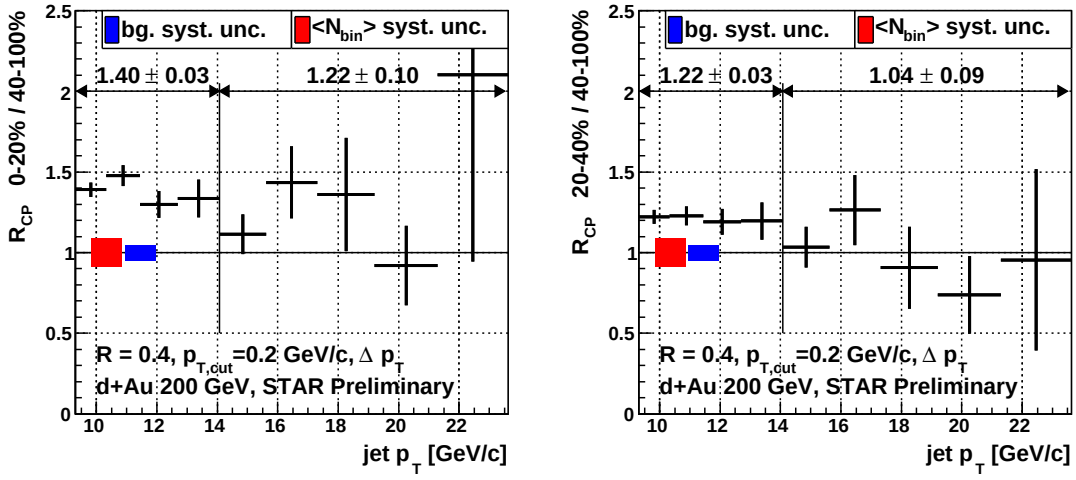

Figure 6.10: Jet R_{CP} in 200 GeV d+Au collisions obtained for two centrality bins using the Δp_{T} correction. Jet algorithm anti$-\mathrm{k_T}$ with $R = 0.4$ and $p_{\mathrm{T,cut}} = 0.2$ GeV/c was used. The p_{T} integrated R_{CP} values with statistical errors are shown in the figures.

6.3.3 Results of R_{CP} measurement at low and high jet p_{T}

Results from two different methods of correcting the background fluctuations are consistent with each other. The R_{CP} ratio is significantly above one for low p_{T} jets ($9.3 < p_{\mathrm{T}} < 11.4$ GeV/c in bin-by-bin correction and $9.3 < p_{\mathrm{T}} < 14.1$ GeV/c in Δp_{T} correction). The average [1] R_{CP} for the two centralities in the interval $9.3 < p_{\mathrm{T}} < 14.1$ GeV/c using the two methods are shown in Table 6.4. Using the Δp_{T} correction $R_{\mathrm{CP}} = 1.40 \pm 0.15$, which is a 2.7σ effect.

The integrated values of the R_{CP} for higher jet transverse momenta $p_{\mathrm{T}} > 14.1$ GeV/c are shown in Table 6.5. A slight enhancement (1.4σ) is observed for 0-20% most central collisions, while for the centrality 20-40% the R_{CP} is consistent with unity.

Two effects may contribute to the observed centrality-dependent enhancement of jet production in d+Au collisions, both of which are discussed in more detail in Section 2.5: Rescattering in nuclear matter (leading to increased jet p_{T}) and anti-shadowing. The quantitative comparison of the data to theoretical models will be done in the future.

[1] taking into account the shape of p_{T} spectrum, therefore dominated by lower p_{T} jets

centrality, p_{T} range	corr. method	$R_{\mathrm{CP}} \pm stat. \pm syst.$	syst.(bg)	syst.(cent.)
0-20% / 40-100%	bin-by-bin	$1.29 \pm 0.05 \pm 0.13$	0.06	0.12
$9.3 - 14.1$ GeV/c	Δp_{T}	$1.40 \pm 0.03 \pm 0.15$	0.07	0.13
20-40% / 40-100%	bin-by-bin	$1.17 \pm 0.05 \pm 0.10$	0.01	0.10
$9.3 - 14.1$ GeV/c	Δp_{T}	$1.22 \pm 0.03 \pm 0.13$	0.06	0.11

Table 6.4: R_{CP} for jets with $9.3 < p_{\mathrm{T}} < 14.1$ GeV/c with the values of the individual systematic uncertainties. Background (bg) systematic uncertainty is uncorrelated between the correction methods. Statistical uncertainty is partially correlated between the correction methods. Centrality (cent) systematic uncertainty is totally correlated between the correction methods.

centrality, p_{T} range	corr. method	$R_{\mathrm{CP}} \pm stat. \pm syst.$	syst.(bg)	syst.(cent.)
0-20% / 40-100%	bin-by-bin	$1.21 \pm 0.10 \pm 0.11$	0.02	0.11
$p_{\mathrm{T}} > 14.1$ GeV/c	Δp_{T}	$1.22 \pm 0.10 \pm 0.13$	0.06	0.11
20-40% / 40-100%	bin-by-bin	$1.03 \pm 0.10 \pm 0.09$	0.01	0.09
$p_{\mathrm{T}} > 14.1$ GeV/c	Δp_{T}	$1.04 \pm 0.09 \pm 0.10$	0.05	0.09

Table 6.5: R_{CP} for jets with $p_{\mathrm{T}} > 14.1$ GeV/c with the values of the individual systematic uncertainties. Background (bg) systematic uncertainty is uncorrelated between the correction methods. Statistical uncertainty is partially correlated between the correction methods. Centrality (cent) systematic uncertainty is totally correlated between the correction methods.

6.3.4 Comparison to results from PHENIX experiment

Recently the PHENIX Collaboration presented measurement of jet R_{CP} from 200 GeV d+Au collisions [144, 145]. The details of this analysis are briefly described, followed by the results. Finally a comparison to the R_{CP} measurement in this thesis is presented.

The PHENIX R_{CP} results were obtained with anti$-\mathrm{k_T}$ jet algorithm with resolution parameter $R = 0.3$ and $R = 0.5$. The PHENIX analysis uses different lower p_{T} cut on tracks and towers: $p_{\mathrm{T,cut}} = 0.4$ GeV/c (as opposed to $p_{\mathrm{T,cut}} = 0.2$ GeV/c used in STAR). PHENIX Collaboration uses jet embedding into minimum bias events and unfolding as their only correction, i.e. without event-wise background determination and subtraction. The event sample used is not minimum bias but there is a trigger requiring a high-p_{T} electron/photon with $p_{\mathrm{T}} > 1.6$ GeV/c. Also the centrality selection for the peripheral bin is different: 60-88% as opposed to 40-100% used in STAR.

The nuclear modification factor R_{CP} by the PHENIX Collaboration is shown in Figure 6.11 for $R = 0.3$ and in Figure 6.12 for $R = 0.5$. What is observed is centrality-dependent *suppression*. The jet suppression for $R = 0.3$ is almost constant with jet p_{T} and has a value of $R_{\mathrm{CP}} \approx 0.75 \pm 0.1$. The suppression is smaller for higher value of resolution parameter R. In this jet p_{T} region there may

be some effect of jet energy loss, as suggested in [70]. For the highest p_{T} there could be already some contribution of the EMC effect. Both of these may lead to the suppression observed by the PHENIX collaboration.

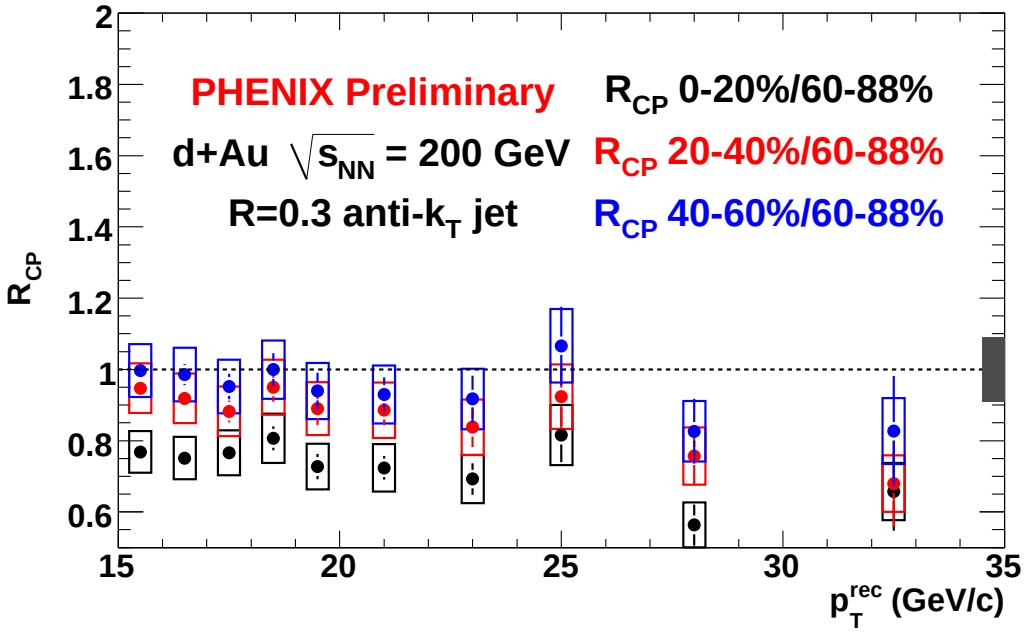

Figure 6.11: Centrality dependence of jet R_{CP} with $R = 0.3$, $p_{\mathrm{T,cut}} = 0.4$ GeV/c by the PHENIX Collaboration. Taken from [144].

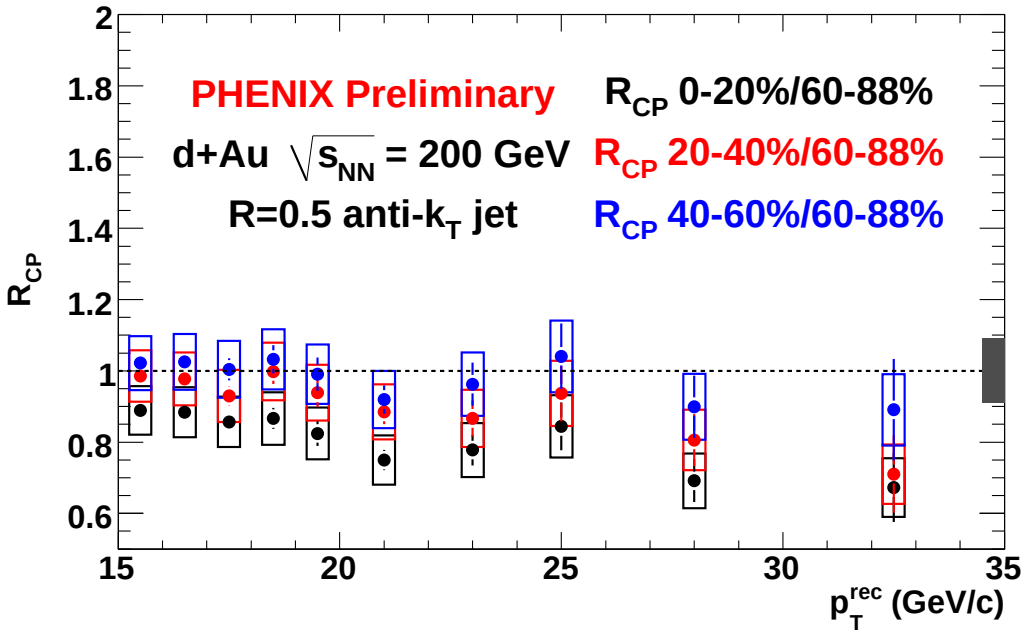

Figure 6.12: Centrality dependence of jet R_{CP} with $R = 0.5$, $p_{\mathrm{T,cut}} = 0.4$ GeV/c by the PHENIX Collaboration. Taken from [145].

To compare to results from STAR experiment it is necessary to use the same

values of R and $p_{\mathrm{T,cut}}$ for jet finding, as will be done later. The centrality selection 60-88% used by PHENIX for the peripheral bin is slightly more peripheral than 40-100%. However since the PHENIX R_{CP} 40-60%/60-88% is very close to unity no big effect of this difference is expected. Likewise, the effect of different trigger and correction for background is expected to be small for jets with $p_{\mathrm{T}} > 15$ GeV/c.

The analysis of R_{CP} at STAR data with bin-by-bin correction was run with $p_{\mathrm{T,cut}} = 0.4$ GeV/c and $R = 0.3$, $R = 0.5$ to compare to the PHENIX results. It was previously shown that the bin-by-bin correction is consistent with the Δp_{T} correction, so only the former was used for this comparison. The R_{CP} results for comparison with PHENIX are shown in Figure 6.13 ($R = 0.3$) and Figure 6.14 ($R = 0.5$).

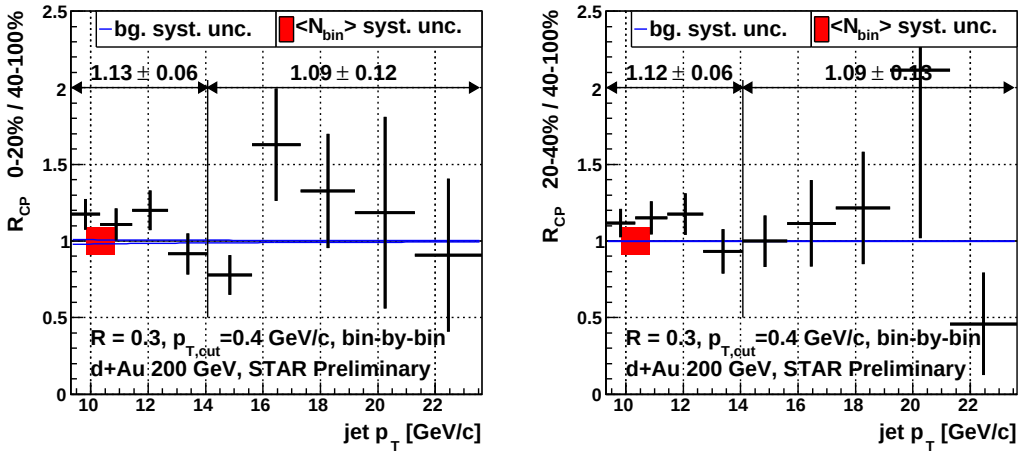

Figure 6.13: Jet R_{CP} in 200 GeV d+Au collisions with anti $-$ k$_{\mathrm{T}}$ $R = 0.3$ jet finder and $p_{\mathrm{T,cut}} = 0.4$ GeV/c, using the bin-by-bin correction. The p_{T} integrated R_{CP} values with statistical errors are shown in the figures.

The p_{T} integrated values of R_{CP} in intervals $9.3 < p_{\mathrm{T}} < 14.1$ GeV/c, $p_{\mathrm{T}} > 14.1$ GeV/c with statistical errors are shown in the figures, the systematic uncertainties are $\approx 10\%$. The R_{CP} for $R = 0.3$ is systematically above unity by $\approx 10\%$, i.e. at the edge of systematic uncertainty. For $R = 0.5$ an enhancement stronger than for the standard STAR cuts ($R = 0.4$, $p_{\mathrm{T,cut}} = 0.2$ GeV/c) is observed over the whole p_{T} range. In the p_{T} range of PHENIX measurement the STAR and PHENIX results are not consistent.

To avoid the possible effect of different centrality selection, comparison of jet p_{T} spectra in the common (0-20%, 20-40%) centrality bins should be done. This is however not possible at the moment, since the PHENIX Collaboration has not presented the fully corrected jet p_{T} spectra yet, only their R_{CP} ratios.

To confirm that the strong enhancement of jets at low p_{T} using the $R = 0.5$ parameter shown in Figure 6.14 is not an effect of uncorrected background fluctuations,

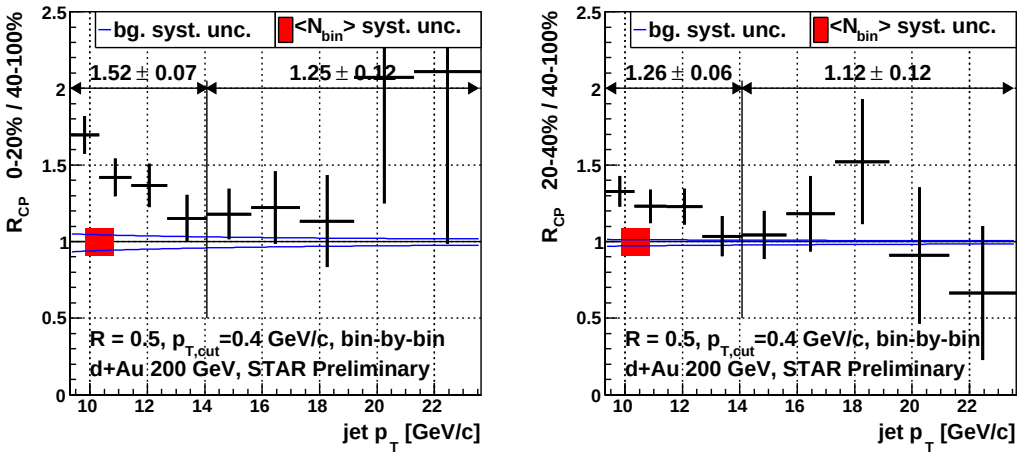

Figure 6.14: Jet R_{CP} in 200 GeV d+Au collisions with anti $-$ k$_{\mathrm{T}}$ $R = 0.5$ jet finder and $p_{\mathrm{T,cut}} = 0.4$ GeV/c, using the bin-by-bin correction. The p_{T} integrated R_{CP} values with statistical errors are shown in the figures.

a cross check was done. The dependence of R_{CP} was studied for jets with $R = 0.4$ as a function of $p_{\mathrm{T,cut}}$. If there was uncorrected effect of background fluctuations it should depend on $p_{\mathrm{T,cut}}$. In particular, for $p_{\mathrm{T,cut}} = 0.4$ GeV/c the background density ρ (defined in Eq. 5.4) is ≈ 3 times smaller than for $p_{\mathrm{T,cut}} = 0.2$ GeV/c and so should be the fluctuations. The R_{CP} for $R = 0.4$ and $p_{\mathrm{T,cut}} = 0.4$ GeV/c shown in Figure 6.15 shows results very close to those for $R = 0.4$ and $p_{\mathrm{T,cut}} = 0.2$ GeV/c in Figure 6.7. This means that the effect of strong enhancement at low p_{T} is not caused by uncorrected background fluctuations.

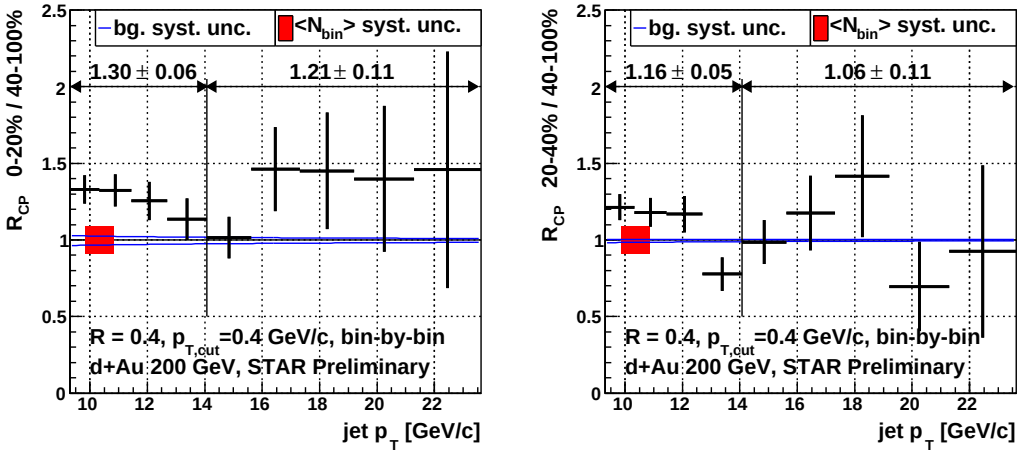

Figure 6.15: Jet R_{CP} in 200 GeV d+Au collisions with anti $-$ k$_{\mathrm{T}}$ $R = 0.4$ jet finder and $p_{\mathrm{T,cut}} = 0.4$ GeV/c, using the bin-by-bin correction. The p_{T} integrated R_{CP} values with statistical errors are shown in the figures.

Chapter 7

Di-jet measurement

The focus of the di-jet analysis is to measure the k_{T} effect and look for possible broadening in di-jet azimuthal correlations due to cold nuclear matter in d+Au collisions. Di-jet correlations are studied in $\sqrt{s_{\mathrm{NN}}} = 200$ GeV p+p and d+Au collisions from the same RHIC run (2007-2008). This has the advantage of cancellation of the systematic uncertainty due to the calibration of the BEMC calorimeter. It is also important because the BEMC is used in the trigger to enhance high p_{T} jet (and di-jet) yield.

The description of the used data and jet finder settings are presented in Section 7.1. The di-jet definition and simulation-based study of detector response and underlying event background effects are described. Results of the k_{T} measurement in p+p and 0-20% most central d+Au collisions are presented in Section 7.2. These results extend the analysis published in [146] with improved estimate of systematic uncertainties.

7.1 Data sample and cuts

To enhance the yield of rare processes (such as high-p_{T} electrons, photons and jets) in the recorded event sample, a *High Tower* ("HT") BEMC trigger was utilized in both d+Au and p+p data taking with several thresholds. The setting "HT2" used in this analysis required at least one BEMC tower with $E_{\mathrm{T}} > 4.3$ GeV to trigger the event. In addition to the High Tower condition, other components of the trigger were present, differing in the case of p+p and d+Au collisions.

The HT2 trigger condition in p+p data taking contained High Tower threshold of 4.3 GeV in addition to a coincidence of the signals in the Beam Beam Counter detectors. The event selection required the trigger tower to be marked as good (as described in Section 5.4) and this together with $|VertexZ| < 30$ cm cut and primary vertex quality cut left 837k events available for the analysis.

The HT2 trigger in d+Au data taking contained High Tower threshold of

4.3 GeV in addition to signal above threshold in the east Zero Degree Calorimeter (this condition was also a part of the minimum bias trigger used in inclusive jet analysis). The event selection required the trigger tower to be marked as good. $|VertexZ| < 30$ cm cut, primary vertex quality cut and centrality cut (0-20% most central) were applied to "HT2" triggered events, leaving 607k events available for the analysis.

The centrality definition is slightly different than the one explained in Section 5.2. The di-jet analysis was done and published [146] before the final centrality definition used for the inclusive jet measurement was available. The difference is in track cuts applied to get $mult_{FTPCE}$ and the reweighting is not applied in di-jet analysis. However, the analysis of di-jet correlations does not require absolute normalization so the sensitivity to the details of centrality determination is small. Furthermore the reweighting played only a very small role for the most central collisions as shown in Table 5.3.

The track and tower cuts and the jet finding and background subtraction procedure are very similar to the analysis of inclusive jets. The difference in the di-jet analysis is the resolution parameter for the $\mathrm{k_T}$ and $\mathrm{anti-k_T}$ algorithms: $R = 0.5$. To reduce the effect of d+Au underlying event background and thus make comparison to p+p data easier, only tracks and towers with $p_\mathrm{T} > 0.5$ GeV/c are used in the jet finding. The tracks and towers used are selected in the pseudorapidity $|\eta| < 0.9$, setting the fiducial jet acceptance to $|\eta| < 0.4$.

7.2 Measurement of k_T effect

The goal of this measurement is to obtain the Gaussian width of the k_T distribution, defined as $\sigma_{k\mathrm{T}}$ in Eq. 2.6. In each event, $\vec{k}_\mathrm{T}$ vector can be decomposed into its cylindrical components $k_{\mathrm{T},\phi}$, $k_{\mathrm{T},\eta}$, $k_{\mathrm{T},p\mathrm{T}}$ with leading jet setting the origin in azimuthal direction. The phenomenological k_T-smearing model assumes $k_{\mathrm{T},\eta} = 0$ since the Bjorken x of the scattered partons can not be measured on event basis in hadron collisions. Therefore the k_T-smearing model is in fact 2-dimensional.

Due to relatively bad jet p_T resolution the easiest way to measure $\sigma_{k\mathrm{T}}$ is to use its azimuthal projection $k_{\mathrm{T},\phi}$. Experimentally, this can be achieved by measuring:

$$k_{\mathrm{T},raw} = p_{\mathrm{T},1} \times \sin(\Delta\phi), \tag{7.1}$$

using di-jets with $p_{\mathrm{T},1} > p_{\mathrm{T},2}$ and fulfilling the condition $|\Delta\phi - \pi| < 0.524$ [1]. Gaussian fit is used to fit the $k_{\mathrm{T},raw}$ distribution to obtain its width $\sigma_{k\mathrm{T},raw}$. The non-Gaussian tails are therefore not directly accounted for, so this method is mainly sensitive to the $k_{\mathrm{T,intrinsic}} \oplus k_{\mathrm{T,soft}}$ part of the total k_T as defined in Eq. 2.7.

[1] this condition is in fact composed of two: $|\Delta\phi - \pi| < 1.0$ and $|\sin(\Delta\phi)| < 0.5$

Since only the azimuthal projection of $\vec{k}_{\mathrm{T}}$ vector is considered in Eq. 7.1, the extracted $\sigma_{k\mathrm{T},raw}$ in fact does not represent the k_{T} of the di-jet, but is factor $\sqrt{2}$ smaller. This definition will still be used since other measurements at RHIC adopted the same convention.

To select di-jet events, two highest p_{T} jets in each event were selected with $p_{\mathrm{T},1} > p_{\mathrm{T},2}$. The azimuthal correlation with respect to the "trigger" jet (the one with transverse momentum $p_{\mathrm{T},1}$) is shown in Figure 7.1 for p+p collisions and in Figure 7.2 for d+Au collisions. It can be clearly seen that a very clean di-jet signal is present for $p_{\mathrm{T},2} > 10$ GeV/c.

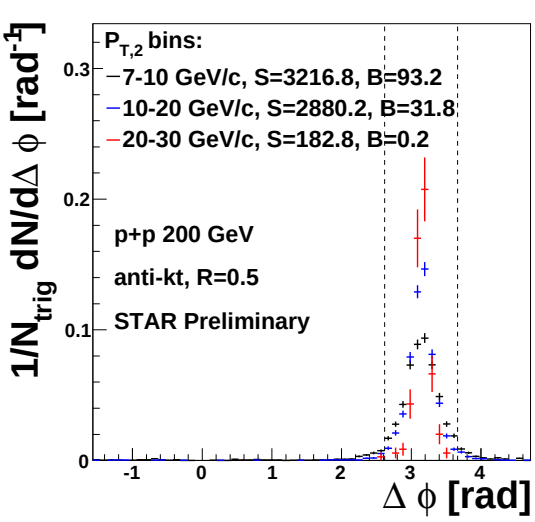

Figure 7.1: Azimuthal angle difference between the two highest p_{T} jets in p+p collision event. The vertical lines mark the di-jet selection cut $|\Delta\phi - \pi| < 0.524$.

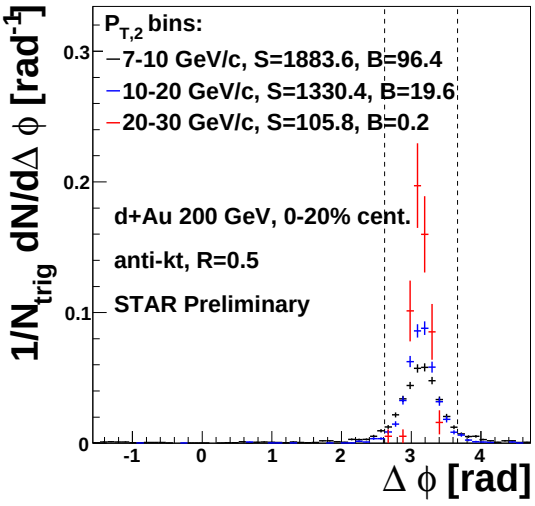

Figure 7.2: Azimuthal angle difference between the two highest p_{T} jets in 0-20% most central d+Au collision event. The vertical lines mark the di-jet selection cut $|\Delta\phi - \pi| < 0.524$.

7.2.1 Simulation

The simulation used to estimate the detector and underlying event background fluctuations effect on k_{T} measurement is the same as described in Section 5.7, except the tracking efficiency is kept at the level of the simulation. The tracking efficiency in p+p collisions is currently not known precisely, but studies of luminosity dependence of tracking efficiency in d+Au collisions and rescaling of track densities $dN_{ch}/d\eta$ from d+Au to p+p suggest it is roughly in between the ideal case and the d+Au π^+ efficiency shown in Figure 5.11. Since the same simulation is used for interpreting both p+p and d+Au data, the uncertainty of TPC tracking efficiency is larger than in inclusive jet analysis: 14%, with two equal parts of 10% (added in quadrature), one of them correlated and the other one uncorrelated between the

p+p and d+Au data sets.

The High Tower $E_{\mathrm{T}} > 4.3$ GeV (HT2) condition is required at the detector level in the simulation for all events, which highly suppresses contribution from the low pt hard bins. To estimate the effect of background fluctuations, these "triggered" events are added to real d+Au events with 0-20% centrality and minimum bias online trigger, i.e., the same online trigger as used in inclusive jet analysis. It can be seen in Figure 7.3, right, that there is a clear peaked correlation in PyBg sample without requiring any matching to jets in PyGe (which was necessary in the inclusive jet analysis). This is due to the requirement of HT2 trigger condition that highly suppresses the contribution from the low pt hard bins.

The analysis of $k_{\mathrm{T},raw} = p_{\mathrm{T},1} \times \sin(\Delta\phi)$ distributions was divided into bins of $p_{\mathrm{T},2}$: $10 < p_{\mathrm{T},2} < 20$ GeV and $20 < p_{\mathrm{T},2} < 30$ GeV/c. Since the jet energy scale in PyMC jet sample differs substantially from the one in PyGe and PyBg jet samples, the di-jet selection in PyMC is based on the value of $p_{\mathrm{T},2}$ at the detector level (PyGe) in the same event. In the case of simulation it turned out that there is a non-negligible pedestal present in $k_{\mathrm{T},raw}$ distributions, so the fit was modified to Gaussian + constant to achieve good fit quality. The distributions of $k_{\mathrm{T},raw}$ in simulation (PyMC, PyGe, PyBg) in the two $p_{\mathrm{T},2}$ bins are shown in Figure 7.3 together with the fits and the Gaussian widths.

The fits describe the $k_{\mathrm{T},raw}$ distributions in simulation relatively well. What is more important is that the shape of the distributions does not change significantly among the three jet samples. Interestingly it turns out that the σ widths are comparable within statistical errors between PyMC, PyGe and PyBg samples. This is due to interplay of jet energy scale (decrease of jet p_{T} leading to narrowing of $k_{\mathrm{T},raw}$ distribution) and jet azimuthal angle resolution (leading to broadening of $k_{\mathrm{T},raw}$ distribution). Since this agreement is actually very good, no correction to the data was made and the extracted Gaussian widths from data can be taken as a result for hadron level jets. For this reason, i.e. no correction was in fact applied, the resulting σ of the fits to data is denoted as $\sigma_{k\mathrm{T},raw}$. The systematic uncertainty on the result coming from the fact that no correction was applied is estimated 0.1 GeV/c.

7.2.2 Results

The previously described p+p and d+Au HT2-triggered data were binned in $p_{\mathrm{T},2}$ the same way as the simulation. Gaussian fits of the $k_{\mathrm{T},raw}$ distributions were performed to extract the values of $\sigma_{k\mathrm{T},raw}$. This is illustrated in Figure 7.4. It can be clearly seen that the peak in the distribution of $k_{\mathrm{T},raw}$ is narrower in p+p collisions and is not described by the Gaussian very well. Several fit ranges were used to estimate the related systematic uncertainty, to be discussed later. The χ^2/NDF values of

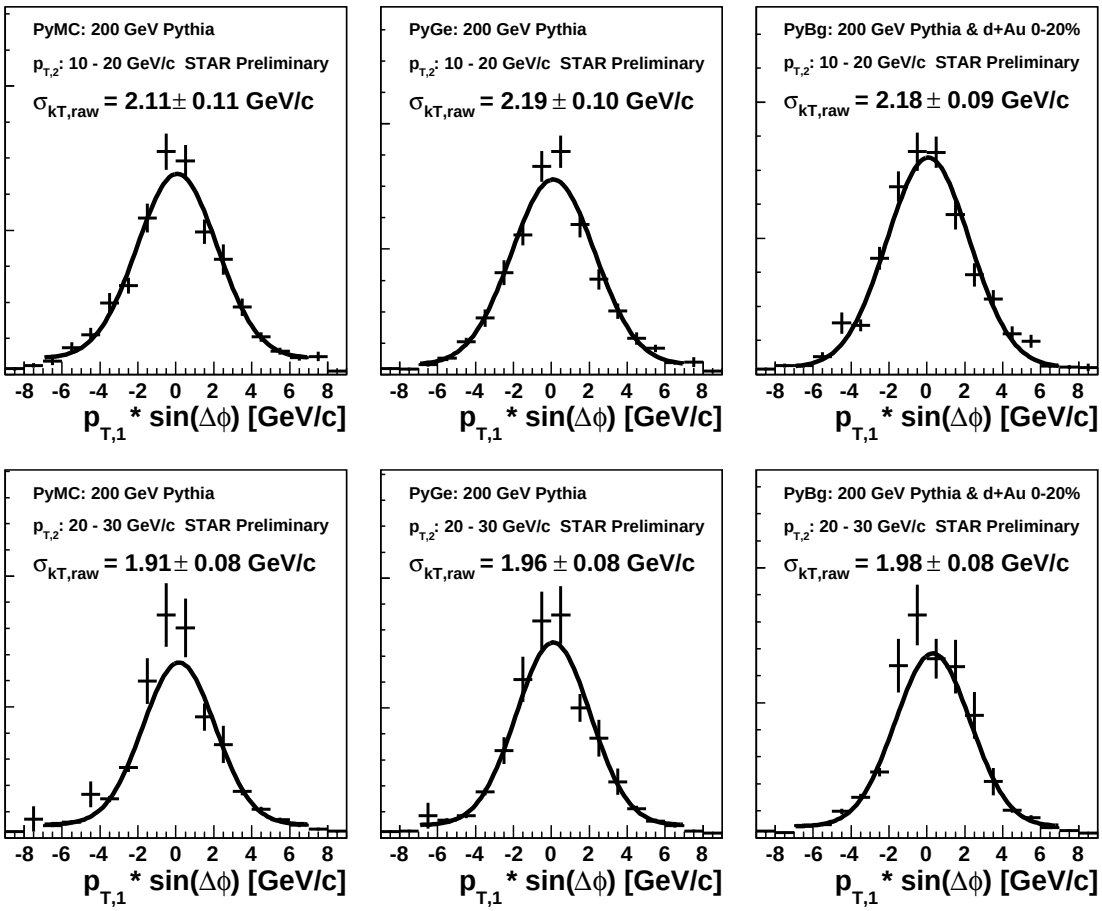

Figure 7.3: Distributions of $k_{\mathrm{T},raw}$ from simulation PyMC, PyGe and PyBg di-jet samples, using anti $-$ k$_{\mathrm{T}}$ algorithm with $R = 0.5$. The fits with constant+Gaussian function in the range $-7 < p_{\mathrm{T}} < 7$ GeV/c are shown.

the fits are shown in Table 7.1 for di-jets with $p_{\mathrm{T},2} > 10$ GeV/c.

There is a visible decrease of $\sigma_{k\mathrm{T},raw}$ with rising $p_{\mathrm{T},2}$ in Figure 7.4, which can possibly be attributed to increasing contribution of quark jets that are expected to have less radiation. The QCD process $g \to gg$ has factor 9/4 larger probability than the process $q \to qg$. The measurement of $\sigma_{k\mathrm{T},raw}$ at higher $p_{\mathrm{T},2}$ is however limited by the available di-jet statistics, so only one selection was used for the final result: $p_{\mathrm{T},2} > 10$ GeV/c.

There are several sources of systematic uncertainties affecting this measurement. The already mentioned effect coming from using the $\sigma_{k\mathrm{T},raw}$ without correction for the final result is ± 0.1 GeV/c. To account for the fact that the $k_{\mathrm{T},raw}$ distributions (especially in the case of p+p collisions) are not exactly Gaussian the default fit range $-7 < k_{\mathrm{T},raw} < 7$ GeV/c was varied between $-5 < k_{\mathrm{T},raw} < 5$ GeV/c and $-9 < k_{\mathrm{T},raw} < 9$ GeV/c and the differences of the resulting $\sigma_{k\mathrm{T},raw}$ parameters were taken as systematic uncertainties coming from the fitting.

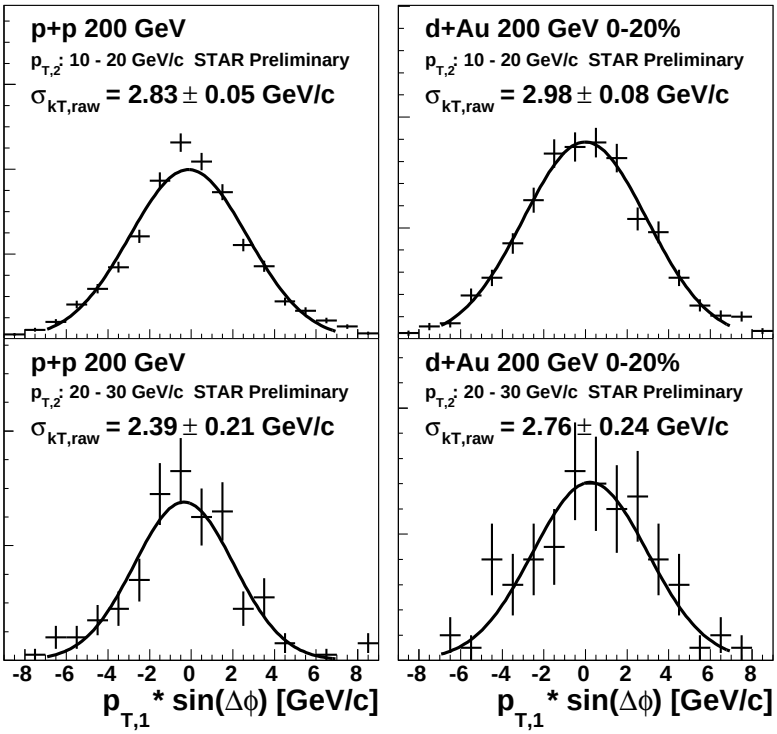

Figure 7.4: Distributions of $k_{\mathrm{T},raw}$ from p+p and d+Au data, using anti $-$ k$_{\mathrm{T}}$ algorithm with $R = 0.5$. The fits with Gaussian function in the range $-7 < p_{\mathrm{T}} < 7$ GeV/c are shown.

system	fit range [GeV/c]		
	(-5,5)	(-7,7)	(-9,9)
p+p	3.1	4.7	5.0
d+Au 0-20%	0.43	0.47	0.90

Table 7.1: The values of χ^2/NDF for the Gaussian fits to the $k_{\mathrm{T},raw}$ distributions in p+p and 0-20% most central d+Au data. For di-jets with $p_{\mathrm{T},2} > 10$ GeV/c.

The systematic uncertainties related to the jet measurement by the STAR detector are coming from the TPC tracking efficiency uncertainty of 14% and BEMC calibration uncertainty of 5%. It should be noted that the TPC tracking efficiency uncertainty is about half correlated between p+p and d+Au, whereas the BEMC calibration uncertainty is totally correlated between the two data sets since the data come from the same run and use the same calibration. The impact of these uncertainties was determined by variation of charged [2] and neutral energy fraction of jets (prior to defining di-jets) and the construction of $k_{\mathrm{T},raw}$ and fitting was repeated. The resulting fit values and the values of individual systematic uncertainties are

[2]It was determined in analysis of jet p_{T} spectra that the impact of 10% tracking efficiency uncertainty is similar to impact of 5% change of charged energy fraction in jets. Therefore the charged energy fraction of jets was changed by 7% - half of 14%.

presented in Table 7.2.

system	$\sigma_{k\mathrm{T},raw} \pm stat. \pm syst.$ [GeV/c]	systematic uncertainties [GeV/c]			
		tracking	BEMC	fit range	no-corr.
p+p	$2.80 \pm 0.05^{+0.17}_{-0.29}$	$^{+0.07}_{-0.09}$	$^{+0.04}_{-0.05}$	$^{+0.09}_{-0.25}$	± 0.1
d+Au 0-20%	$3.00 \pm 0.07^{+0.18}_{-0.15}$	$^{+0.11}_{-0.09}$	$^{+0.06}_{-0.05}$	$^{+0.09}_{-0.03}$	± 0.1

Table 7.2: The final values of $\sigma_{k\mathrm{T},raw}$ extracted from p+p and 0-20% most central d+Au collisions for di-jets with $p_{\mathrm{T},2} > 10$ GeV/c. "no-corr." denotes the uncertainty due to not correcting exactly back to hadron level jets. The "tracking" uncertainty is partially correlated and the "BEMC" uncertainty is totally correlated between the two data sets.

7.3 Summary

The final Gaussian σ widths of k_{T} distributions in $\sqrt{s_{\mathrm{NN}}} = 200$ GeV collisions for di-jets selected with $p_{\mathrm{T},1} > p_{\mathrm{T},2} > 10$ GeV/c are:

- p+p collisions: $\sigma_{k\mathrm{T},raw} = 2.80 \pm 0.05(\mathrm{stat.})^{+0.17}_{-0.29}(\mathrm{syst.})$ GeV/c
- 0-20% d+Au col.: $\sigma_{k\mathrm{T},raw} = 3.00 \pm 0.07(\mathrm{stat.})^{+0.18}_{-0.15}(\mathrm{syst.})$ GeV/c

Comparison of p+p and d+Au allows for possible broadening due to rescattering in cold nuclear matter, but the systematic uncertainties prevent us from conclusive quantification of this effect.

The measurement of $\sigma_{k\mathrm{T}}$ using di-jets can be compared to a complimentary method - so called jet-like di-hadron correlations - that is using azimuthal correlations of high-p_{T} hadrons. The highest-p_{T} hadron in the event serves as a proxy for the jet axis and is used as a trigger. Azimuthal correlations of other hadrons in the event are constructed with respect to this trigger. The method utilizes the measurement of the widths of the near-side ($\Delta\phi \approx 0$) and away-side ($\Delta\phi \approx \pi$) correlation peaks. The near-side peak width is mainly due to the j_{T}, the transverse momentum of the jet constituents with respect to the jet axis. The away-side with has an additional contribution from k_{T}. See [147] and references therein for more details on this method.

Di-hadron correlation analysis [148, 149] done by the STAR collaboration using the run 2007-2008 RHIC data has shown that there is $\approx 20\%$ broadening of k_{T} distribution from p+p to d+Au collisions. The detailed dependence of the extracted $\sqrt{\langle k_{\mathrm{T}}^2 \rangle}$ on the trigger hadron p_{T} is displayed in Figure 7.5. There is a slight rise for high trigger p_{T}, but generally the statistical precision and kinematic reach of this

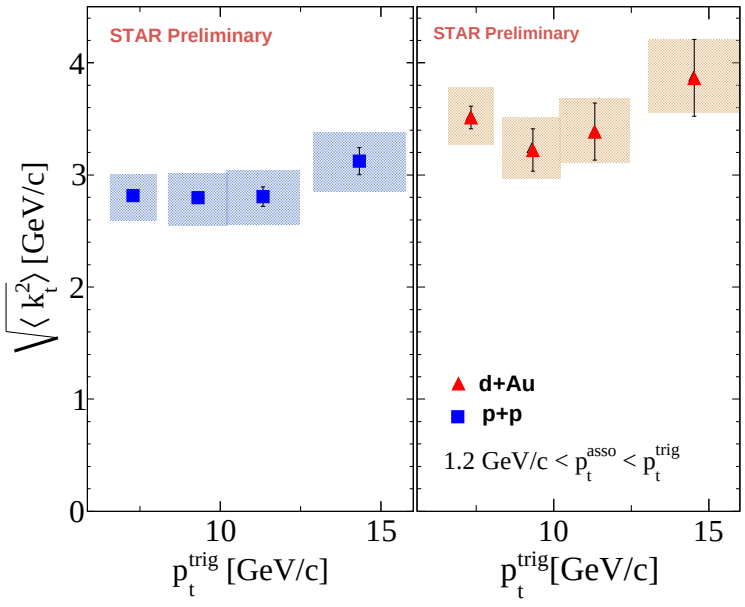

Figure 7.5: The k_{T} widths extracted by the di-hadron correlation method [148, 149] in 200 GeV p+p and d+Au collisions. Figure taken from [150].

method is worse than for the di-jet correlation method. This result is consistent with the presented result from di-jet correlations.

The di-hadron correlation method was used by the PHENIX collaboration to measure the p_{T}-integrated value of k_{T} in $\sqrt{s} = 200$ GeV p+p collisions [147]. The result is $\sqrt{\langle k_{\mathrm{T}}^2 \rangle} = 2.68 \pm 0.07(\mathrm{stat.}) \pm 0.34(\mathrm{syst.})$, which is consistent with the presented di-jet measurement.

The article [46] presents an overview of k_{T} measurements in p+p collisions in the broad range of collision energies, ranging from fixed target experiments to Tevatron energies ($\sqrt{s}$ 630 GeV and 1.8 TeV). The reported quantity is the total transverse momentum of parton *pair* (the k_{T} of di-jet) that corresponds to $\langle p_{\mathrm{T}} \rangle_{pair} = \sqrt{2}\sigma_{k\mathrm{T},raw}$. The result for the presented di-jet measurement in $\sqrt{s} = 200$ GeV p+p collisions is [3] $\langle p_{\mathrm{T}} \rangle_{pair} = 3.96^{+0.25}_{-0.41}$ GeV/c. This result is compared to other measurements of $\langle p_{\mathrm{T}} \rangle_{pair}$ in Figure 7.6. It is above the trend of di-photon data. This increase can be explained by enhanced initial and final state radiation in the di-jet case, since there is a larger contribution of gluons in the di-jet events as compared to the di-photon events. Such increase of $\langle p_{\mathrm{T}} \rangle_{pair}$ for di-jets is seen already at lower $\sqrt{s}$ where the situation is similar.

[3] the uncertainty are statistical + systematic summed in quadrature

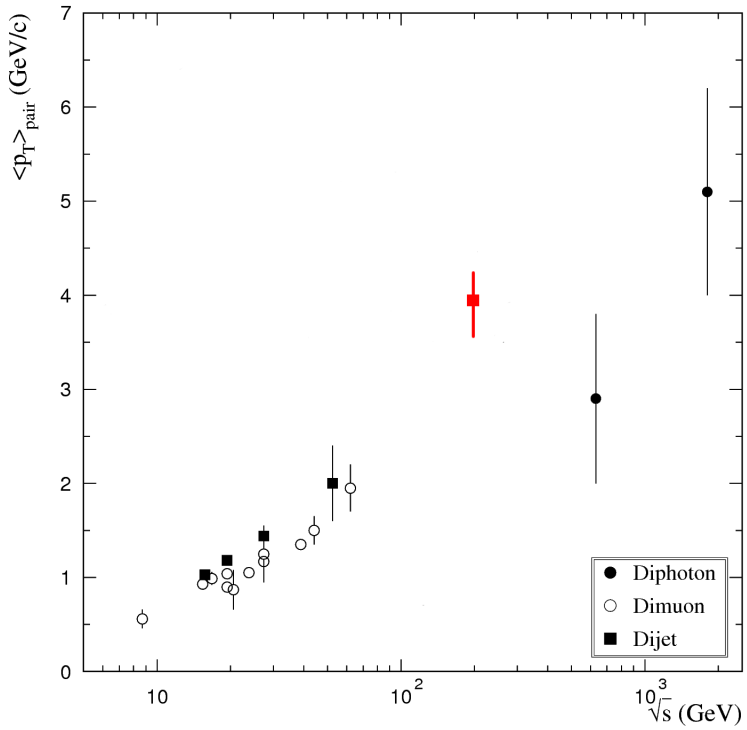

Figure 7.6: The comparison of the presented k_{T} measurement with di-jets (red square) to measurements by other experiments at different energies using di-photons, di-jets and di-muons [46]. $\langle p_{\mathrm{T}} \rangle_{pair} = \sqrt{2}\sigma_{k\mathrm{T},raw}$.

Chapter 8

Conclusions and Outlook

The goal of this work was to use the measurement of the jet production at mid-rapidity in d+Au collisions at $\sqrt{s_{\mathrm{NN}}} = 200$ GeV with the STAR detector to search for and quantify the cold nuclear matter effects. This was achieved by studying inclusive jet spectra and di-jet correlations in comparison to either p+p reference measurement or via the centrality dependence of the observed effects.

Important and interesting results on jet production in 200 GeV d+Au collisions were presented in this thesis. The jet p_{T} spectrum in d+Au collisions presented first in [140] was the first such measurement at RHIC. The presented inclusive jet p_{T} spectrum and di-jet correlation measurements in d+Au will play a crucial role in interpretation of the jet measurements in heavy-ion collisions at RHIC [78].

Apart from the main topic of this work, the author contributed to the Heavy Flavor Tracker (HFT) project described in Chapter 4. The simulations of D^0 and Λ_{C} reconstruction were among the performance studies requested for the final approval of this important upgrade of the STAR experiment. The project has passed all required steps and a partial installation of the HFT detector is planned for the RHIC summer shutdown in 2012. The studies of D^0 and Λ_{C} reconstruction with the HFT were presented in [121, 124, 126].

The jets were reconstructed from charged tracks and towers of the electromagnetic calorimeter using modern techniques of anti $-$ $\mathrm{k_T}$ jet algorithm with a novel method of underlying background subtraction based on active jet areas and event-by-event background density determination. The jet reconstruction performance was evaluated using a PYTHIA simulated jet events with GEANT-based detector response simulation. The residual background effects (background fluctuations) were studied and corrected for using the mixed events from PYTHIA and real d+Au collision background.

The inclusive jet p_{T} spectrum in pseudorapidity $|\eta| < 0.55$ from 0-20% most central collisions was measured in the range of $9.3 < p_{\mathrm{T}} < 32.2$ GeV/c and compared to measurements of jet p_{T} spectra in p+p collisions. These results were reported

also in [151, 152]. Within the systematic uncertainties of these measurements, the jet production in d+Au collisions is consistent with binary collision scaled p+p collisions. The comparison uncertainty is dominated by systematic errors of the reference measurements in p+p collisions.

The centrality dependence of jet production in d+Au collisions was studied via the measurement of jet nuclear modification factor R_{CP}. This measurement was performed for two centralities: 0-20% and 20-40% most central collisions in comparison to peripheral collisions (centrality 40-100%). Two methods differing in the treatment of background fluctuations were used: bin-by-bin correction and Δp_{T} correction. The resulting R_{CP} for the most central collisions (0-20% / 40-100%) in the jet p_{T} range $9.3 < p_{\mathrm{T}} < 14.1$ GeV/c has the value:

- $R_{\mathrm{CP}} = 1.29 \pm 0.05(\mathrm{stat.}) \pm 0.14(\mathrm{syst.})$ using bin-by-bin correction
- $R_{\mathrm{CP}} = 1.40 \pm 0.03(\mathrm{stat.}) \pm 0.12(\mathrm{syst.})$ using Δp_{T} correction

At higher jet transverse momenta $p_{\mathrm{T}} > 14.1$ GeV/c the presented results show a slight (20% or 1.4σ) enhancement of jet production in 0-20% most central collisions. These observations may be explained by rescattering in cold nuclear matter and by nuclear modification of parton distribution functions (anti-shadowing).

A similar measurement was performed by the PHENIX Collaboration, showing $\approx 10 - 20\%$ suppression for jet $p_{\mathrm{T}} > 15$ GeV/c in 0-20% most central collisions. To compare to these measurements the presented R_{CP} analysis was rerun with the same jet finder parameters (resolution parameter R and particle p_{T} cut $p_{\mathrm{T,cut}}$) as used by PHENIX. The results are however inconsistent: STAR result is showing $\approx 10 - 25\%$ enhancement of jet production for jet $p_{\mathrm{T}} > 14.1$ GeV/c in 0-20% most central collisions. The comparison of the jet spectra between STAR and PHENIX experiments has to be done to find the source of the discrepancy. This will be possible when the fully corrected jet p_{T} spectrum from the PHENIX collaboration is available.

The study of di-jets in 0-20% most central d+Au collisions and in p+p collisions at $\sqrt{s_{\mathrm{NN}}} = 200$ GeV [146, 153] aims at observation of k_{T} broadening due to cold nuclear matter effects. The following values of the k_{T} Gaussian sigma widths were measured using di-jets with $p_{\mathrm{T},1} > p_{\mathrm{T},2} > 10$ GeV/c:

- p+p collisions: $\sigma_{k\mathrm{T},raw} = 2.80 \pm 0.05(\mathrm{stat.})^{+0.17}_{-0.29}(\mathrm{syst.})$ GeV/c
- 0-20% d+Au col.: $\sigma_{k\mathrm{T},raw} = 3.00 \pm 0.07(\mathrm{stat.})^{+0.18}_{-0.15}(\mathrm{syst.})$ GeV/c

The measurement is compatible with a slight broadening from p+p to central d+Au collisions due to cold nuclear matter effects. This observation is consistent

with the preliminary results of a di-hadron measurement by the STAR Collaboration. The measurement of k_{T} in p+p collisions at $\sqrt{s} = 200$ GeV using di-jets is compared to measurements at different collision energies with di-jets, di-photons and di-muons. The value of $\sigma_{k\mathrm{T},raw}$ in p+p collisions is consistent with measurement by the PHENIX Collaboration using the di-hadron correlation technique.

There are several steps planned to further improve the existing results. One of them is a more realistic simulation of jet reconstruction in d+Au collisions with run 8 detector backgrounds to decrease the systematic uncertainties related to detector performance. To measure the jet nuclear modification factor with p+p collisions as reference (R_{dAu}), it will be necessary to extract and fully correct the inclusive jet p_{T} spectrum from run 8 p+p collisions. This will cancel out most of the remaining detector-related systematic uncertainties.

Appendix A

Glauber modeling in high energy nuclear collisions

Glauber modeling is used in nuclear (A+B) collisions to calculate the mean number of participants $\langle N_{part} \rangle$ and binary collisions $\langle N_{bin} \rangle$ as a function of collision centrality determined by impact parameter b. Participant is a nucleon that undergoes at least one (inelastic) collision. The basic ingredients of Glauber model [154, 53] are:

- a characteristic nucleon-nucleon (n-n) cross section
- straight line trajectories of the colliding nucleons

In other words, the complex A+B collision is treated as superposition of many n-n collisions with all nucleons traveling on constant trajectories. Spatial distribution of nucleons within nuclei A, B and n-n cross section are inputs to the model. Technically, the model uses eikonal approximation to multi-particle scattering problem, which is related to the assumption of straight-line nucleon trajectories. The eikonal approximation may be used to calculate the phase shifts for individual scatterings and relate them to the total cross section via optical theorem.

The organization and several parts of this Appendix are adopted from the article [130] which describes the Glauber model implementation for RHIC collisions.

A.1 Representation of nuclei

The most common representation of (near) spherical nuclei such as Au is the Woods-Saxon form with the nucleon density as a function of distance from the center r:

$$\rho(r) = \frac{\rho_0}{1 + \exp(\frac{r - r_0}{c})}, \tag{A.1}$$

with the parameter values for Au nucleus: $r_0 = 6.5$ fm (radius), $c = 0.535$ fm (skin depth) and $\rho_0 = 0.17$ nucleons/fm^3 (nucleon density).

For the description of the deuteron nucleus, the Hulthen form [129] of the wave function is used at RHIC:

$$\phi(r_{pn}) = \frac{1}{2\pi}\frac{\sqrt{ab(a+b)}}{b-a}\frac{e^{-ar_{pn}} - e^{-br_{pn}}}{r_{pn}}, \tag{A.2}$$

where r_{pn} is proton-neutron distance and the following parameter values were used: $a = 0.228$ fm^{-1}, $b = 1.18$ fm^{-1}. The probability for given r_{pn} is then given by:

$$p(r_{pn}) = 4\pi r^2 \phi^2(r_{pn}). \tag{A.3}$$

These nuclear density profiles are shown in Figure A.1.

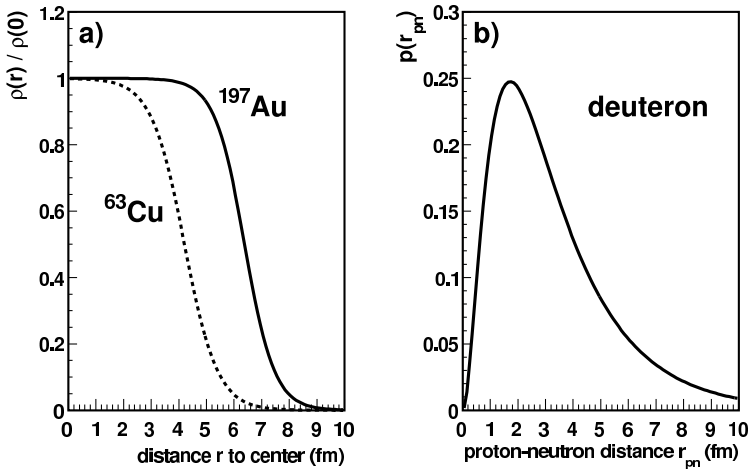

Figure A.1: Nuclear density profiles: Woods-Saxon for Cu, Au (a) and Hulthen for deuteron (b). Figure from [130].

A.2 Optical Glauber model

With two nuclei A, B colliding with impact parameter $\vec{b}$ as shown in Figure A.2, consider the "flux tubes" (along the z direction/beam axis) with displacement $\vec{s}$ from the center of nucleus A and $\vec{s} - \vec{b}$ from the center of the nucleus B. Nucleus A has A nucleons, nucleus B has B nucleons. During the collision, the nucleons in these flux tubes overlap. The probability per unit transverse area of a given nucleon being located in the target flux tube is $T_A(\vec{s}) = \int \rho_A(\vec{s}, z_A) dz_A$, where $\rho_A(\vec{s}, z_A)$ is per volume probability (normalized to unity) of locating nucleon in target nucleus A. Constructing the same quantity for nucleus B, the so-called thickness function $T_{AB}(\vec{b})$ can be calculated as:

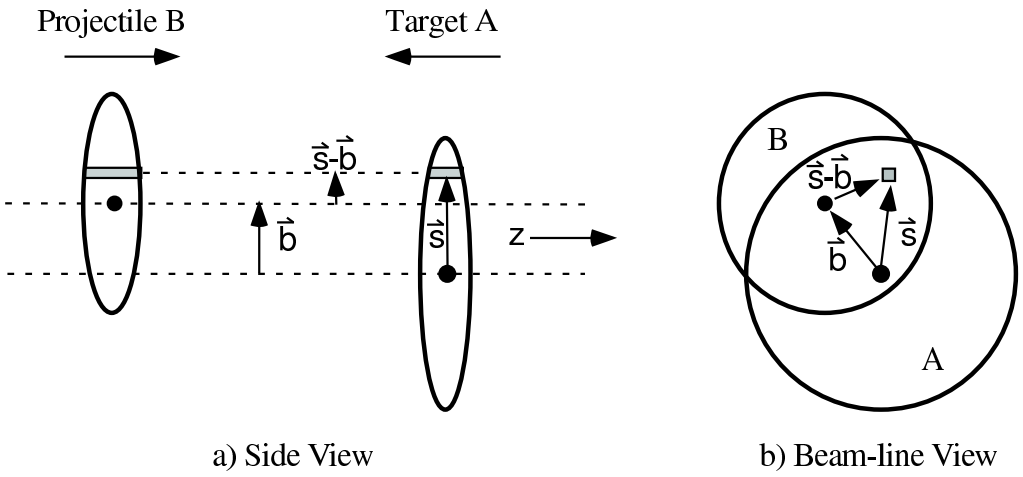

Figure A.2: Illustration of nucleus-nucleus collision with impact parameter $\vec{b}$. Figure from [130].

$$T_{AB}(\vec{b}) = \int T_A(\vec{s}) T_B(\vec{s} - \vec{b}) d^2\vec{s}. \tag{A.4}$$

The probability of inelastic interaction of given nucleon-nucleon pair is then $T_{AB}(\vec{b})\sigma_{\text{inel}}$, where σ_{inel} is the nucleon-nucleon inelastic cross section, $\sigma_{\text{inel}} = 42$ mb at $\sqrt{s_{\text{NN}}} = 200$ GeV. The vector impact parameter $\vec{b}$ can be replaced by scalar b if the nuclei are not polarized. The probability of n nucleon-nucleon interactions between nuclei A, B is then obtained via binomial distribution:

$$P(n, b) = \binom{AB}{n} \left[T_{AB}(b)\, \sigma_{\text{inel}}\right]^n \left[1 - T_{AB}(b)\, \sigma_{\text{inel}}\right]^{AB-n} \tag{A.5}$$

The total inelastic cross section of the A+B collision can be obtained by summing the b-dependent binomial probability for $n > 0$ and integrating over impact parameter space:

$$\sigma_{\text{inel}}^{\text{A+B}} = \int_0^\infty 2\pi b db \left\{1 - \left[1 - T_{AB}(b)\, \sigma_{\text{inel}}\right]^{AB}\right\} \tag{A.6}$$

The number of binary nucleon-nucleon collisions is:

$$\langle N_{bin} \rangle (b) = \sum_{n=1}^{AB} nP(n, b) = ABT_{AB}(b)\, \sigma_{\text{inel}}^{\text{NN}} \tag{A.7}$$

and the number of nucleons from nucleus A participating in at least one collision (called participants or wounded nucleons) is:

$$N_{\text{part}}^{\text{A}}(b) = A \int T_A(s) \left\{1 - \left[1 - T_B\left(|\vec{s} - \vec{b}|\right) \sigma_{\text{inel}}\right]^B\right\} d^2\vec{s}, \tag{A.8}$$

with the analogical expression holding for participants from the nucleus B.

A.3 Glauber Monte Carlo modeling

The Glauber Monte Carlo (MC) approach generates positions of the nucleons in the incoming nuclei by sampling the nuclear density profiles, keeping the nucleon-nucleon distance $d > d_{min} = 0.4$ fm, which is the characteristic length of the nucleon-nucleon repulsive potential. Using the "black-disk" nucleon-nucleon overlap function, a given pair of nucleons of incoming nuclei A, B undergoes an inelastic collision if their distance is:

$$d < \sqrt{\frac{\sigma_{inel}}{\pi}}. \tag{A.9}$$

This way, $N_{\rm bin}$ and $N_{\rm part}$ are determined for given simulated collision.

The main difference between the two approaches is the fact that optical Glauber model uses smooth distributions of nuclear density profiles. It does not consider individual nucleons with given positions. This brings some small discrepancies between the two approaches especially in collisions with large impact parameters and/or small A, B. That is, in the cases where local fluctuations of the nucleon density may become important. As a result, the optical Glauber model gives higher values of cross-section as shown in Figure A.3.

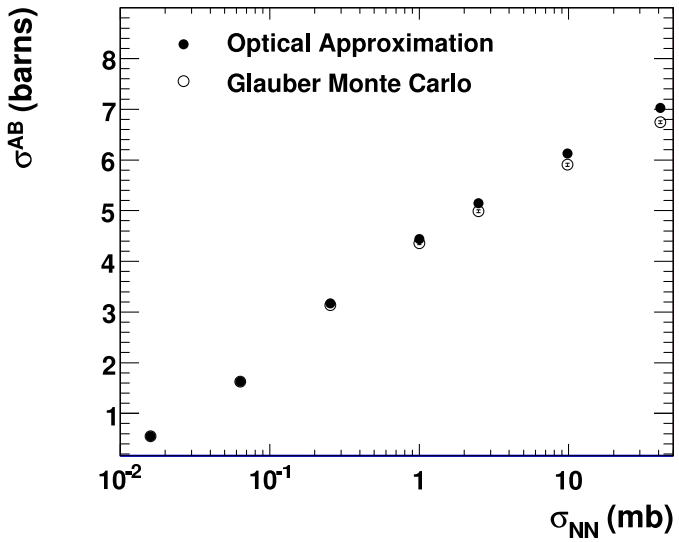

Figure A.3: Total nucleus-nucleus inelastic cross-section calculated with optical and MC Glauber models as a function of nucleon-nucleon cross section $\sigma_{\rm NN}$. Figure from [130].

Figure A.4 shows the expected linear rise of cross section as a function of impact

parameter for various collision systems. It can be observed, that the optical Glauber model gives higher cross section in the peripheral collisions (large b). That is, in the region of smaller nucleon densities where the nucleon density fluctuations become important. Figure A.5 shows impact parameter dependence of N_{bin} (marked N_{coll} in the figure) and N_{part} for Au+Au collisions at $\sqrt{s_{\mathrm{NN}}} = 200$ GeV.

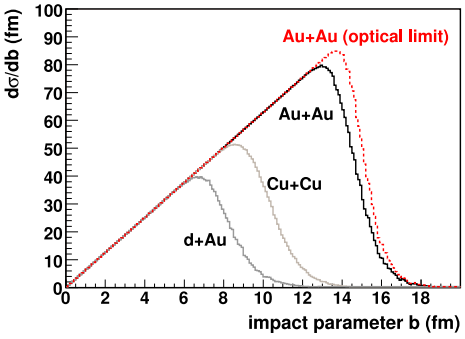

Figure A.4: Cross sections (inelastic) as function of impact parameter for various collision systems (MC Glauber), compared to optical Glauber calculation for Au+Au. Figure from [130].

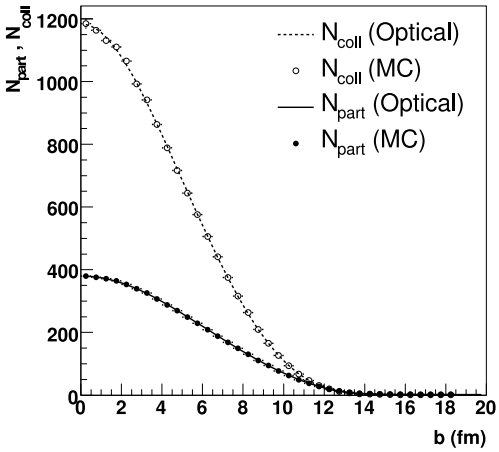

Figure A.5: Number of participants N_{part} and binary collisions N_{coll} (denoted N_{bin} in the main text) as function of impact parameter. Figure from [130].

A.4 Multiplicity distributions

It is necessary to relate the quantities obtained with the Glauber modeling to the experimental observables. There are two ways to measure the collision centrality: measuring the participant neutrons with the zero degree calorimeter or measuring the particles from the collisions of the participant nucleons. The most common way to experimentally determine centrality is via the measurement of particle multiplicity (i.e., the latter option).

An assumption for this method is monotonous dependence of particle multiplicity in certain phase space on centrality, i.e. multiplicity is higher for more central (small impact parameter) collisions. This is fulfilled in all known particle production models. Usually the measured value of multiplicity is not the total multiplicity, but rather a multiplicity density ($dN_{\mathrm{ch}}/d\eta$) in certain acceptance. Since this value is measured on event basis, the notation used will be dN/dN_{ch} to avoid confusion with measurements of pseudorapidity dependence of multiplicity $dN_{\mathrm{ch}}/d\eta$.

Having measured the multiplicity distribution in data dN/dN_{ch}, the quantiles of

this distribution are used to define centrality as illustrated in Figure A.6 for 200 GeV Au+Au collisions at RHIC. If the trigger efficiency depends on N_{ch}, some additional corrections have to be applied. To calculate the mean numbers of binary collisions, participants and impact parameter for the centrality quantiles, two approaches are used.

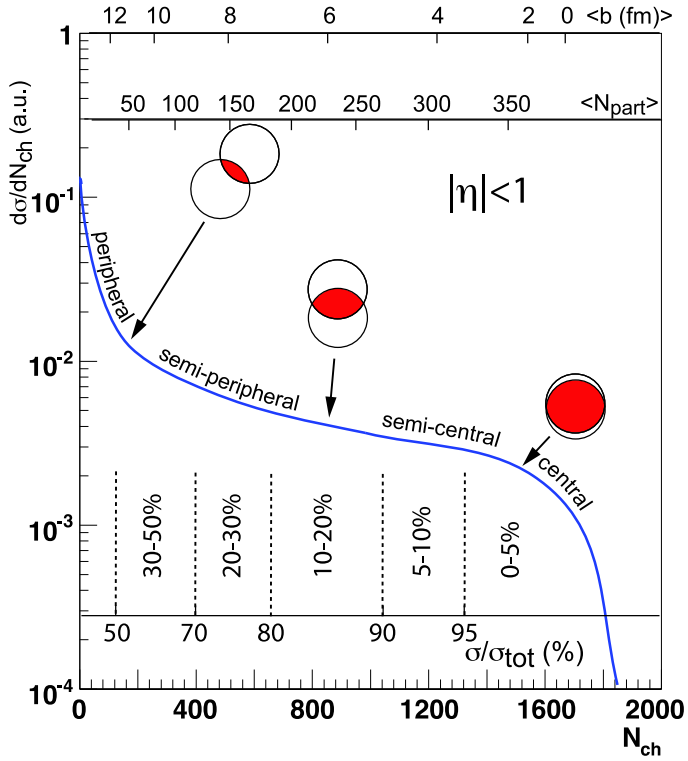

Figure A.6: Correlation of the measured multiplicity N_{ch} with the parameters from Glauber MC simulation for 200 GeV Au+Au collision. The plotted values are illustrative, not actual values used in physics analyses. Figure from [130].

With a particular model of particle production, the multiplicity distribution dN/dN_{ch} can be simulated in Glauber MC. Then the quantiles of simulated multiplicity distribution are defined and $\langle N_{bin} \rangle$, $\langle N_{part} \rangle$ and $\langle b \rangle$ are determined for events in particular centrality classes. The values of parameters in the particle production model may be taken from an external multiplicity measurement or obtained via fitting the simulated multiplicity distribution to the measured one.

To simulate the multiplicity in A+B collision, two ingredients are needed: multiplicity distribution for nucleon-nucleon distribution and how this scales in nuclear collisions (i.e., the dependence on N_{part} or N_{bin}). Multiplicity distributions in p+p collisions were measured by the UA5 experiment [131] and they are well described by the Negative Binomial Distribution (NBD). The probability of a collision with multiplicity n is:

$$P_{\mu,k}(n) = \frac{\Gamma(n+k)}{\Gamma(n+1)\Gamma(k)} \cdot \frac{(\mu/k)^n}{(\mu/k+1)^{n+k}}, \tag{A.10}$$

where parameter μ is the mean multiplicity and parameter k controls the shape of the distribution (for $k \to \infty$ the distribution becomes Poisson).

The model of multiplicity scaling presented in [155], the "wounded nucleon" model, assumes the total multiplicity scaling with number of participants (i.e., wounded nucleons):

$$dN/dN_{\mathrm{ch}} = n_{pp} N_{\mathrm{part}}, \tag{A.11}$$

where n_{pp} is multiplicity distribution in p+p collisions. This model is successfully used for d+Au collisions at RHIC, but deviates from the measured dN/dN_{ch} distributions in Au+Au collisions.

The two-component model [156] sums the contributions from hard ($\langle N_{bin} \rangle$ scaling) and soft ($\langle N_{part} \rangle$ scaling) collisions to the total multiplicity. The hard processes have very short characteristic time scales $\tau \propto 1/p_{\mathrm{T}}$ compared to the distance between individual collisions encountered by a given nucleon. Therefore these processes can be incoherently summed over the binary nucleon-nucleon collisions, hence the $\langle N_{bin} \rangle$ scaling. The following formula is then used for the multiplicity of nuclear collision:

$$dN/dN_{\mathrm{ch}} = n_{pp} \left[(1-x) N_{\mathrm{part}} + x N_{\mathrm{bin}} \right], \tag{A.12}$$

where n_{pp} is multiplicity distribution in p+p collisions and x is the fraction of hard component. The value of $x \approx 0.10$ describes well RHIC data. A very small dependence of x on collision energy makes it however questionable if the parameter x is really related to hard particle production (that should increase at higher collision energy) [130]. This should therefore be taken more as a phenomenological model.

In Au+Au collisions at STAR the centrality definition turned out to be only very little sensitive to the details of particle production models and therefore the dN/dN_{ch} is not simulated. Instead the distributions $d\sigma/dN_{\mathrm{part}}$ and $d\sigma/dN_{\mathrm{bin}}$ are used directly to define the centrality quantiles in the Glauber MC [130].

Bibliography

[1] J. Adams *et al.*, (STAR Collaboration), "Experimental and theoretical challenges in the search for the quark gluon plasma: The star collaboration's critical assessment of the evidence from rhic collisions," *Nucl. Phys.* **A757** (2005) 102–183, nucl-ex/0501009.

[2] J. Adams *et al.*, (STAR Collaboration), "Transverse momentum and collision energy dependence of high p(T) hadron suppression in Au+Au collisions at ultrarelativistic energies," *Phys.Rev.Lett.* **91** (2003) 172302, arXiv:nucl-ex/0305015 [nucl-ex].

[3] C. Adler *et al.*, (STAR Collaboration), "Disappearance of back-to-back high p(T) hadron correlations in central Au+Au collisions at s(NN)**(1/2) = 200-GeV," *Phys. Rev. Lett.* **90** (2003) 082302, arXiv:nucl-ex/0210033.

[4] J. Adams *et al.*, (STAR Collaboration), "Evidence from d + Au measurements for final state suppression of high p(T) hadrons in Au+Au collisions at RHIC," *Phys.Rev.Lett.* **91** (2003) 072304, arXiv:nucl-ex/0306024 [nucl-ex].

[5] T. Renk, "Angular variation of hard back-to-back hadron suppression in heavy-ion collisions," *Phys. Rev.* **C78** (2008) 034904, arXiv:0803.0218 [hep-ph].

[6] E. Rutherford, "The scattering of α and β particles by matter and the structure of the atom," *Phil. Mag.* **21** (1911) 669–688.

[7] C. D. Anderson, "THE POSITIVE ELECTRON," *Phys. Rev.* **43** (1933) 491–494.

[8] J. Chadwick, "POSSIBLE EXISTENCE OF A NEUTRON," *Nature* **129** (1932) 312.

[9] V. E. Barnes *et al.*, "Observation of a Hyperon with Strangeness -3," *Phys. Rev. Lett.* **12** (1964) 204–206.

[10] M. Gell-Mann, "Symmetries of baryons and mesons," *Phys. Rev.* **125** (1962) 1067–1084.

[11] M. Gell-Mann, "The Eightfold Way: A Theory of strong interaction symmetry,". CTSL-20.

[12] A. N. et al. (Particle Data Group) *Physics Letters* **B667** (2008) 1.

[13] R. Brandelik *et al.*, (TASSO Collaboration), "Evidence for Planar Events in e+ e- Annihilation at High- Energies," *Phys. Lett.* **B86** (1979) 243.

[14] J. Chýla, "Quarks, partons and Quantum Chromodynamics,". `http://www-hep.fzu.cz/Theory/notes/text.pdf`.

[15] D. J. Gross and F. Wilczek, "ULTRAVIOLET BEHAVIOR OF NON-ABELIAN GAUGE THEORIES," *Phys. Rev. Lett.* **30** (1973) 1343–1346.

[16] H. D. Politzer, "RELIABLE PERTURBATIVE RESULTS FOR STRONG INTERACTIONS?," *Phys. Rev. Lett.* **30** (1973) 1346–1349.

[17] S. Bethke, "Experimental Tests of Asymptotic Freedom," *Prog. Part. Nucl. Phys.* **58** (2007) 351–386, `arXiv:hep-ex/0606035`.

[18] B. Z. Kopeliovich and A. H. Rezaeian, "Applied QCD," `arXiv:0811.2024 [hep-ph]`.

[19] H. Caines, (STAR Collaboration), "Jet and underlying event measurements in p + p collisions at RHIC," *Nucl.Phys.* **A855** (2011) 376–379.

[20] B. I. Abelev *et al.*, (STAR Collaboration), "Longitudinal double-spin asymmetry and cross section for inclusive jet production in polarized proton collisions at s**(1/2) = 200-GeV," *Phys. Rev. Lett.* **97** (2006) 252001, `arXiv:hep-ex/0608030`.

[21] B. Jager, M. Stratmann, and W. Vogelsang, "Single inclusive jet production in polarized p p collisions at O(alpha**3(s))," *Phys. Rev.* **D70** (2004) 034010, `arXiv:hep-ph/0404057`.

[22] J. Adams *et al.*, (STAR Collaboration), "Identified hadron spectra at large transverse momentum in p + p and d + Au collisions at s(NN)**(1/2) = 200-GeV," *Phys. Lett.* **B637** (2006) 161–169, `arXiv:nucl-ex/0601033`.

[23] V. N. Gribov and L. N. Lipatov, "Deep inelastic e p scattering in perturbation theory," *Sov. J. Nucl. Phys.* **15** (1972) 438–450.

[24] G. Altarelli and G. Parisi, "Asymptotic Freedom in Parton Language," *Nucl. Phys.* **B126** (1977) 298.

[25] Y. L. Dokshitzer, "Calculation of the Structure Functions for Deep Inelastic Scattering and e+ e- Annihilation by Perturbation Theory in Quantum Chromodynamics," *Sov. Phys. JETP* **46** (1977) 641–653.

[26] S. Kretzer, H. L. Lai, F. I. Olness, and W. K. Tung, "CTEQ6 parton distributions with heavy quark mass effects," *Phys. Rev.* **D69** (2004) 114005, arXiv:hep-ph/0307022.

[27] A. D. Martin, R. G. Roberts, W. J. Stirling, and R. S. Thorne, "Parton distributions incorporating QED contributions," *Eur. Phys. J.* **C39** (2005) 155–161, arXiv:hep-ph/0411040.

[28] M. Gluck, E. Reya, and A. Vogt, "Dynamical parton distributions revisited," *Eur. Phys. J.* **C5** (1998) 461–470, arXiv:hep-ph/9806404.

[29] T. Sjostrand *et al.*, "High-energy physics event generation with PYTHIA 6.1," *Comput. Phys. Commun.* **135** (2001) 238–259, arXiv:hep-ph/0010017.

[30] T. Kinoshita, "Mass singularities of Feynman amplitudes," *J. Math. Phys.* **3** (1962) 650–677.

[31] T. D. Lee and M. Nauenberg, "Degenerate Systems and Mass Singularities," *Phys. Rev.* **133** (1964) B1549–B1562.

[32] G. F. Sterman and S. Weinberg, "Jets from Quantum Chromodynamics," *Phys. Rev. Lett.* **39** (1977) 1436.

[33] D. de Florian and W. Vogelsang, "Resummed cross-section for jet production at hadron colliders," *Phys. Rev.* **D76** (2007) 074031, arXiv:0704.1677 [hep-ph].

[34] G. C. Blazey *et al.*, "Run II jet physics," arXiv:hep-ex/0005012.

[35] G. P. Salam and G. Soyez, "A Practical Seedless Infrared-Safe Cone jet algorithm," *JHEP* **0705** (2007) 086, arXiv:0704.0292 [hep-ph].

[36] J. Pumplin *et al.*, "New generation of parton distributions with uncertainties from global QCD analysis," *JHEP* **07** (2002) 012, arXiv:hep-ph/0201195.

[37] C. F. Berger, T. Kucs, and G. F. Sterman, "Event shape / energy flow correlations," *Phys. Rev.* **D68** (2003) 014012, arXiv:hep-ph/0303051.

[38] Y.-S. Lai and B. A. Cole, "Jet reconstruction in hadronic collisions by Gaussian filtering," arXiv:0806.1499 [nucl-ex].

[39] Y.-S. Lai, (PHENIX Collaboration), "Direct jet reconstruction in p + p and Cu + Cu at PHENIX," arXiv:0911.3399 [nucl-ex].

[40] M. Cacciari and G. P. Salam, "Dispelling the N^3 myth for the k_t jet-finder," *Phys. Lett.* **B641** (2006) 57–61, arXiv:hep-ph/0512210.

[41] S. D. Ellis and D. E. Soper, "Successive combination jet algorithm for hadron collisions," *Phys.Rev.* **D48** (1993) 3160–3166, arXiv:hep-ph/9305266 [hep-ph].

[42] Y. L. Dokshitzer, G. Leder, S. Moretti, and B. Webber, "Better jet clustering algorithms," *JHEP* **9708** (1997) 001, arXiv:hep-ph/9707323 [hep-ph].

[43] M. Cacciari, G. P. Salam, and G. Soyez, "The anti-k_t jet clustering algorithm," *JHEP* **04** (2008) 063, arXiv:0802.1189 [hep-ph].

[44] M. Cacciari, G. P. Salam, and G. Soyez, "The Catchment Area of Jets," *JHEP* **04** (2008) 005, arXiv:0802.1188 [hep-ph].

[45] R. P. Feynman, R. D. Field, and G. C. Fox, "Quantum-chromodynamic approach for the large-transverse- momentum production of particles and jets," *Phys. Rev.* **D18** (1978) 3320.

[46] L. Apanasevich, C. Balazs, C. Bromberg, J. Huston, A. Maul, *et al.*, "k_T effects in direct photon production," *Phys.Rev.* **D59** (1999) 074007, arXiv:hep-ph/9808467 [hep-ph].

[47] L. Kluberg *et al.*, "Atomic Number Dependence of Large Transverse Momentum Hadron Production by Protons," *Phys. Rev. Lett.* **38** (1977) 670–673.

[48] E. V. Shuryak, "Quantum Chromodynamics and the Theory of Superdense Matter," *Phys. Rept.* **61** (1980) 71–158.

[49] F. E. Close, J.-w. Qiu, and R. G. Roberts, "QCD parton recombination and applications to nuclear structure functions," *Phys. Rev.* **D40** (1989) 2820.

[50] J. J. Aubert *et al.*, (European Muon Collaboration), "The Ratio of the Nucleon Structure Functions f2 (n) for Iron and Deuterium," *Phys. Lett.* **B123** (1983) 275.

[51] K. J. Eskola, H. Paukkunen, and C. A. Salgado, "An improved global analysis of nuclear parton distribution functions including RHIC data," *JHEP* **07** (2008) 102, arXiv:0802.0139 [hep-ph].

[52] A. Accardi, "Cronin effect in proton nucleus collisions: A survey of theoretical models," arXiv:hep-ph/0212148.

[53] P. Shukla, "Glauber model for heavy ion collisions from low energies to high energies," arXiv:nucl-th/0112039.

[54] M. Gyulassy and X.-n. Wang, "Multiple collisions and induced gluon Bremsstrahlung in QCD," *Nucl. Phys.* **B420** (1994) 583–614, arXiv:nucl-th/9306003.

[55] R. Baier, Y. L. Dokshitzer, S. Peigne, and D. Schiff, "Induced gluon radiation in a QCD medium," *Phys. Lett.* **B345** (1995) 277–286, arXiv:hep-ph/9411409.

[56] R. Baier, Y. L. Dokshitzer, A. H. Mueller, S. Peigne, and D. Schiff, "Radiative energy loss of high energy quarks and gluons in a finite-volume quark-gluon plasma," *Nucl. Phys.* **B483** (1997) 291–320, arXiv:hep-ph/9607355.

[57] N. Armesto, C. A. Salgado, and U. A. Wiedemann, "Medium-induced gluon radiation off massive quarks fills the dead cone," *Phys. Rev.* **D69** (2004) 114003, arXiv:hep-ph/0312106.

[58] M. Gyulassy, P. Levai, and I. Vitev, "Non-Abelian energy loss at finite opacity," *Phys. Rev. Lett.* **85** (2000) 5535–5538, arXiv:nucl-th/0005032.

[59] P. B. Arnold, G. D. Moore, and L. G. Yaffe, "Photon emission from ultrarelativistic plasmas," *JHEP* **11** (2001) 057, arXiv:hep-ph/0109064.

[60] M. Luo, J.-w. Qiu, and G. F. Sterman, "Anomalous nuclear enhancement in deeply inelastic scattering and photoproduction," *Phys. Rev.* **D50** (1994) 1951–1971.

[61] A. Majumder, E. Wang, and X.-N. Wang, "Modified dihadron fragmentation functions in hot and nuclear matter," *Phys.Rev.Lett.* **99** (2007) 152301, arXiv:nucl-th/0412061 [nucl-th].

[62] K. Zapp, G. Ingelman, J. Rathsman, J. Stachel, and U. A. Wiedemann, "A Monte Carlo Model for 'Jet Quenching'," *Eur. Phys. J.* **C60** (2009) 617–632, arXiv:0804.3568 [hep-ph].

[63] N. Armesto, L. Cunqueiro, and C. Salgado, "Implementation of a medium-modified parton shower algorithm," *Eur.Phys.J.* **C61** (2009) 775–778, arXiv:0809.4433 [hep-ph].

[64] T. Renk, "Parton shower evolution in a 3-d hydrodynamical medium," *Phys.Rev.* **C78** (2008) 034908, arXiv:0806.0305 [hep-ph].

[65] D. d'Enterria, "Jet quenching," arXiv:0902.2011 [nucl-ex].

[66] K. Adcox *et al.*, (PHENIX Collaboration), "Suppression of hadrons with large transverse momentum in central Au+Au collisions at s(NN)**(1/2) = 130-GeV," *Phys. Rev. Lett.* **88** (2002) 022301, arXiv:nucl-ex/0109003.

[67] D. Kharzeev, E. Levin, and L. McLerran, "Parton saturation and N(part) scaling of semi-hard processes in QCD," *Phys. Lett.* **B561** (2003) 93–101, arXiv:hep-ph/0210332.

[68] I. Vitev, "Initial state parton broadening and energy loss probed in d + Au at RHIC," *Phys. Lett.* **B562** (2003) 36–44, arXiv:nucl-th/0302002.

[69] S. Adler *et al.*, (PHENIX Collaboration), "Centrality dependence of pi0 and eta production at large transverse momentum in s(NN)**(1/2) = 200-GeV d+Au collisions," *Phys.Rev.Lett.* **98** (2007) 172302, arXiv:nucl-ex/0610036 [nucl-ex].

[70] B. A. Cole, G. G. Barnafoldi, P. Levai, G. Papp, and G. Fai, "EMC effect and jet energy loss in relativistic deuteron nucleus collisions," arXiv:hep-ph/0702101.

[71] M. Cacciari and G. P. Salam, "Pileup subtraction using jet areas," *Phys. Lett.* **B659** (2008) 119–126, arXiv:0707.1378 [hep-ph].

[72] S. Salur, (STAR Collaboration), "First Direct Measurement of Jets in $\sqrt{s_{NN}} = 200$ GeV Heavy Ion Collisions by STAR," *Eur. Phys. J.* **C61** (2009) 761–767, arXiv:0809.1609 [nucl-ex].

[73] J. Putschke, (STAR Collaboration), "First fragmentation function measurements from full jet reconstruction in heavy-ion collisions at $\sqrt{s_{\rm NN}} = 200$ GeV by STAR," *Eur. Phys. J.* **C61** (2009) 629–635, arXiv:0809.1419 [nucl-ex].

[74] M. Ploskon, (STAR Collaboration), "Inclusive cross section and correlations of fully reconstructed jets in 200 GeV Au+Au and p+p collisions," *Nucl. Phys.* **A830** (2009) 255c–258c, arXiv:0908.1799 [nucl-ex].

[75] E. Bruna, (STAR Collaboration), "Measurements of jet structure and fragmentation from full jet reconstruction in heavy ion collisions at RHIC," *Nucl. Phys.* **A830** (2009) 267c–270c, arXiv:0907.4788 [nucl-ex].

[76] J. Putschke, (STAR Collaboration), "Towards a consistent jet quenching picture at rhic (and lhc?)," Presented in the RHIC & AGS Users Meeting, 2009. http://www.bnl.gov/aum/content/workshops/pdf/Folder1/ags_putschke_web.pdf.

[77] A. Ohlson, (STAR Collaboration), "Jet-hadron correlations in STAR," *J.Phys.G* **G38** (2011) 124159, arXiv:1106.6243 [nucl-ex].

[78] J. Kapitan, (STAR Collaboration), "Jet studies with STAR at RHIC: jet algorithms, jet shapes, jets in AA," arXiv:1111.1892 [nucl-ex].

[79] H. Caines, (STAR Collaboration), "Jets and jet-like correlations studies from STAR," *J.Phys.G* **G38** (2011) 124019, arXiv:1106.6247 [nucl-ex].

[80] S. S. Adler *et al.*, (PHENIX Collaboration), "Common suppression pattern of eta and pi0 mesons at high transverse momentum in Au + Au collisions at s(NN)**(1/2) = 200-GeV," *Phys. Rev. Lett.* **96** (2006) 202301, arXiv:nucl-ex/0601037.

[81] T. Renk and K. Eskola, "Prospects of medium tomography using back-to-back hadron correlations," *Phys.Rev.* **C75** (2007) 054910, arXiv:hep-ph/0610059 [hep-ph].

[82] H. Hahn *et al.*, "The RHIC design overview," *Nucl. Instrum. Meth.* **A499** (2003) 245–263.

[83] K. H. Ackermann *et al.*, (STAR Collaboration), "Star detector overview," *Nucl. Instrum. Meth.* **A499** (2003) 624–632.

[84] I. Alekseev, C. Allgower, M. Bai, Y. Batygin, L. Bozano, *et al.*, "Polarized proton collider at RHIC," *Nucl.Instrum.Meth.* **A499** (2003) 392–414.

[85] J. Alessi *et al.*, "Upgrade and Operation of the BNL Tandems for RHIC Injection,". Presented at IEEE Particle Accelerator Conference (PAC2001), Chicago, Illinois, 18-22 Jun 2001.

[86] H. W. P. Thieberger, M. McKeown *IEEE Trans. Nucl. Sci. NS-30 (4) (1983) 2746.* .

[87] J. Brennan and M. Blaskiewicz, "Stochastic cooling in rhic," *Proceedings of PAC09, Vancouver, BC, Canada* 1910–1914. http://epaper.kek.jp/PAC2009/papers/we3gri01.pdf.

[88] W. Fischer, "Rhic run overview,". http://www.agshome.bnl.gov/RHIC/Runs/.

[89] K. H. Ackermann *et al.*, "The forward time projection chamber (FTPC) in STAR," *Nucl. Instrum. Meth.* **A499** (2003) 713–719, arXiv:nucl-ex/0211014.

[90] K. H. Ackermann *et al.*, (STAR Collaboration), "The STAR time projection chamber," *Nucl. Phys.* **A661** (1999) 681–685.

[91] M. Anderson *et al.*, "The STAR time projection chamber: A unique tool for studying high multiplicity events at RHIC," *Nucl. Instrum. Meth.* **A499** (2003) 659–678, arXiv:nucl-ex/0301015.

[92] M. Anderson *et al.*, "A readout system for the STAR time projection chamber," *Nucl. Instrum. Meth.* **A499** (2003) 679–691, arXiv:nucl-ex/0205014.

[93] G. Van Buren, L. Didenko, J. Dunlop, Y. Fisyak, J. Lauret, *et al.*, "Correcting for distortions due to ionization in the STAR TPC," *Nucl.Instrum.Meth.* **A566** (2006) 22–25, arXiv:physics/0512157 [physics].

[94] W. Llope, (STAR Collaboration), "The large-area time-of-flight (TOF) upgrade for the STAR detector," *AIP Conf.Proc.* **1099** (2009) 778–781. http://wjllope.rice.edu/~WJLlope/-myPublications/LLOPE_caari2008_proceedings.pdf.

[95] H. Agakishiev *et al.*, (STAR Collaboration), "Observation of the antimatter helium-4 nucleus," *Nature* **473** (2011) 353–356, arXiv:1103.3312 [nucl-ex].

[96] M. Beddo *et al.*, (STAR Collaboration), "The STAR barrel electromagnetic calorimeter," *Nucl.Instrum.Meth.* **A499** (2003) 725–739.

[97] C. Adler *et al.*, "The RHIC zero-degree calorimeters," *Nucl. Instrum. Meth.* **A461** (2001) 337–340.

[98] J. Kiryluk, (STAR Collaboration), "Relative luminosity measurement in STAR and implications for spin asymmetry determinations," *AIP Conf.Proc.* **675** (2003) 424–428.

[99] J. Kiryluk, (STAR Collaboration), "Local polarimetry for proton beams with the STAR beam beam counters," *16th International Spin Physics Symposium Proc.* (2005) 718–721, arXiv:hep-ex/0501072 [hep-ex].

[100] R. Averbeck, (PHENIX Collaboration), "Limits on the viscosity to entropy ratio from phenix data on single electron production," Presented in the 20th International Conference on Ultra-Relativistic Nucleus Nucleus Collisions, 2008. `http://www.phenix.bnl.gov/phenix/WWW/publish/ralf/talks/qm_2008/RalfAverbeck_qm2008.pdf`.

[101] C. Adler *et al.*, (STAR Collaboration), "Centrality dependence of high p(T) hadron suppression in Au+Au collisions at s**(NN)(1/2) = 130-GeV," *Phys. Rev. Lett.* **89** (2002) 202301, `arXiv:nucl-ex/0206011`.

[102] R. Baier, D. Schiff, and B. Zakharov, "Energy loss in perturbative QCD," *Ann.Rev.Nucl.Part.Sci.* **50** (2000) 37–69, `arXiv:hep-ph/0002198 [hep-ph]`.

[103] M. Gyulassy, I. Vitev, X.-N. Wang, and B.-W. Zhang, "Jet quenching and radiative energy loss in dense nuclear matter," `arXiv:nucl-th/0302077 [nucl-th]`. Published in Quark Gluon Plasma 3, editors: R.C. Hwa and X.N. Wang, World Scientific, Singapore.

[104] Y. L. Dokshitzer and D. E. Kharzeev, "Heavy quark colorimetry of QCD matter," *Phys. Lett.* **B519** (2001) 199–206, `arXiv:hep-ph/0106202`.

[105] B. I. Abelev *et al.*, (STAR Collaboration), "Erratum: Transverse momentum and centrality dependence of high-$p_{\rm T}$ non-photonic electron suppression in Au+Au collisions at $\sqrt{s_{\rm NN}} = 200$ GeV," *Phys. Rev. Lett.* **98** (2007) 192301, `arXiv:nucl-ex/0607012`. [Erratum-ibid.106:159902,2011].

[106] A. Adare *et al.*, (PHENIX Collaboration), "Energy Loss and Flow of Heavy Quarks in Au+Au Collisions at $\sqrt{s_{\rm NN}} = 200$ GeV," *Phys. Rev. Lett.* **98** (2007) 172301, `arXiv:nucl-ex/0611018`.

[107] B. Abelev *et al.*, (STAR Collaboration), "Erratum: Transverse momentum and centrality dependence of high-$p_{\rm T}$ non-photonic electron suppression in Au+Au collisions at $\sqrt{s_{\rm NN}} = 200$ GeV," *Phys.Rev.Lett.* **98** (2007) 192301, `arXiv:nucl-ex/0607012 [nucl-ex]`.

[108] P. R. Sorensen and X. Dong, "Suppression of non-photonic electrons from enhancement of charm baryons in heavy ion collisions," *Phys. Rev.* **C74** (2006) 024902, `arXiv:nucl-th/0512042`.

[109] B. Abelev *et al.*, (STAR Collaboration), "Identified baryon and meson distributions at large transverse momenta from Au+Au collisions at

s(NN)**(1/2) = 200-GeV," *Phys.Rev.Lett.* **97** (2006) 152301, arXiv:nucl-ex/0606003 [nucl-ex].

[110] B. Abelev *et al.*, (STAR Collaboration), "Energy dependence of pi+-, p and anti-p transverse momentum spectra for Au+Au collisions at s(NN)**(1/2) = 62.4 and 200-GeV," *Phys.Lett.* **B655** (2007) 104–113, arXiv:nucl-ex/0703040 [nucl-ex].

[111] J. Adams *et al.*, (STAR Collaboration), "Measurements of identified particles at intermediate transverse momentum in the STAR experiment from Au + Au collisions at s(NN)**(1/2) = 200-GeV," arXiv:nucl-ex/0601042.

[112] M. A. Lamont, (STAR Collaboration), "Recent Results on Strangeness Production at RHIC," *J.Phys.Conf.Ser.* **50** (2006) 192–200, arXiv:nucl-ex/0608017 [nucl-ex].

[113] A. Andronic, P. Braun-Munzinger, K. Redlich, and J. Stachel, "Statistical hadronization of charm in heavy-ion collisions at SPS, RHIC and LHC," *Phys. Lett.* **B571** (2003) 36–44, arXiv:nucl-th/0303036.

[114] S. H. Lee, K. Ohnishi, S. Yasui, I.-K. Yoo, and C.-M. Ko, "Λ_C enhancement from strongly coupled quark-gluon plasma," *Phys. Rev. Lett.* **100** (2008) 222301, arXiv:0709.3637 [nucl-th].

[115] L. Arnold *et al.*, "The STAR silicon strip detector (SSD)," *Nucl. Instrum. Meth.* **A499** (2003) 652–658, arXiv:physics/0211083.

[116] M. Gyulassy and X.-N. Wang, "HIJING 1.0: A Monte Carlo program for parton and particle production in high-energy hadronic and nuclear collisions," *Comput. Phys. Commun.* **83** (1994) 307, arXiv:nucl-th/9502021.

[117] E. Anderssen *et al.*, "A Heavy Flavor Tracker for STAR,". http://rnc.lbl.gov/hft/docs/hft_final_submission_version.pdf.

[118] M. Shao *et al.*, "Extensive particle identification with TPC and TOF at the STAR experiment," *Nucl. Instrum. Meth.* **A558** (2006) 419–429, arXiv:nucl-ex/0505026.

[119] B. Abelev *et al.*, (STAR Collaboration), "Charmed hadron production at low transverse momentum in Au+Au collisions at RHIC," arXiv:0805.0364 [nucl-ex].

[120] "STAR RunLog Browser for Run 10,". `http://online.star.bnl.gov/RunLogRun10/`.

[121] J. Kapitan, (STAR Collaboration), "Open charm measurement with HFT at STAR," *Indian J.Phys.* **85** (2011) 177–181, `arXiv:0806.2266 [nucl-ex]`.

[122] R. E. Kalman, "A new approach to linear filtering and prediction problems," *Transactions of the ASME–Journal of Basic Engineering* **82** no. Series D, (1960) 35–45.

[123] S. A. Voloshin, "Anisotropic flow at RHIC: Constituent quark scaling," *J. Phys. Conf. Ser.* **9** (2005) 276–279.

[124] J. Kapitan, (STAR Collaboration), "STAR inner tracking upgrade: A performance study," *Eur.Phys.J.* **C62** (2009) 217–221, `arXiv:0811.2311 [nucl-ex]`.

[125] "Actions Authorized by Critical Decision (CD) Approval,". `http://www.fnal.gov/directorate/OPMO/DOE/o413/CD_Actions_Authorized.pdf`.

[126] J. Kapitan, (STAR Collaboration), "Performance study of the Heavy Flavor Tracker for STAR," *Proceedings of the 16th Conference of Czech and Slovak Physicists* (2009) 43–48.

[127] "The STAR Heavy Flavor Tracker Conceptual Design Report,". `http://www4.rcf.bnl.gov/~videbaks/hft/cd1/HFT_CDR_V26.pdf`.

[128] R. Reed *et al.*, "Vertex finding in pile-up rich events for p+p and d+Au collisions at STAR," *J. Phys. Conf. Ser.* **219** (2010) 032020.

[129] L. Hulthén and M. Sagawara *Handbuch der Physik* **39** (1957) .

[130] M. L. Miller, K. Reygers, S. J. Sanders, and P. Steinberg, "Glauber modeling in high energy nuclear collisions," *Ann.Rev.Nucl.Part.Sci.* **57** (2007) 205–243, `arXiv:nucl-ex/0701025 [nucl-ex]`.

[131] R. E. Ansorge *et al.*, (UA5 Collaboration), "Charged Particle Multiplicity Distributions at 200-GeV and 900-GeV Center-Of-Mass Energy," *Z. Phys.* **C43** (1989) 357.

[132] C. Jena private communication.

[133] J. Adams *et al.*, (STAR Collaboration), "Identified hadron spectra at large transverse momentum in p+p and d+Au collisions at s(NN)**(1/2) = 200-GeV," *Phys.Lett.* **B637** (2006) 161–169, arXiv:nucl-ex/0601033 [nucl-ex].

[134] M. Walker, "Run 8 BTOW Calibration: MIP peak analysis (TPC tracks, 2008 pp data),". http://drupal.star.bnl.gov/STAR/subsys/bemc/calibrations/run-8-btow-calibration-2008/03-mip-peak-analysis.

[135] M. Walker, "Run 8 BTOW Calibration: Absolute Calibration from Electrons,". http://drupal.star.bnl.gov/STAR/subsys/bemc/calibrations/run-8-btow-calibration-2008/05-absolute-calibration-electrons.

[136] P. Djawotho, "Gluon polarization measurements with inclusive jets at STAR," arXiv:1106.5769 [nucl-ex].

[137] H. Caines, (STAR Collaboration), "Exploring Jet Properties in p-p Collisions at 200-GeV with STAR," *Nucl.Phys.* **A830** (2009) 263C–266C, arXiv:0907.3460 [nucl-ex].

[138] J. Bielčíková, (STAR Collaboration), "Underlying event studies in d+Au collisions at $\sqrt{s_{\rm NN}} = 200$ GeV from STAR," Poster presented in the Quark Matter conference, 2011. http://drupal.star.bnl.gov/STAR/system/files/QM2011_bielcikova_final.pdf.

[139] R. Field, "PYTHIA Tune Set A,". http://www.phys.ufl.edu/~rfield/cdf/tunes/py_tuneA.html.

[140] J. Kapitan, (STAR Collaboration), "Jets in 200 GeV p+p and d+Au collisions from the STAR experiment at RHIC," *J.Phys.Conf.Ser.* **270** (2011) 012015, arXiv:1008.4875 [nucl-ex].

[141] T. Sakuma private communication.

[142] P. M. Jacobs, (STAR Collaboration), "Background Fluctuations in Heavy Ion Jet Reconstruction," *Nucl.Phys.* **A855** (2011) 299–302, arXiv:1012.2406 [nucl-ex].

[143] M. J. Tannenbaum, "The distribution function of the event-by-event average p(T) for statistically independent emission," *Phys. Lett.* **B498** (2001) 29–34.

[144] N. Grau, (PHENIX Collaboration), "Probing Nuclear Matter With Jets and γ-Hadron Correlations: Results from PHENIX," *J.Phys.G* **G38** (2011) 124090, arXiv:1108.0085 [nucl-ex].

[145] D. Perepelitsa, (PHENIX Collaboration), "Jets in phenix," Presented in the workshop High-pT Probes of High-Density QCD at the LHC, 2011. http://indico.in2p3.fr/getFile.py/access?contribId=6&resId=0&materialId=slides&confId=4422.

[146] J. Kapitan, (STAR Collaboration), "Full jet reconstruction in 200 GeV p+p, d+Au and Au+Au collisions by STAR," *PoS* **EPS-HEP2009** (2009) 041, arXiv:0909.2951 [nucl-ex].

[147] S. Adler *et al.*, (PHENIX Collaboration), "Jet properties from dihadron correlations in p^+p collisions at $\sqrt{s} = 200$-GeV," *Phys.Rev.* **D74** (2006) 072002, arXiv:hep-ex/0605039 [hep-ex].

[148] M. M. Mondal, (STAR Collaboration), "K(T) measurement of partons from di-hadron correlation and a comparative study with jet reconstruction method using PYTHIA," *Int. J. Mod. Phys.* **E20** (2011) 1656–1661.

[149] M. M. Mondal, (STAR Collaboration), "Jet properties in p+p and their possible modification in cold nuclear matter in star," Poster presented in the Quark Matter conference, 2011. http://indico.cern.ch/contributionDisplay.py?contribId=231&sessionId=65&confId=30248.

[150] M. M. Mondal private communication.

[151] J. Kapitan, (STAR Collaboration), "Jet measurements in p+p and d+Au collisions with STAR at RHIC," *Int.J.Mod.Phys.* **E20** (2011) 1651–1655, arXiv:1012.0362 [nucl-ex].

[152] J. Kapitan, (STAR Collaboration), "Jet studies in 200 GeV p+p and d+Au collisions from the STAR experiment at RHIC," *Nucl.Phys.* **A855** (2011) 412–415, arXiv:1012.1804 [nucl-ex].

[153] J. Kapitan, (STAR Collaboration), "Initial state nuclear effects for jet production measured in s(NN)**(1/2) = 200-GeV d + Au collisions by STAR," *Nucl.Phys.* **A830** (2009) 619C–620C, arXiv:0907.3830 [nucl-ex].

[154] *Lectures on Theoretical Physics*. Interscience, NY, 1959.

[155] A. Bialas, M. Bleszynski, and W. Czyz, "Multiplicity Distributions in Nucleus-Nucleus Collisions at High-Energies," *Nucl. Phys.* **B111** (1976) 461.

[156] D. Kharzeev and M. Nardi, "Hadron production in nuclear collisions at RHIC and high density QCD," *Phys. Lett.* **B507** (2001) 121–128, arXiv:nucl-th/0012025.